

**THE MICROSTRUCTURE AND PROPERTIES OF
AUTOGENOUS GAS TUNGSTEN ARC AND LASER WELDS IN
TYPE 441 FERRITIC STAINLESS STEEL**

by

Mpho Collins Mmadi

Submitted in partial fulfillment of the requirements for the degree

Master of Engineering

in the Faculty of Engineering, the Built Environment and Information Technology,
University of Pretoria

October 2015

ABSTRACT

Type 441 stainless steel (EN 1.4509 or UNS S43940) is a low carbon dual-stabilised ferritic grade with a nominal chromium content of 18%. This steel displays high corrosion and oxidation resistance, good formability, excellent high temperature strength and thermal fatigue resistance. Type 441 stainless steel is used primarily in high temperature applications such as the automotive exhaust systems. The ferritic grades of stainless steel are difficult to weld successfully, especially in thicker sections, and for applications involving welding, the recommended plate thickness is limited to 2.5 mm for type 441. This investigation studied the weldability of type 441 stainless steel in thicker sections, with specific emphasis on the microstructure and mechanical properties of the weld metal and heat-affected zone after gas tungsten arc welding and laser beam welding at various heat input levels. The precipitation of intermetallic compounds (such as Laves and sigma phase) during the weld thermal cycle, carbide precipitation and grain growth in the weld metal and high temperature heat-affected zone were considered.

The results indicate that the microstructures of the weld and heat-affected zone that form during autogenous welding of type 441 stainless steel are complex and strongly dependent on the cooling rate after welding (and therefore the weld heat input used). Laves phase, sigma phase, $M_{23}C_6$ carbides and needle-like titanium-rich carbides (with niobium in solid solution) were observed in the welds and heat-affected zones of gas tungsten arc welds. The presence of intermetallic compounds and carbides embrittled the weld metal and increased the hardness of the weld metal significantly. The fusion zones of the laser welds were observed to be mostly free of second phase particles, whereas the heat-affected zone contained partially dissolved cuboidal titanium-rich carbides and some $M_{23}C_6$ carbides (in the higher heat input welds). The laser welds displayed significantly higher strength and ductility, which can be attributed to the lower heat inputs utilised and the finer grain sizes obtained.

Although type 441 is dual-stabilized with titanium and niobium, welding at low heat input levels resulted in chromium-rich $M_{23}C_6$ precipitation in the high temperature heat-affected zone during cooling, effectively sensitising the welds to intergranular corrosion. Sensitisation in gas tungsten arc welds was limited to a narrow region of the HTHAZ

adjacent to the fusion line in low heat input welds, but extended well into the HTHAZ and weld metal at heat inputs of 0.3 kJ/mm and 0.45 kJ/mm. Sensitisation was mostly suppressed in samples welded at a heat input of 0.7 kJ/mm. Sensitisation was observed in the weld metal of laser welds performed at 0.11 kJ/mm, and in the weld and HTHAZ after welding at 0.23 kJ/mm.

TABLE OF CONTENTS

<u>CHAPTER 1: OVERVIEW OF THE PROJECT</u>	p. 1
1.1 INTRODUCTION	p. 1
1.2 PROBLEM STATEMENT	p. 4
1.3 OBJECTIVES	p. 5
1.4 REFERENCES	p. 5
<u>CHAPTER 2: THE PHYSICAL METALLURGY AND WELDING OF FERRITIC STAINLESS STEELS</u>	p. 8
2.1 PHYSICAL METALLURGY OF STAINLESS STEELS	p. 8
2.2 TYPES OF STAINLESS STEELS	p. 11
2.3 TYPE 441 FERRITIC STAINLESS STEEL	p. 15
2.4 EMBRITTLEMENT DURING THE WELDING OF FERRITIC STAINLESS STEELS	p. 19
2.5 REFERENCES	p. 42
<u>CHAPTER 3: PROCESSES FOR WELDING STAINLESS STEEL</u>	p. 45
3.1 GAS TUNGSTEN ARC WELDING	p. 45
3.2 LASER BEAM WELDING	p. 47
3.3 MOTIVATION FOR CHOOSING GTAW AND LBW	p. 50
3.4 REFERENCES	p. 51
<u>CHAPTER 4: EXPERIMENTAL PROCEDURE</u>	p. 52
4.1 ALLOY INVESTIGATED	p. 52
4.2 THERMODYNAMIC MODELLING	p. 52
4.3 WELDING	p. 53
4.4 METALLOGRAPHIC INVESTIGATION	p. 55
4.5 PHASE IDENTIFICATION	p. 56
4.6 SENSITISATION TESTING	p. 57
4.7 DILATOMETRY	p. 58
4.8 MECHANICAL TESTING	p. 58
4.9 REFERENCES	p. 60
<u>CHAPTER 5: RESULTS AND DISCUSSION</u>	p. 62
5.1 MICROSTRUCTURE PREDICTIONS FOR TYPE 441 STAINLESS STEEL	p. 62
5.2 MICROSTRUCTURES OF THE GAS TUNGSTEN ARC WELDS	p. 64
5.3 MICROSTRUCTURES OF THE LASER BEAM WELDS	p. 76

5.4 GRAIN REFINEMENT EFFECT IN THE LTHAZ OF THE GAS TUNGSTEN ARC WELDS	p. 81
5.5 MECHANICAL PROPERTIES	p. 86
5.6 IMPACT TOUGHNESS	p. 88
5.7 FRACTURE SURFACES	p. 89
5.8 REFERENCES	p. 94
<u>CHAPTER 6: CONCLUSIONS AND RECOMMENDATIONS</u>	p. 95
6.1 CONCLUSIONS	p. 95
6.2 RECOMMENDATIONS FOR FUTURE WORK	p. 96
<u>APPENDIX</u>	p. 98

CHAPTER 1: OVERVIEW OF THE PROJECT

1.1 INTRODUCTION

Columbus Stainless (Pty) Ltd is a primary producer of stainless steel flat products in South Africa. Its integrated production plant, located in Mpumalanga, produces a wide range of products in various austenitic, ferritic, martensitic, utility and duplex stainless steel grades for the local and export markets [1].

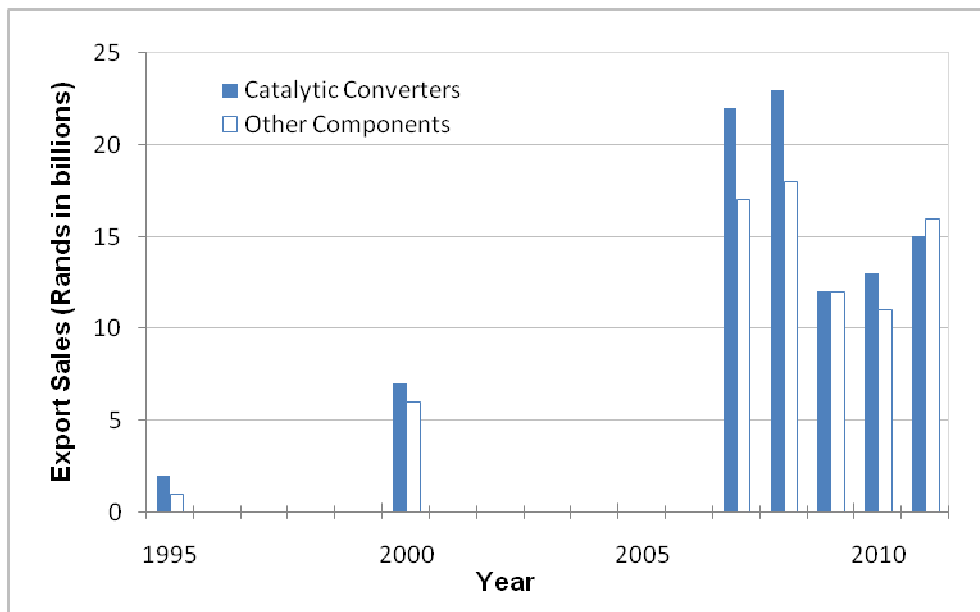


Figure 1.1: Automotive components turnover in South Africa [2].

A significant proportion of its ferritic stainless steel production is utilised in the automotive industry, in particular in the production of catalytic converters for exhaust systems. Due to the abundant local supply of ferrochrome and platinum group metals (PGM's) and the favourable incentives launched by the South African government in the 1990's in the form of the Motor Industry Development Programme (MIDP), the local catalytic converter industry has experienced remarkable success in the last two decades, averaging compound growth of around 14% per annum in the years leading up to 2012. As shown in Figure 1.1 above, the contribution of the catalytic converter industry to the value of automotive component export sales remained high despite a decrease in the value of export sales in 2008 and 2009 due to the impact of the global recession. Unfortunately, the catalytic converter industry in South Africa is currently under threat, mainly due to uncertainties introduced by

the recent transition from the export-focused MIDP to the value-added Automotive Production Development Programme (APDP) [2].

The catalytic converter components in exhaust systems are operated at temperatures up to 900°C, but temperature variations are frequently experienced due to intermittent operation. A material with high strength at elevated temperature, good thermal fatigue resistance, a low coefficient of thermal expansion and moderate corrosion resistance in the exhaust gas environment is therefore preferred. Ferritic stainless steels (FSS) are replacing carbon steels and austenitic stainless steels for this application due to the following reasons;

- FSS are cheaper compared to the austenitic stainless.
- FSS have a better strength to weight ratio than carbon steels.
- FSS have better corrosion resistance than carbon steels and thus a longer life.
- FSS have a greater resistance to stress corrosion cracking compared to austenitic stainless steels.
- FSS also have a low coefficient of thermal expansion [2, 3].

Ferritic stainless steels, however, have a lower high temperature strength compared to austenitic steels. An incentive therefore exists to produce ferritic stainless steels with improved high temperature properties [3].

Type 441 ferritic stainless steel is increasingly finding application in the higher temperature parts of the automobile exhaust system and catalytic converter. This steel is equivalent to grades EN 1.4509 (as specified in BS EN 10088-2:2005 [4]) and UNS S44100 (in accordance with ASTM A240/A240M-14 [5]). As shown in Table 1.1, type 441 is a dual-stabilised ferritic stainless steel with a nominal chromium content of 18%. This steel displays excellent corrosion resistance, oxidation resistance, high temperature strength, thermal fatigue resistance and formability [3]. Titanium and niobium act as stabilising elements to prevent sensitisation and improve resistance to intergranular corrosion [6], whereas niobium (in solid solution) also increases the high temperature strength of the steel [7].

Table 1.1: Specified chemical composition of type 441 ferritic stainless steel in accordance with BS EN 10088-2:2005 and ASTM A240/A240M-14 (compositions are shown as ranges or maximum values, balance Fe) [4, 5]

Grade	C	Si	Mn	P	S	N	Cr	Nb	Ni	Ti
EN 1.4509	0.03	1.00	1.0	0.040	0.030	0.03	17.5-19.5	(9xC+0.3) min.	1.0	0.1-0.5
UNS S44100	0.03	0.75	1.0	0.040	0.015	Not specified	17.5-18.5	(3xC+0.3) to 1.0	Not specified	0.1-0.6

The ferritic grades of stainless steel are, however, difficult to weld successfully, especially in thicker sections. High temperature embrittlement is one of the most serious problems associated with welding ferritic stainless steels. This form of embrittlement is a function of both composition and microstructure. Excessive grain growth in the heat-affected zone (and in the weld metal of autogenous welds or welds produced with matching consumables) tends to reduce toughness and increase the ductile-to-brittle transition temperature of the welded joint. The presence of interstitial elements, such as carbon and nitrogen, further embrittles the steel and promotes sensitisation and intergranular corrosion through the formation of chromium-rich grain boundary carbides. Although ferritic stainless steels are generally resistant to most forms of stress corrosion cracking, intergranular stress corrosion cracking has been observed in ferritic grades in the presence of a sensitised microstructure. Stabilisation with titanium and/or niobium is beneficial in this regard. These elements have a high affinity for carbon and nitrogen, and form stable alloy carbonitrides on cooling, effectively preventing the formation of chromium carbides at lower temperatures [6, 8].

The precipitation of intermetallic compounds has also been shown to be detrimental to the toughness and corrosion resistance of highly alloyed ferritic stainless steel welds. Sigma (σ) phase is an intermetallic compound of iron and chromium that forms at temperatures below approximately 820°C in high chromium alloys and severely embrittles stainless steels. Although precipitation is sluggish in most stainless steels, higher chromium contents, as well as the presence of titanium and niobium, tend to accelerate sigma phase formation. As a consequence, sigma phase may form during the weld thermal cycle leading to the embrittlement of welds [9]. Alloying with niobium may also negatively affect toughness through the precipitation

of intermetallic Laves phase (Fe_2Nb) [3] and by promoting solidification cracking in ferritic stainless steels [10].

1.2 PROBLEM STATEMENT

As described above, ferritic stainless steels are difficult to weld successfully, especially in thicker sections. The behaviour of the dual-stabilised type 441 stainless steel during welding is currently not well understood and a series of recent weld failures of type 441 during fabrication highlighted the need for a more in-depth investigation into the microstructures that form during welding and the influence of various microstructural features on susceptibility to failure during joining. Previous studies [3, 11-15] highlighted three areas related to the welding of type 441 that require further investigation:

- Despite the rapid heating and cooling rates associated with welding, the precipitation of intermetallic phases (in particular Laves and sigma phase) during the weld thermal cycle may reduce the toughness and ductility of the weld metal and heat-affected zone. Embrittlement due to Laves phase (Fe_2Nb) formation has been reported in type 441 stainless steel [3]. Laves phase has been observed in AISI 444 arc welds [11], but intermetallic phase precipitation in type 441 welds requires more investigation.
- An anomalous grain growth phenomenon has been observed in type 441 on heating to temperatures in excess of 1000°C , resulting in abnormal growth of individual grains within the microstructure [12]. This phenomenon has not been fully explained to date, but is expected to influence the grain structure that develops when the heat-affected zone of type 441 welds is heated to temperatures within the grain growth temperature range.
- Titanium-stabilised grades of ferritic stainless steel have been shown to be susceptible to sensitisation and intergranular corrosion after welding at low heat input levels [13-15]. The rapid cooling rates experienced after low heat input welding prevent the precipitation of titanium- or niobium-containing carbides at high temperatures, and promote the formation of coarse intergranular M_{23}C_6

carbides on cooling to lower temperatures. This phenomenon has not been investigated for dual-stabilised grades of ferritic stainless steel.

1.3 OBJECTIVES

To address the problem statement described above, this project aimed at examining the microstructures that develop in the weld metal and heat-affected zone of autogenous fusion welds in type 441, and determining the influence of these microstructures on the mechanical and corrosion properties of the welds. The following experimental procedure was followed (to be considered in more detail in Chapter 4):

- Autogenous fusion welding of type 441 was performed using gas tungsten arc welding (GTAW) and laser beam welding (LBW). A variety of heat inputs was used in order to obtain a range of cooling rates.
- Microstructural examination of the welds was carried out using optical microscopy, scanning electron microscopy (SEM) and high resolution SEM to identify second phase particles and precipitates, and to measure the heat-affected zone's grain size as a function of heat input. Energy dispersive X-ray spectrometry (EDS) and X-ray diffraction (XRD) techniques were used for phase identification.
- Heat flow modelling was used to relate the grain sizes and observed microstructures to the weld thermal profile, and thermodynamic modelling was used to study phase equilibria.
- The welds were evaluated for sensitisation and intergranular corrosion.
- The mechanical properties of the welds were determined using hardness measurements, Charpy impact testing and transverse tensile testing.

The results of this investigation are considered in more detail in Chapter 5.

1.4 REFERENCES

- [1] Columbus Stainless (Pty) Ltd company website at www.columbus.co.za.

- [2] K. Dewar. *“The catalytic converter industry in South Africa”*. Proceedings of the 5th International Platinum Conference, held in Sun City, South Africa, on 18-20 September 2012. SAIMM. pp. 893-904.
- [3] M. P. Sello and W. E. Stumpf, “Laves phase embrittlement of the ferritic stainless steel type AISI 441,” *Materials Science and Engineering: A*, vol. 527, no. 20, pp. 5194–5202, Jul. 2010.
- [4] BS EN 10088-2:2005. *“Stainless steels. Technical delivery conditions for sheet/plate and strip of corrosion resisting steels for general purposes”*. The British Standards Institution, London. 2005
- [5] ASTM A240/A240M-14. *“Standard Specification for Chromium and Chromium-Nickel Stainless Steel Plate, Sheet, and Strip for Pressure Vessels and for General Applications”*. ASTM International, West Conshohocken, PA. 2014.
- [6] W. Gordon and A. van Bennekom. *“Review of stabilisation of ferritic stainless steels”*. *Materials Science and Technology*, vol. 12, no. 2. 1996. pp. 126-131.
- [7] N. Fujita, K. Ohmura, M. Kikuchi, T. Suzuki, S. Funaki and I. Hiroshige. *“Effect of Nb on high-temperature properties for ferritic stainless steel”*. *Scripta Materialia*, vol. 35, no. 6. 1996. pp. 705-710.
- [8] J.C. Lippold and D.J. Kotecki. *“Welding metallurgy and weldability of stainless steels”*. Wiley, Hoboken, USA. 2005. pp. 85-137.
- [9] F.C. Hull. *“Effects of composition on embrittlement of austenitic stainless steels”*. *Welding Journal*, vol. 52. 1973. pp. 104s-113s.
- [10] D.H. Kah and D.W. Dickinson. *“Weldability of ferritic stainless steels”*. *Welding Journal*, vol. 60. August 1981. pp. 135s-142s.
- [11] C.C. Silva, J.P. Farias, H.C. Miranda, R.F. Guimarães, J.W.A. Menezes and M.A.M. Neto. *“Microstructural characterization of the HAZ in AISI 444 ferritic stainless steel welds”*. *Materials Characterization*, vol. 59. 2008. pp. 528-533.
- [12] N. Olivier. *“Quantification of the grain growth anomaly found in AISI stainless steel 441 above 900 °C”*. Final-year project (unpublished research). Department of Materials Science and Metallurgical Engineering, University of Pretoria, South Africa. November 2011.
- [13] M. du Toit, G.T. van Rooyen and D. Smith. *“An overview of the heat-affected zone sensitisation and stress corrosion cracking behaviour of 12% chromium*

type 1.4003 ferritic stainless steel". *Welding in the World*, vol. 51, no. 9/10. September/October 2007. pp. 41-50.

- [14] M.L. Greeff and M. du Toit. "*Looking at the sensitisation of 11-12% chromium EN 1.4003 stainless steels during welding*". *Welding Journal*, vol. 85, no. 11. November 2006. pp. 243s-251s.
- [15] C.J. van Niekerk, M. du Toit and M.W. Erwee. "*Heat-affected zone sensitisation of type 409 ferritic stainless steel during continuous cooling after low heat input welding*". *Welding in the World*, vol. 56, no. 5-6. May/June 2012. pp. 54-64.

CHAPTER 2: PHYSICAL METALLURGY AND WELDING **OF FERRITIC STAINLESS STEELS**

This chapter provides a brief overview of the general physical metallurgy of stainless steels, with special emphasis on the family of ferritic stainless steels that type 441 belongs to. This will be followed by a discussion of the alloy in question, its applications and weldability, before a general overview of the difficulties associated with the welding of ferritic stainless steels is provided.

2.1 PHYSICAL METALLURGY OF STAINLESS STEELS

Stainless steels are iron-based alloys containing appreciable amounts of chromium and less than 1.5 wt% carbon. These alloys are popular as engineering materials because of their excellent corrosion resistance in many environments. Stainless steels derive their corrosion resistance from a very stable, thin, hydrated surface oxide film (essentially Cr_2O_3) that forms spontaneously in oxidising environments. This oxide film protects the iron-chromium alloy from corrosion by forming a diffusion barrier between the corrosive environment and the underlying metal [1].

The binary iron-chromium equilibrium phase diagram is shown in Figure 2.1. The addition of chromium to iron restricts the austenite (γ) phase field with increasing chromium content until austenite disappears completely at chromium levels of more than about 12.7%. This implies that binary Fe-Cr alloys containing more than approximately 12.7% chromium do not undergo any δ -ferrite $\rightarrow \gamma$ or $\gamma \rightarrow \alpha$ -ferrite phase transformation on cooling, ruling out any accompanying grain refinement and the possibility of quench hardening. Chromium strongly promotes ferrite formation to the point where only δ -ferrite solidifies from the melt over the entire alloying range. Austenite forms from the ferrite in lower chromium alloys when the alloy is within the γ phase field. Rapid cooling of the austenite below the martensite start (M_s) temperature results in martensite formation. In binary Fe-Cr alloys furnace cooling promotes the transformation of austenite to low temperature ferrite (α).

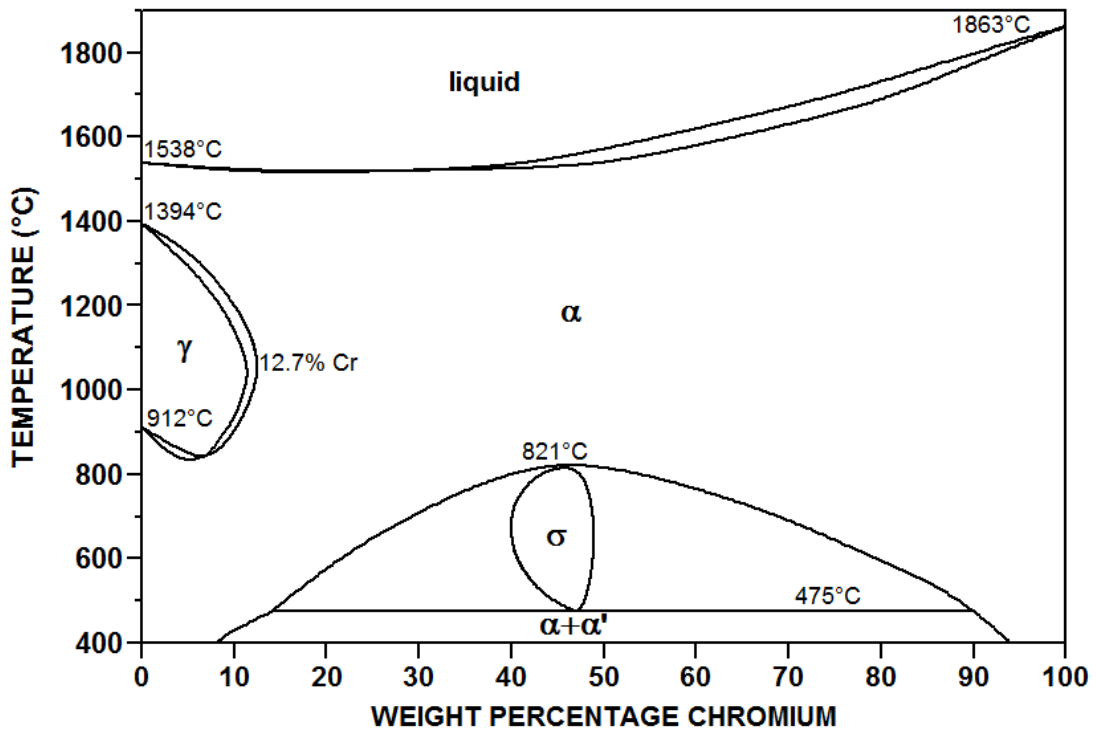


Figure 2.1: The equilibrium binary iron-chromium phase diagram [2].

At higher chromium contents, sigma (σ) phase precipitates from ferrite at temperatures below about 821°C. Sigma phase is a brittle intermetallic compound of iron and chromium (FeCr), consisting of approximately 45% chromium and 55% iron. Precipitation of sigma phase may be accompanied by chromium depletion of the matrix adjacent to the σ -phase boundaries [2].

The kinetics of sigma phase precipitation in stainless steel is usually sluggish, and the composition and temperature ranges over which sigma phase is stable are influenced by the presence of alloying additions. Hull [3] investigated the influence of various alloying additions on the precipitation of sigma phase at a temperature of 816°C and precipitation times up to 1000 hours in various carbon- and nitrogen-free Fe-Ni-Cr alloys. Based on his results, Hull calculated the chromium equivalent for embrittlement at 816°C, equation (2.1), which shows the influence of alloying elements on σ phase formation [3].

$$Cr_{eq} = \%Cr + 0.31(\%Mn) + 1.76(\%Mo) + 1.70(\%Nb) + 1.58(\%Si) + 2.44(\%Ti) + 1.22(\%Ta) + 2.02(\%V) + 0.97(\%W) - 0.266(\%Ni) - 0.177(\%Co) \quad \dots(2.1)$$

Elements with positive signs in equation (2.1) accelerate the precipitation of sigma phase. It is evident that only nickel and cobalt (which are strong austenite-forming elements) retard sigma phase precipitation in stainless steels.

Carbon and nitrogen were not included in Hull's investigation, but it has been reported that carbon retards sigma phase precipitation in stainless steels. Due to the low solubility of carbon in sigma phase, precipitation of sigma only starts once most of the carbon has been removed from solid solution to precipitate as $M_{23}C_6$ carbides. In addition, precipitation of $M_{23}C_6$ depletes the grain boundary areas of chromium. If the chromium content falls below the precipitation limit for sigma phase formation (approximately 16% chromium), the precipitation of sigma phase will be retarded even more [3,4]. According to Hull [3], alloying additions of titanium and niobium promote the precipitation of sigma phase by removing carbon from solid solution to form alloy carbides. As a result, stabilised steels behave in a similar manner to steels with a very low carbon content.

The influence of nitrogen is reported to be similar to that of carbon. Nitrogen must be removed from solid solution before sigma phase precipitation starts. Whereas carbon precipitates readily as $M_{23}C_6$, precipitation is considerably more difficult in the case of nitrogen. Precipitation is often only possible in the form of complex nitrides of the type M_2N that form very slowly [5].

Another feature of the Fe-Cr binary phase diagram shown in Figure 2.1 is the separation of ferrite into a magnetic component that is rich in iron (α), and a chromium-rich non-magnetic component with approximately 80% chromium (α') at temperatures between about 400°C to 510°C. This phenomenon, known as spinodal decomposition, is associated with severe embrittlement of the steel, and is often referred to as 475°C embrittlement. 475°C Embrittlement only occurs during the annealing of ferrite-containing stainless steels and stainless steel welds in the temperature range around 475°C. The formation of alpha prime (α') is sluggish in low chromium alloys, but is greatly accelerated with an increase in chromium and molybdenum contents [1,2].

2.2 TYPES OF STAINLESS STEELS

Stainless steels are classified on the predominant microstructural phase (or phases). There are five types of stainless steels, namely; martensitic, austenitic, duplex, precipitation-hardening, and ferritic stainless steels. These types of stainless steels will be briefly discussed here, and with special emphasis on ferritic stainless steels that type 441 belongs to.

2.2.1 Martensitic stainless steels

Martensitic stainless steels consist predominately of martensite at room temperature. Any austenite that is stable at high temperature transforms to martensite on rapid cooling, provided the martensite start temperature is above room temperature. The cooling rates during welding are usually rapid enough to transform austenite to martensite in the weld metal and heat-affected zone of most martensitic stainless steels[1]. The martensite crystal structure that forms is highly faulted, resulting in a very hard and brittle microstructure. As in carbon steels, the hardness of the martensite formed depends on its composition. The higher the carbon content of the martensite phase, the harder and more brittle it is. Yield strengths of martensitic stainless steels range from 275 MPa in the annealed condition to 1900 MPa in the quenched and tempered condition (for high carbon grades), but the corrosion resistance of these steels is generally inferior to that of other stainless steels due to the lower chromium requirement (typically 12 to 14 wt% chromium for the lower carbon grades). These steels therefore find application where high strength and moderate corrosion resistance under ambient atmospheric conditions are required [1].

2.2.2 Austenitic stainless steels

Austenitic stainless steels are predominantly austenitic at room temperature. These steels are not hardenable by heat treatment as the austenite is stable and does not transform to martensite on rapid cooling. Standard austenitic stainless steels contain 16 to 25 wt% chromium in addition to high concentrations of nickel. These steels have good ductility and toughness and exhibit significant elongation during tensile loading. Yield strengths are similar to those of mild steels. The austenitic grades have good low temperature properties and can be used in cryogenic applications. Depending on the chemical composition, these steels can also be used at

temperatures up to 760°C. Above this temperature the strength and corrosion resistance are compromised. The austenitic stainless steels are generally more expensive than the martensitic and ferritic grades because of their high nickel contents [1,2].

2.2.3 Duplex Stainless Steels

Duplex stainless steels contain approximately equal amounts of ferrite and austenite at room temperature. The duplex grades are usually highly alloyed with between 19 and 26 wt% chromium, additions of molybdenum and high concentrations of nitrogen. Molybdenum and nitrogen improve the localised corrosion resistance, while nitrogen helps to maintain the phase balance during welding. Most matching filler metals are overalloyed with nickel to improve the phase balance in the weld [1]. The duplex stainless steels are used in applications that require superior corrosion resistance and high strength and often replace austenitic stainless steels in applications where stress corrosion cracking resistance is required [1].

2.2.4 Precipitation hardened stainless steels

Precipitation hardened (PH) stainless steels are the least common of the stainless steels grades. They can be heat treated to contain strengthening precipitates. These steels are classified into three groups according to the predominant microstructure, namely martensitic, semi-austenitic and austenitic precipitation hardenable stainless steels. The PH grades are capable of achieving tensile strengths in excess of 1520 MPa in some alloys, with good ductility and toughness if heat treated correctly. Their maximum allowable service temperature can be as high as 615°C in the austenitic PH stainless steel grades [1].

2.2.5 Ferritic stainless steels

Ferritic stainless steels are essentially iron-chromium binary alloys containing about 12 to 30% chromium as major alloying element, in addition to a maximum of 0.25% carbon and various other possible alloying elements depending on the desired properties and application. These alloys are referred to as ferritic stainless steels because their microstructure remains mostly ferritic (body centred cubic ferrite) under normal heat treatment conditions. Chromium is a powerful ferrite-former and

extends the ferrite phase field while suppressing the region where austenite is stable on the phase diagram. Most ferritic stainless steels, since they contain more than 12% chromium, do not undergo the $\delta \rightarrow \gamma \rightarrow \alpha$ phase transformation and cool from high temperatures as a solid solution of chromium in ferrite [2].

Since the ferritic stainless steels are relatively low in cost (they do not contain significant amounts of nickel) and mostly resistant to chloride stress corrosion cracking, they may be preferred to austenitic stainless steels in certain applications. They are magnetic and are typically employed where corrosion resistance is needed but strength requirements are relatively moderate. Such applications include furnace parts, boiler baffles, kiln linings, stack dampers, chemical processing equipment, automobile trim, catalytic converters and decorative applications [2].

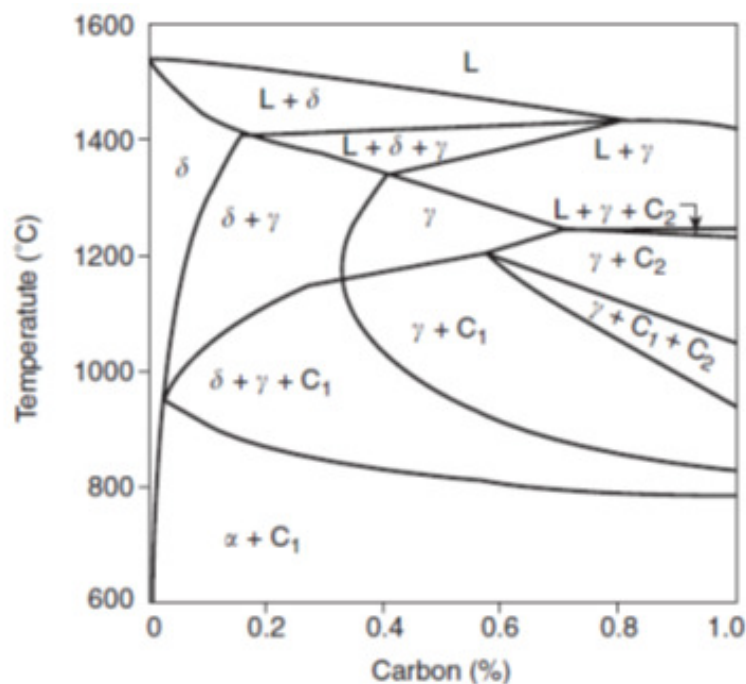


Figure 2.2: A vertical section of the Fe-Cr-C ternary phase diagram at 17 wt% chromium [2].

The influence of carbon on the microstructure of Fe-Cr alloys is illustrated in Figure 2.2, which displays a vertical section of the Fe-Cr-C ternary phase diagram at 17 wt% chromium. In this diagram C₁ refers to the M₂₃C₆ or (Fe,Cr)₂₃C₆ carbide and C₂ to the M₇C₃ or (Fe,Cr)₇C₃ carbide. The terms δ-ferrite and α-ferrite are sometimes used interchangeably as both refer to the same body centred cubic (BCC) crystal structure. In welding literature, ferrite that is formed by primary precipitation (from the melt) is usually referred to as δ-ferrite, whereas ferrite formed by secondary

precipitation from austenite during the $\gamma \rightarrow \alpha$ solid state phase transformation at lower temperatures is called α -ferrite. There is a slight difference in lattice parameter between BCC α -ferrite and BCC δ -ferrite in stainless steel [2].

It is evident from Figure 2.2 that the ferrite phase has a low solubility for carbon. The solubility of carbon in a 17% chromium alloy is approximately 0.05 wt% at 1000°C, but falls to negligible amounts at room temperature. Under equilibrium conditions any carbon dissolved in ferrite at elevated temperatures will therefore precipitate as a carbide phase on cooling. For carbon content lower than about 0.05 wt%, the microstructure of an Fe-17% Cr alloy remains ferritic down to room temperature. On cooling most of the carbon dissolved in the ferrite precipitates in the form of carbides, and the room temperature microstructure therefore consists of a mixture of ferrite and carbides. At higher carbon contents, a small amount of austenite may form on cooling. This austenite tends to transform to martensite if cooled to temperatures below the M_s temperature [2].

The nominal chemical composition of a number of commercially available medium chromium ferritic stainless steels is shown in Table 2.1. As indicated in this table, the composition of ferritic stainless steels has evolved over time as steelmaking practice improved. The first generation steels are unstabilised grades with medium chromium and relatively high carbon contents. Carbon is a strong austenite-former and expands the austenite phase field to higher chromium contents. Austenite tends to form in these alloys on cooling, and the room temperature microstructure typically consists of a mixture of ferrite and martensite. The second generation steels are stabilised with titanium and/or niobium to remove carbon and nitrogen from solid solution. This improves the weldability and promotes fully ferritic microstructures. Further improvements in steelmaking practice facilitated the development of the low interstitial third generation ferritic stainless steels. These grades are stabilised with titanium and/or niobium and display moderate corrosion resistance and mechanical properties [2].

Table 2.1: Nominal chemical compositions of a number of medium carbon ferritic stainless steels (weight percentage, balance Fe). Compositions are shown as ranges or maximum values [6,7].

Type	C	Mn	P	S	Si	Cr	Ni	Mo	N	Ti	Nb
<i>First generation: Unstabilised higher carbon grades</i>											
430	0.12	1.00	0.040	0.030	1.00	16.0-18.0	0.75	-	-	-	-
434	0.12	1.00	0.040	0.030	1.00	16.0-18.0	-	0.75-1.25	-	-	-
<i>Second generation: Stabilised grades</i>											
436	0.12	1.00	0.040	0.030	1.00	16.0-18.0	-	0.75-1.25	-	-	min. (5xC) max. 0.8
439	0.03	1.00	0.040	0.015	1.00	17.5-18.5	-	-	-	0.1-0.6	min. 0.3+(3xC)
441	0.03	1.00	0.040	0.015	0.75	17.5-18.5	1.0	-	0.03	0.1-0.6	min. 0.3+(3xC) max. 1.0
<i>Third generation: Stabilised low interstitial grades</i>											
444	0.025	1.00	0.040	0.030	1.00	17.5-19.5	1.0	1.75-2.50	0.035	min. (Ti+Nb)=0.2+4(C+N) max. 0.8	

2.3 TYPE 441 FERRITIC STAINLESS STEELS

2.3.1 Composition and mechanical properties

Type 441 is a medium chromium high-temperature ferritic stainless steel with a low interstitial content. The low nitrogen and carbon content improve toughness and deep-drawability, and prevent martensite formation at lower temperatures during cooling. The pitting corrosion resistance of type 441 is similar to that of AISI 304 austenitic stainless steel. Like most ferritic grades, type 441 is not susceptible to stress corrosion cracking. The low carbon content reduces susceptibility to sensitisation and intergranular corrosion and the alloy is dual-stabilised with niobium and titanium to improve weld ductility and resistance to intergranular corrosion in the weld heat-affected zone [8]. Table 2.2 shows the specified chemical composition range of type 441 stainless steel in accordance with ASTM A240/A240M-14 (included as UNS S44100) [6] and BS EN 10088-2:2005 (included as special grade EN 1.4509 or X2CrTiNb18) [7]. It should be noted that the designation 441, used in this dissertation to refer to the steel in question, is not officially included in ASTM A240/A240M-14, but is widely used as a colloquial synonym for EN 1.4509 or UNS grade S44100.

Table 2.2: Nominal composition of type 441 (EN 1.4509) ferritic stainless steel in accordance with ASTM A240/A240M-14 and BS EN 10088-2:2005 (compositions are shown as ranges or maximum values, balance Fe) [6,7].

Specification	C	Si	Mn	P	S	N	Cr	Nb	Ni	Ti
UNS S44100	0.03	0.75	1.0	0.040	0.015	Not specified	17.5-18.5	(3xC+0.3) to 1.0	Not specified	0.1-0.6
EN 1.4509	0.03	1.00	1.0	0.040	0.030	0.03	17.5-19.5	(9xC+0.3) min.	1.0	0.1-0.5

Type 441 solidifies as ferrite and remains ferritic down to room temperature. The steel is usually hot rolled and annealed at approximately 1035°C, followed by quenching and pickling [8,9]. Coarse cuboidal titanium carbonitrides remain randomly dispersed throughout the ferritic microstructure after annealing and quenching. Excess niobium in solid solution provides high temperature strength and promotes the precipitation of fine intermetallic Laves phase on slow cooling through the temperature range between 600°C and 950°C [9]. The room temperature mechanical properties of type 441 are shown in Table 2.3 (with those of AISI 304 austenitic stainless steel included as comparison). The high temperature properties are shown in Table 2.4.

2.3.2 Applications of type 441 ferritic stainless steel

Type 441 stainless steel is used in a wide range of applications, including elevator doors and frames, wall panels and cladding, in catering and appliances, as tubes and in heat exchangers, and to replace austenitic grades in corrosive applications [1,2]. Its excellent oxidation resistance at temperatures up to 950°C makes it an excellent candidate for use in the hot end of automotive exhaust systems [8].

Increasing pressure from environmental authorities to reduce dangerous exhaust gas emissions from cars has resulted in car manufacturers raising the temperature in the exhaust system in order to produce a cleaner exhaust gas. Table 2.5 shows the typical operating temperatures of different components in an automotive exhaust system. In the higher temperature components, excellent high temperature strength, thermal fatigue resistance and good oxidation resistance are required. Ferritic stainless are preferred in this application as they are less expensive than austenitic stainless steels, with good corrosion resistance in many exhaust gas environments

[1,2]. The addition of niobium to ferritic stainless steel improves the high temperature strength of the alloy [10].

Table 2.3: Mechanical properties of type 441 stainless steel compared to those of AISI 304 [7].

Steel	Yield Strength $R_{p0.2}$	Ultimate Tensile Strength R_m	Elongation	Hardness
EN 1.4509 (Type 441)	250 MPa	450-630 MPa	18%	180 BHN
EN 1.4301 (AISI 304)	230 MPa	540-750 MPa	45%	201 BHN

Table 2.4: Short term elevated temperature strength of type 441 stainless steel [7].

Property	Test temperature						
	100°C	200°C	300°C	400°C	500°C	600°C	700°C
Ultimate Tensile Strength R_m	460 MPa	425 MPa	400 MPa	380 MPa	350 MPa	295 MPa	200 MPa
Yield Strength $R_{p0.2}$	280 MPa	255 MPa	230 MPa	Not available	Not available	Not available	Not available

2.3.3 Welding of type 441 stainless steel

The ferritic grades of stainless steel are difficult to weld successfully, especially in thicker sections, and in applications involving welding, the maximum recommended plate thickness for type 441 is 2.5mm [8]. Type 441 has low carbon and nitrogen contents, and is dual-stabilised with titanium and niobium to reduce the risk of sensitisation and martensite formation on cooling. The high level of stabilisation improves the weldability of type 441 somewhat compared to other medium chromium stainless steels.

Fully ferritic stainless steels are prone to rapid grain growth on exposure to temperatures in excess of the grain growth temperature. These steels solidify as ferrite and remain ferritic down to room temperature. The absence of bulk solid state phase transformations during cooling leads to grain growth, further facilitated by rapid diffusion in the ferritic structure. Olivier [11] reported that type 441 ferritic stainless steel displays excessive grain coarsening when heated above 925°C. As with most ferritic stainless steels, the weldability of type 441 is mainly limited by grain

growth in the heat-affected zone (HAZ), so the heat input during welding must be kept to a minimum.

Table 2.5: Various components of automobile exhaust systems and their typical operating temperatures [12].

Component		Service temperature (°C)	Required properties	Current materials
Exhaust manifold		950-750	<ul style="list-style-type: none"> • High temperature strength • Thermal fatigue life • Oxidation resistance • Workability 	409, 441, 304, 321, 309
Front pipe		800-600		304, 321, 309, 409
Flexible pipe				304, 321, 309, 316Ti
Catalytic converter	Shell	800-600	<ul style="list-style-type: none"> • High temperature strength • High temperature salt damage resistance • Workability 	441, 409, 321, 309
	Catalyst carrier	1200-1000		
Centre pipe		600-400	<ul style="list-style-type: none"> • Salt damage resistance 	304, 409, 441
Main muffler		400-100	<ul style="list-style-type: none"> • Corrosion resistance at inner surface (condensate) • Corrosion damage at outer surface (salt damage) 	409, 434, 436, 430Ti, 321, 304
Tail end pipe		400-100		304, 316

Type 441 is usually welded autogenously (without filler metal) in thin sections. If filler metal is added, austenitic consumables are preferred because of the additional toughness imparted to the weld. If ferritic stainless steel consumables are used, the composition of the filler material has to be compatible with that of the base metal, and the consumable should preferably contain a low interstitial content and a modest amount of stabilising elements. Commonly used filler metals for gas tungsten arc welding and gas metal arc welding of type 441 include austenitic ER308LSi wires or ferritic ER430LNb and ER439 consumables (electrode classification according to AWS A5.9 [13]). Shielded metal arc welding is only recommended for repair operations; a suitable electrode is austenitic type E308L stainless steel electrodes (classification in accordance with AWS A5.4 [14]).

2.4 EMBRITTLEMENT DURING THE WELDING OF FERRITIC STAINLESS STEELS

Ferritic stainless steels, including type 441, are more difficult to weld successfully than the more widely used austenitic grades of stainless steel. The ferritic grades are prone to embrittlement during welding. Embrittlement may be due to carbide and nitride precipitation during the weld thermal cycle, precipitation of brittle intermetallic compounds (such as Laves phase and/or sigma phase) in the weld metal and heat-affected zone, rapid grain growth and loss of corrosion resistance through sensitisation. Each of these factors are considered in more detail below.

2.4.1 Precipitation of carbides and nitrides

The presence of interstitial atoms, particularly carbon and nitrogen, in solid solution in ferritic stainless steels tends to decrease toughness through a mechanism of dislocation locking. The interstitial atoms preferentially diffuse to dislocations, making it difficult for the dislocations to move; therefore the interstitial elements increase the flow stress [15].

Ferritic stainless steels, however, have a body centred cubic (BCC) crystal structure with a low solubility for interstitial atoms. Figure 2.3 shows the solubility of carbon and nitrogen in a 26 wt% chromium ferritic stainless steel. It is evident that the carbon solubility is low and decreases with a decrease in temperature. According to Figure 2.3, the carbon solubility in a 26% chromium ferritic stainless steels falls from approximately 400 ppm at 1100°C to less than 50 ppm at 950°C. The solubility of carbon and nitrogen decreases with increasing chromium levels, and therefore the highly alloyed ferritics have very low interstitial solubility. Any excess carbon tends to precipitate as carbides or carbonitrides. Nitrogen behaves in a similar manner, but displays slightly higher solubility due to its smaller atom size than that of carbon [15].

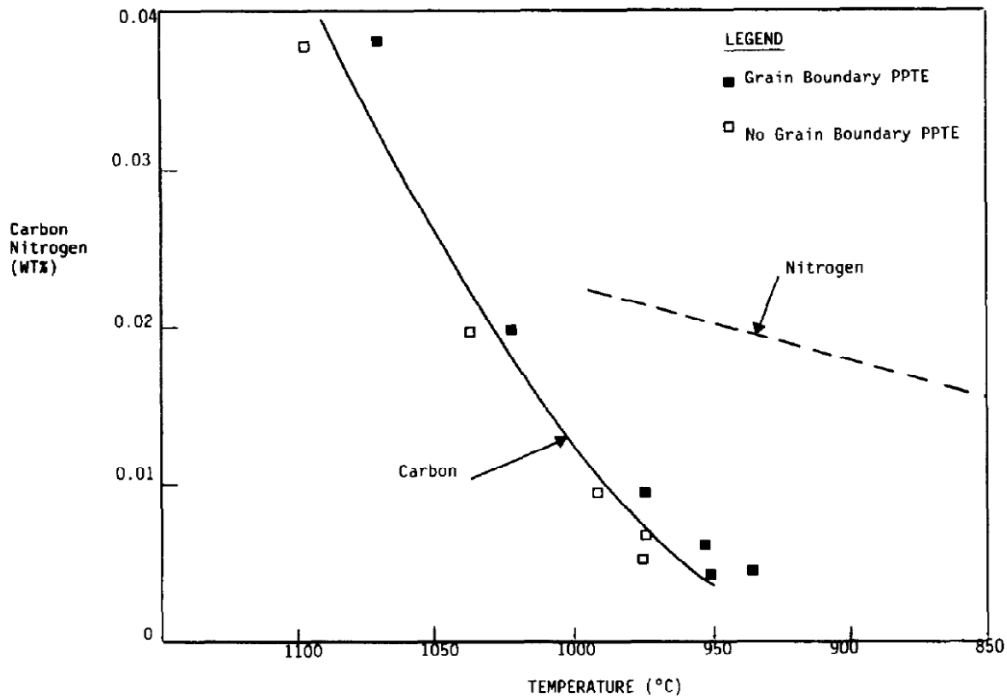


Figure 2.3: The solubility of carbon and nitrogen in a 26 wt% Cr ferritic stainless [15].

As the solubility is exceeded, the interstitial atoms are rejected from the matrix and diffuse to high energy sites, including grain corners, grain boundaries and dislocations. At these sites, carbon and nitrogen precipitate as carbides, nitrides and carbonitrides. These precipitates are known to increase the ductile-to-brittle transition temperature (DBTT) of ferritic steels. Figure 2.4 shows Charpy impact transition curves for 17 wt% chromium ferritic stainless steels with different carbon and nitrogen contents. It is evident that as the carbon content increases, the DBTT increases. The upper shelf energy is also shown to decrease with an increase in carbon and nitrogen content [15]. The influence of carbide precipitation on the corrosion resistance of the alloy is considered in §2.4.5.

The cooling rate through the critical temperature range where precipitation takes place has a significant effect on the room temperature toughness. Figure 2.5 shows impact curves for a 25 wt% chromium ferritic stainless steel after cooling at various rates from 850 °C. It is evident that rapid cooling improves the toughness of the alloy. This is attributed to the fact that fast cooling suppresses precipitation by reducing the time spent in the critical temperature range where precipitation occurs [15].

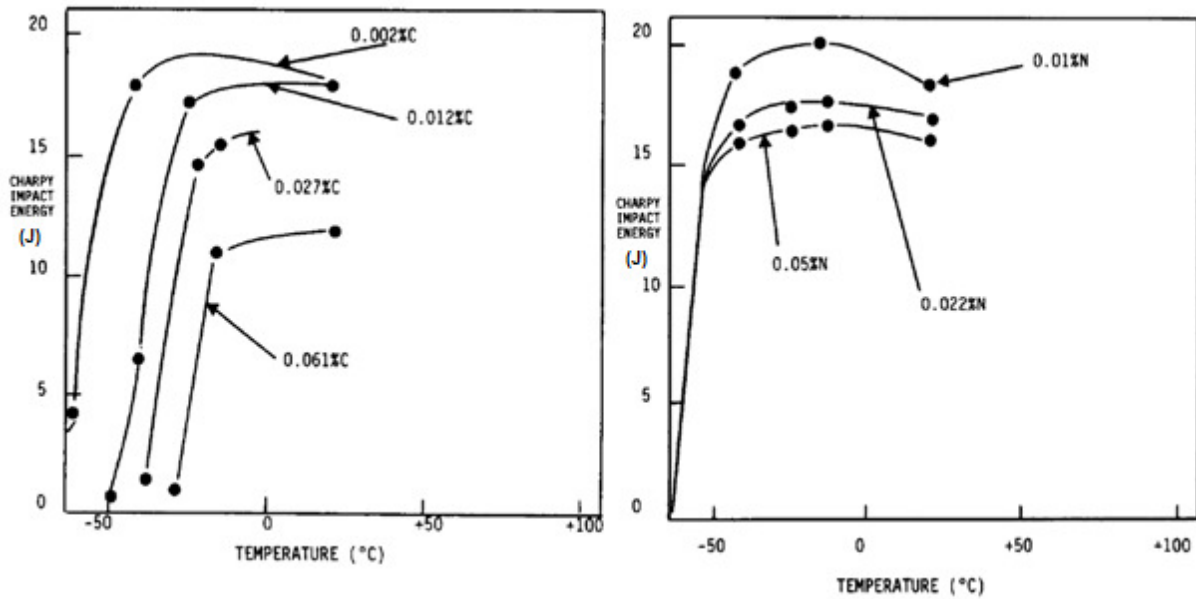


Figure 2.4: The effect of carbon and nitrogen on the Charpy impact toughness (on the vertical scale) of 17 wt% chromium ferritic stainless steel isothermally treated at 815 °C [15]. Test specimens were 55 × 10 × 10 mm notched Charpy samples.

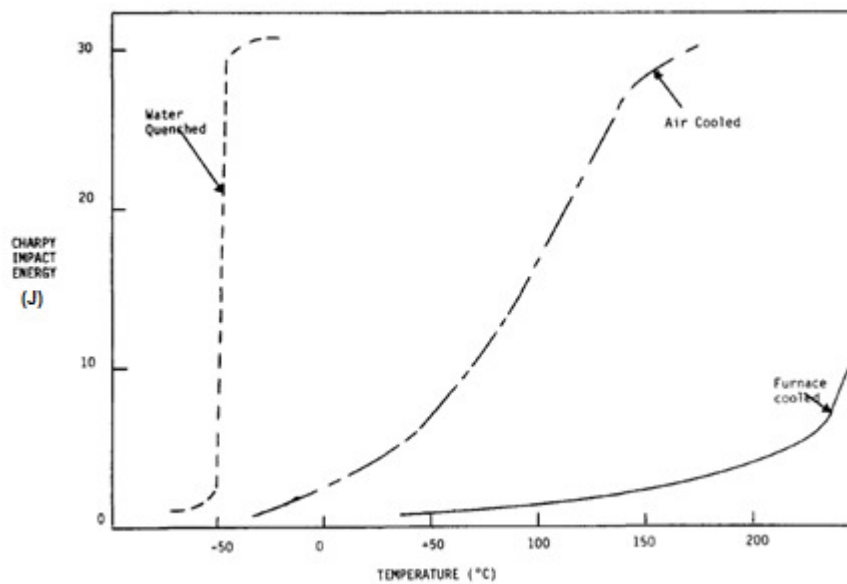


Figure 2.5: Impact curves for a Fe-25% Cr alloy cooled at different rates from 850 °C [15]. Carbon and nitrogen content not noted. Test specimens were 55 × 10 × 10 mm notched Charpy samples.

Rapid cooling may, however, decrease toughness at high interstitial contents and chromium levels. Due to the low solubility of carbon and nitrogen in ferrite, there is an increased driving force for precipitation in high chromium alloys. The cooling rate affects the morphology and distribution of the precipitates. Rapid cooling promotes

the formation of finely dispersed intragranular carbonitrides. This form of dispersed intragranular precipitation makes it difficult for dislocations to move, thus increasing the flow stress. Rapid cooling may also cause supersaturation of the interstitial atoms in the ferrite, strengthening the matrix through solid solution strengthening. These atoms cluster around dislocation lines, increasing the lattice friction stress and the flow stress. At high interstitial contents, furnace cooling improves toughness. Carbon and nitrogen are given enough time to diffuse to the desired high energy sites, normally the grain boundaries. Grain boundary precipitation therefore takes place instead of intragranular precipitation. Intergranular precipitation does not increase the flow stress to the same extent as intragranular precipitation, thereby improving toughness properties [15].

2.4.2 The effect of titanium and niobium on the mechanical properties of ferritic stainless steels

Dual-stabilised ferritic stainless steels such as type 441 are alloyed with titanium and niobium to increase sensitisation resistance. Titanium is a ferrite-forming element, which means it forms and stabilises ferrite at the expense of austenite. It is highly reactive and tends to form at high temperatures titanium carbonitrides (TiCN) in the presence of nitrogen and carbon. In the presence of carbon, titanium forms large cuboidal titanium carbide precipitates which decrease impact toughness by acting as crack initiators. Titanium is a solid solution strengthener, therefore it tends to decrease ductility and increase the DBTT [16].

The influence of niobium in stainless steel on mechanical properties and weldability is, however, not well understood. Niobium is mainly added to ferritic stainless steels to improve high temperature strength [10] and corrosion resistance [16]. As described earlier, type 441 ferritic stainless steel is used primarily in catalytic converters in automobile exhaust systems where good high temperature strength is essential. Since ferritic stainless steels generally display lower high temperature strength than corresponding austenitic grades, niobium is added to improve high temperature strength through solid solution strengthening. Figure 2.6 shows the relationship between high temperature strength and aging time at 700 °C in niobium-containing steels. The steel containing 0.8 wt% Nb has the highest yield strength in the as-solution treated, followed by steel containing 0.3 wt% Nb. The loss of high

temperature strength with increasing aging time is due to the loss of niobium in solution due to precipitation and coarsening of niobium containing precipitates in the steels [17].

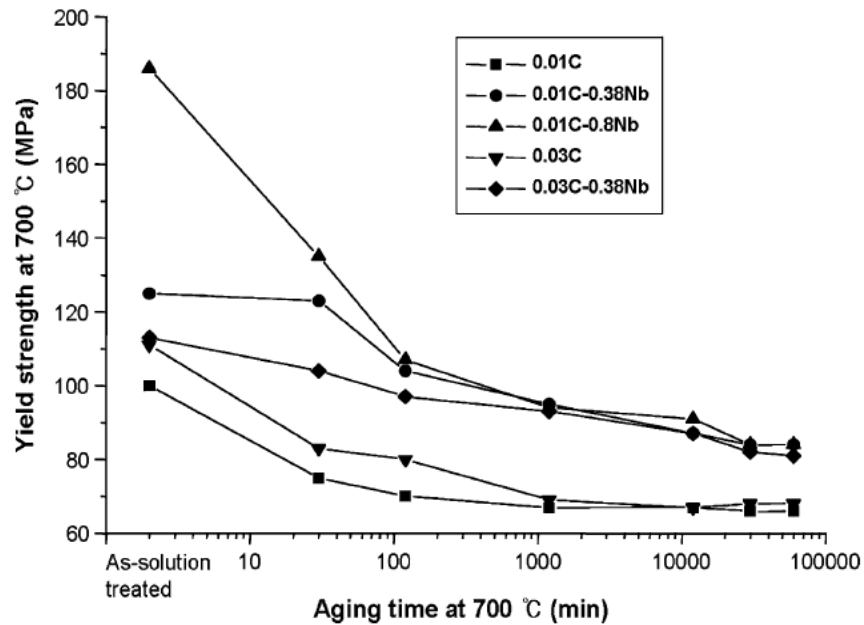


Figure 2.6: Relationship between high temperature strength and aging time at 700 °C in 15Cr niobium-containing steels [17]. Solution treatment was performed at 1250 °C for 10 min and followed by water quenching.

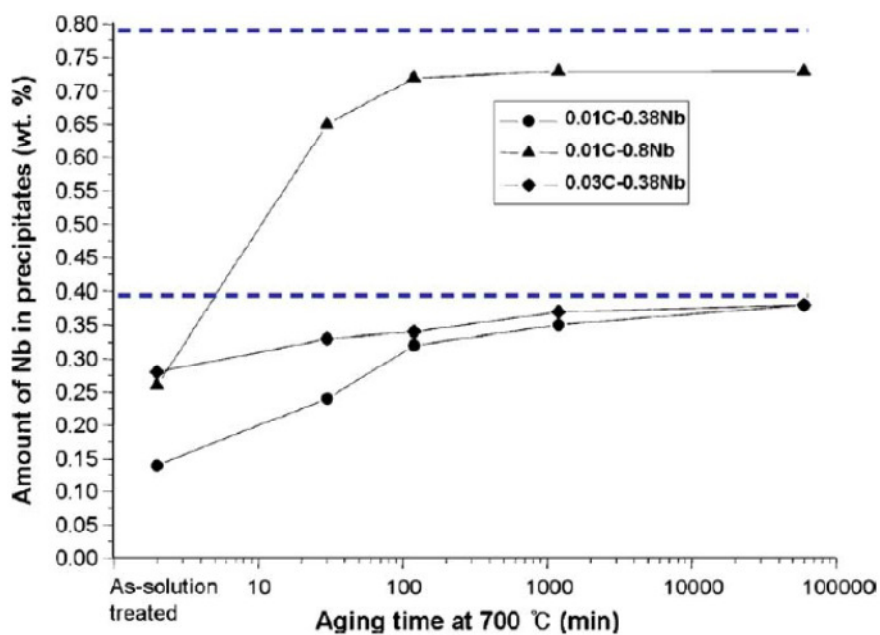


Figure 2.7: Change of Nb amount in precipitates measured by ICP with aging time [17].

Figure 2.7 below shows the change of Nb amount in precipitates as a function of aging time at 700 °C. It is evident from figure 2.7 that the precipitates are enriched with niobium as the aging time increases. As a consequence of the enrichment of precipitates with niobium during aging at 700 °C, niobium is precipitated out of solution. The loss of niobium from solution is therefore associated with the loss of solid solution strengthening and high temperature strength.

It is also evident from figure 2.7 that the niobium content in the precipitates in the 0.01C-0.8Nb steel reaches a constant value of 0.72 wt% Nb after approximately 100 minutes. After approximately 100 minutes, precipitation of niobium out of solution ceases. Figure 2.7 shows further decrease in high temperature strength of this steel after 100 minutes of aging. The additional decrease in high temperature strength after 100 minutes is possibly due to coarsening of niobium carbides and niobium-containing precipitates. Coarser precipitates are not as effective in raising lattice friction or locking dislocations as fine precipitates [15].

Niobium may also embrittle ferritic stainless steels through intermetallic Laves phase precipitation [18], as considered below.

2.4.3 Laves phase precipitation

Laves phase is an intermetallic compound of iron and niobium, Fe_2Nb . The iron may be partially substituted by chromium and the niobium by titanium to form a $(Fe,Cr)_2(Nb,Ti)$ phase. Laves phase is needle- or rod-like and is known to precipitate preferentially at grain boundaries and dislocation lines [9].

Figure 2.8 shows experimental data and Thermo-Calc™ predictions of the equilibrium weight fraction Laves phase as a function of temperature in type 441. Sello and Stumpf confirmed that Laves phase is stable at temperatures between approximately 600 °C and 900 °C in type 441 [19].

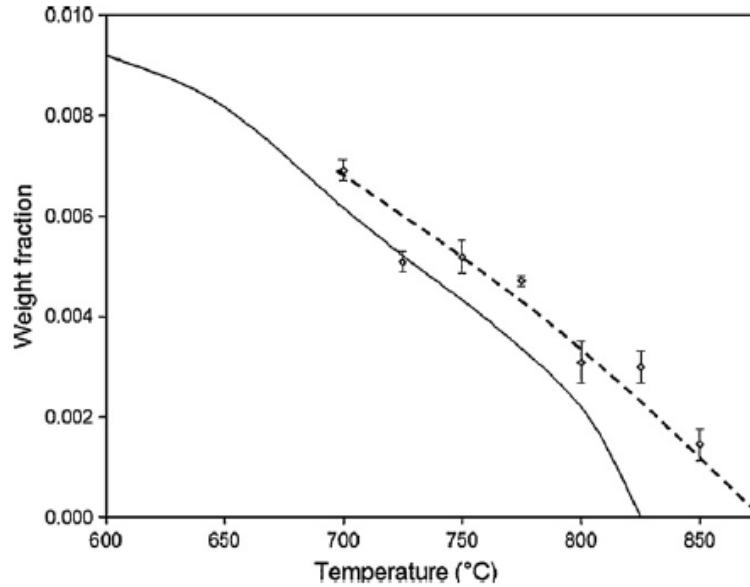


Figure 2.8: Comparison between experimental (dotted line) and predicted by Thermo-Calc™ (solid line) weight fractions of Laves phase in type 441 stainless steel [19].

The effect of temperature on the transformation kinetics of Laves phase was also investigated by Sello and Stumpf [19]. Figure 2.9 shows the time-temperature-transformation (TTT) diagrams for Laves phase formation in type 441 ferritic stainless steel. The TTT diagram displays two noses, at approximately 825°C and 650-670°C. These two noses on the TTT diagram may suggest two different nucleation mechanisms at these temperatures. It was observed that in the temperature range between 650°C and 670°C, Laves phase precipitates primarily on dislocation lines. At 825°C, however, Laves phase precipitates at grain boundaries. The highest transformation rates were observed at temperature between 650°C and 670°C, where 5% transformation required approximately 600 seconds.

Sello and Stumpf [19] also investigated the effect of ferrite grain size on the transformation kinetics of Laves phase. It is evident from Figure 2.10 that fine ferrite grains show faster transformation rates than coarse grains. This is attributed to the larger grain boundary area associated with finer grain sizes. A larger grain boundary area provides more nucleation sites for Laves phase formation.

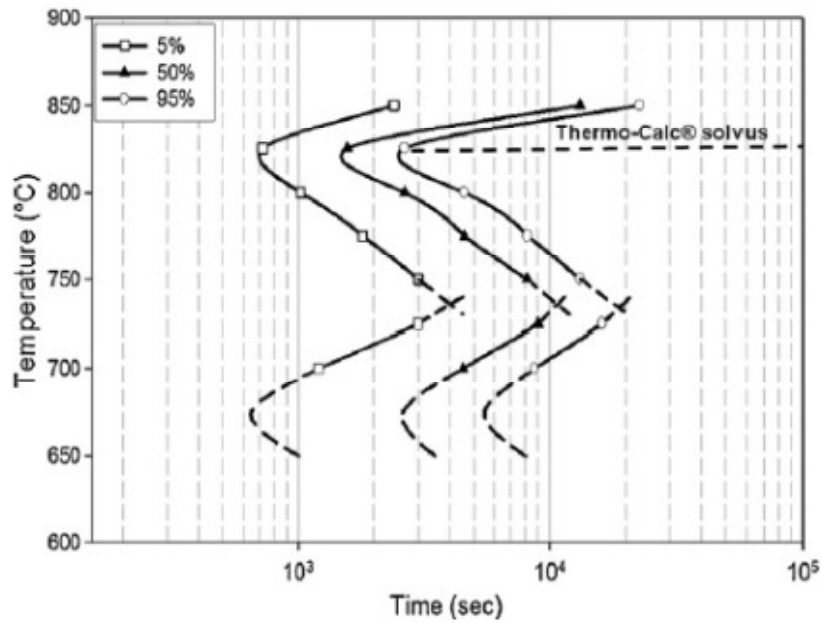


Figure 2.9: A time-temperature-precipitation diagram for Laves phase formation in type 441 steel [19].

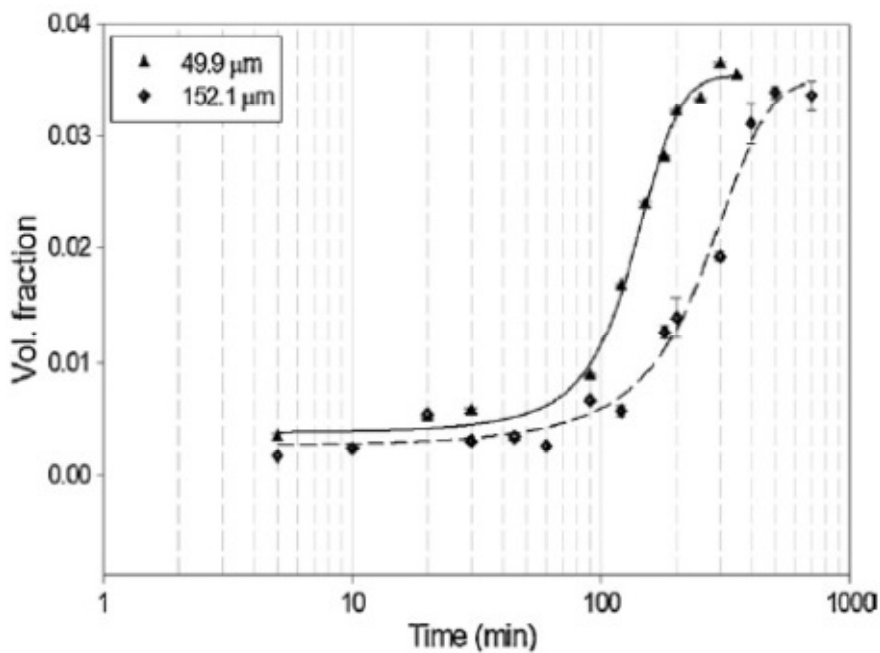


Figure 2.10: The effect of grain size on the kinetics of Laves phase transformation in type 441 stainless steel [18].

As alluded to before, niobium plays an important role in the precipitation of Laves phase. Sello and Stumpf [19] studied the effect of niobium content on Laves phase precipitation in type 441 ferritic stainless steel, with the results shown in Table 2.6. It was found that higher niobium contents in the steel increase the equilibrium volume fraction of Laves phase and accelerates the transformation. Molybdenum was found

to delay Laves phase precipitation by retarding niobium diffusion to the nucleation sites [9].

Table 2.6: Comparison between the thermodynamically predicted and experimentally measured Laves phase weigh fractions in type 441 after annealing at 750 °C [9].

Alloy	Weight fraction Laves phase	
	Thermo-Calc™	Experimental values
17.89Cr - 0.444Nb - 0.153Ti	0.041	0.054
17.9Cr - 0.39Nb - 0.171 Ti	0.001	0.013

The embrittlement caused by Laves phase in ferritic stainless steels has been reported by a number of authors [8,20]. Figure 2.11 shows the effect of annealing temperature on the tensile strength and elongation of type 441 ferritic stainless steel. It is evident that as-received material has a higher yield strength and ultimate tensile strength than annealed steel. This is due to the fact that the as-received steel contained Laves phase that increased the hardness and strength [20]. At annealing temperatures of 850 °C to 900 °C, the Laves content decreased, resulting in a reduction in strength and an increase in ductility. This confirms that the presence of Laves phase increases strength and reduces ductility. Above 900 °C, the solvus temperature of Laves phase in this alloy, the mechanical properties remained constant.

The impact toughness of ferritic stainless steel is also influenced by the presence of Laves phase. Figure 2.12 shows the Charpy impact energy of type 441 as a function of test temperature for specimens annealed at various temperatures. The specimen annealed at 850 °C exhibits a DBTT of about 5 °C and a maximum toughness of about 60 J at 25 °C. The specimen annealed at 700 °C contains the highest volume fraction of Laves phase in the microstructure and displays the lowest impact toughness. Reducing Laves phase therefore tends to result in improved toughness properties in type 441. The specimen annealed at 950 °C displays the highest DBTT due to excessive grain growth [9].

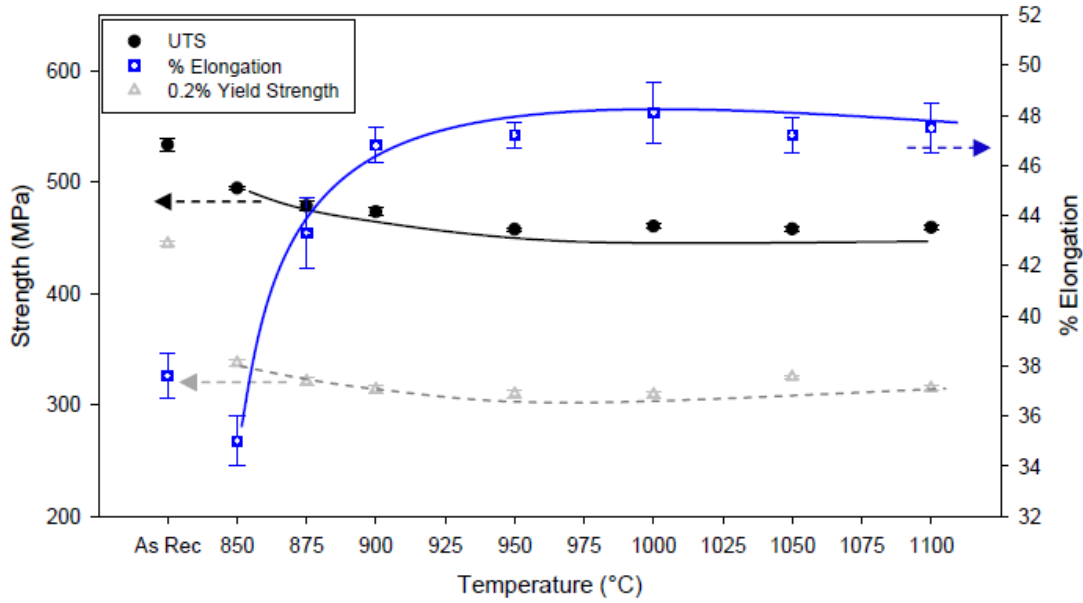


Figure 2.11: The effect of annealing at temperatures above 850 °C on the tensile strength and elongation of type 441 steel [20].

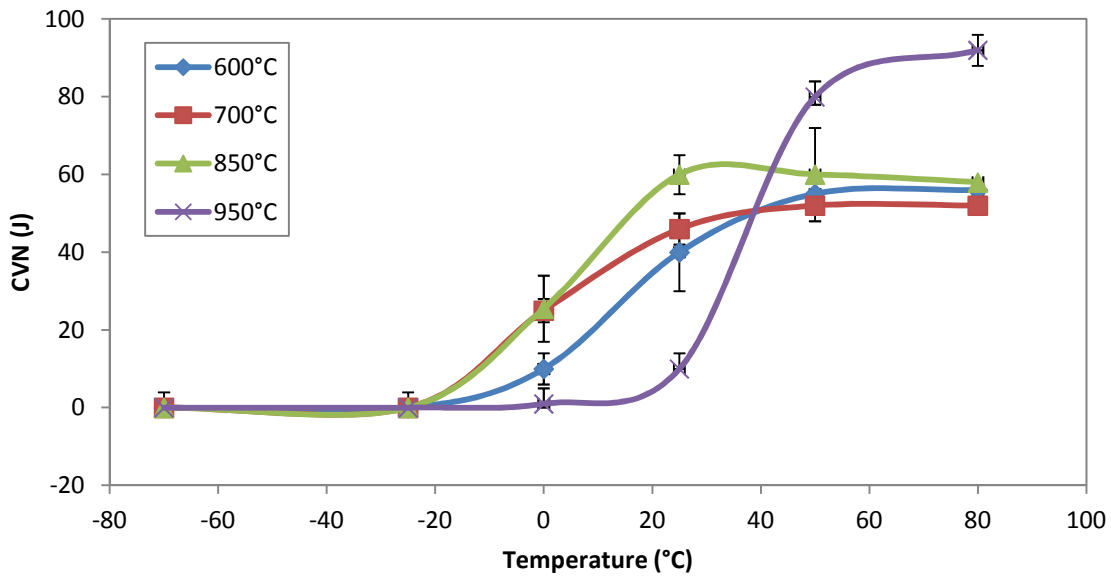


Figure 2.12: Charpy impact energy as a function of the test temperature for type 441 ferritic stainless steel annealed at different temperatures [9].

The impact toughness of type 441 is affected by the cooling rate through the critical temperature ranges where Laves phase precipitation takes place (shown in Figure 2.9). Figure 2.13 displays the room temperature Charpy impact toughness of type 441 stainless steel after heating to 850°C, followed by cooling at different rates to 600°C before quenching to room temperature. Slower cooling rates through the

temperature range between 850°C to 600°C resulted in lower impact toughness as more time was available to form Laves phase in the microstructure.

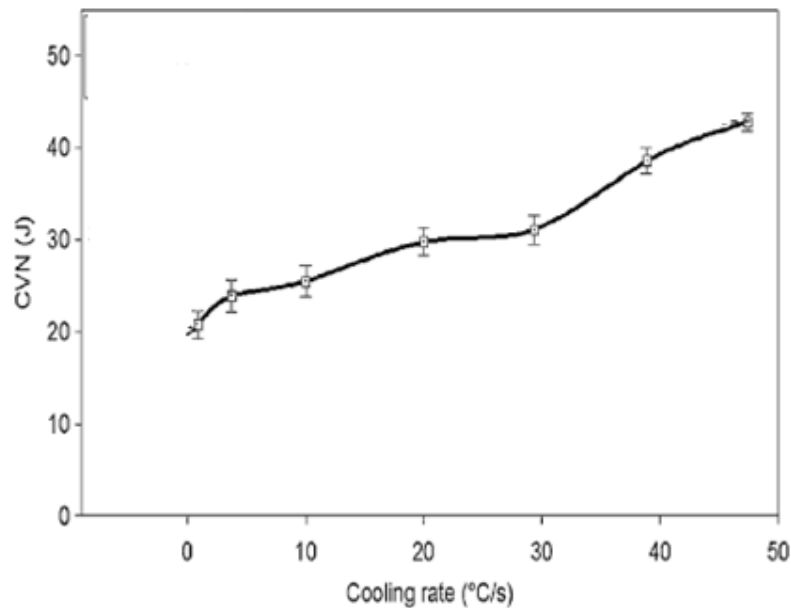


Figure 2.13: The effect of linear cooling rate in °C/s on the room temperature impact toughness of specimens cooled from 850 °C [9]. Test specimens were 55 × 10 × 10 mm notched Charpy samples.

Sigma phase (σ) precipitation also causes high temperature embrittlement in ferritic stainless, as considered below.

2.4.4 Sigma phase precipitation.

Although sigma phase precipitation has been introduced earlier in § 2.1 in the Fe-Cr binary system, this section describes the precipitation behaviour of sigma phase in ferritic stainless steels.

Sigma phase is an intermetallic compound of iron and chromium, FeCr. It has a tetragonal crystal structure. The σ phase transforms from ferrite between 600 and 800 °C. In steels containing more than 20 wt% Cr, it is difficult to prevent σ phase precipitation [5]. It can be precipitated at high temperatures during welding, rolling, casting, forging and aging. The presence of σ phase cause deterioration of mechanical properties, corrosion resistance and weldability [5].

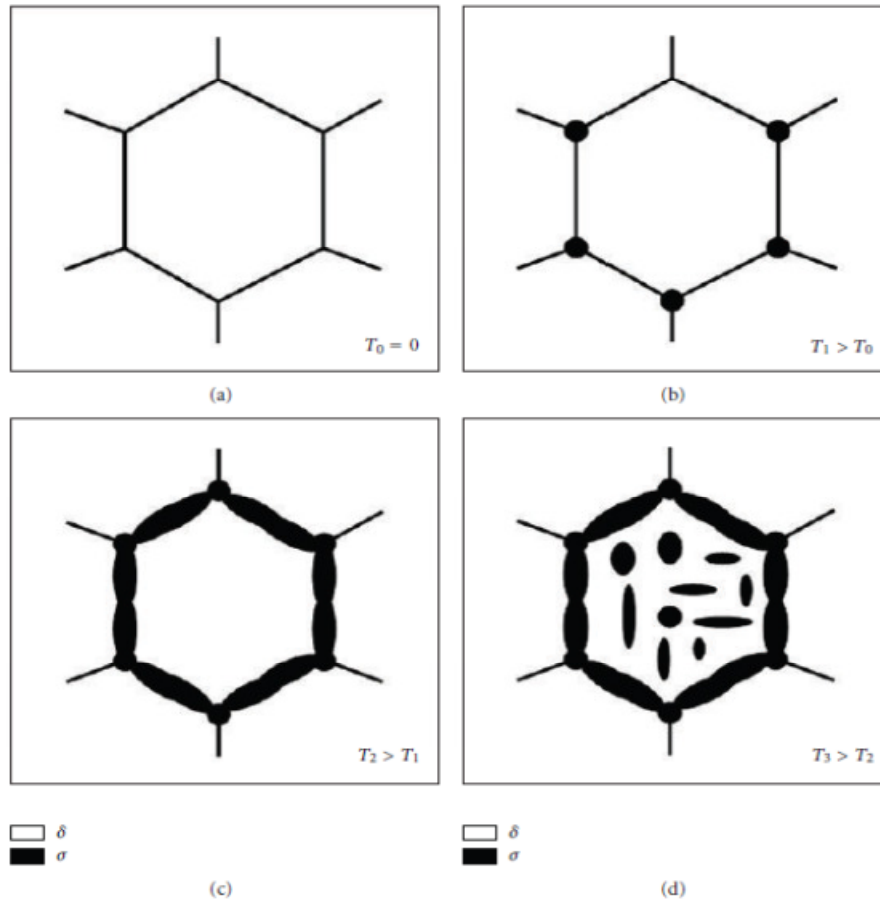


Figure 2.14: Mechanism of σ phase precipitation in ferritic stainless steel (DN 1.4575) [5].

Figure 2.14 (a)-(d) shows the precipitation mechanism of the σ phase in ferritic stainless steel as a function of aging temperature. The microstructure consists only of ferrite and no σ phase without preheating (T_0). When the aging temperature is increased to T_1 , σ phase occupies firstly the triple points of the ferrite grain boundaries. When the aging temperature is increased to T_2 , σ phase grows completely on the ferrite grain boundaries. Finally, when the aging temperature is increased to T_3 , σ phase precipitation extends to intragranular in the ferrite matrix [5].

The role of $M_{23}C_6$ carbides on σ phase precipitation have been investigated by different authors and it seems a consensus has not yet been reached [31]. Redjaimia et al [32] studied the decomposition of delta ferrite (δ) in a duplex stainless steel. It was discovered that σ phase nucleated on the intergranular (δ/δ) $M_{23}C_6$ carbides and interface of ferrite with austenite. It was found at early stages $M_{23}C_6$ carbides appear on δ/δ grain boundaries. Their precipitation prior to other phases is due to fast diffusion rates of interstitial carbon. Chen and Yang [33] also observed that Cr- and

Mo-rich σ phase preferentially nucleated at the preformed carbides, which were located on grain boundary and within ferrite grain (see figure 2.15). However, a recent study [34] on the precipitation sequence of 316L steel at lower temperatures (< 500 °C) discovered that formation of σ phase preceded that of $M_{23}C_6$ carbides.

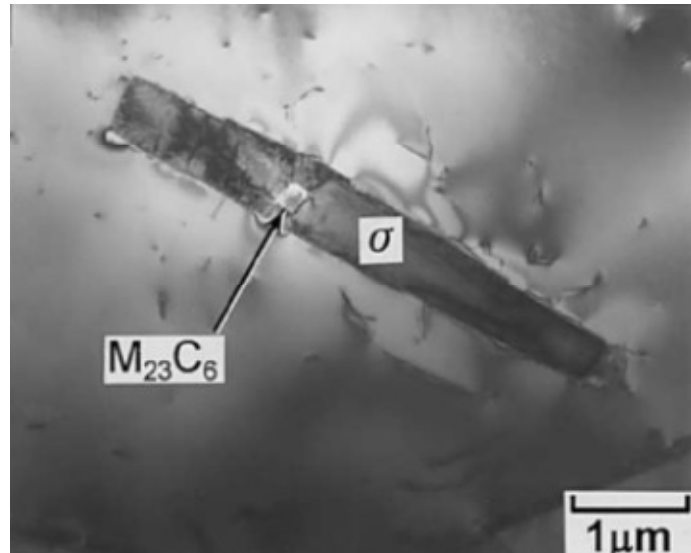


Figure 2.15: TEM micrograph showing intragranular σ phase induced on a preformed $M_{23}C_6$ particle within the δ -ferrite [33].

2.4.5 Grain growth

Ferritic stainless steels can also experience embrittlement as a result of grain growth on exposure to high temperatures. Fine grain sizes are known to produce tough, ductile and strong microstructures. The driving force for grain growth at higher temperatures is a decrease in the surface free energy, as shown in equation (2.2). As the average grain size increases, the surface free energy, ΔG in equation (2.2), decreases [21].

$$\Delta G = \frac{2\gamma_{gb}}{d} \quad \dots (2.2)$$

where γ_{gb} is the surface tension and d is the average grain size.

The presence of precipitates in the microstructure tends to hinder grain growth. This phenomenon is known as grain pinning. The theoretical maximum grain size is given by equation (2.3). Finer precipitates and a higher volume fraction of particles tend to be more effective at pinning the grain boundaries. Solute atoms that preferentially

segregate to grain boundaries, such as niobium, add drag that also inhibits grain growth [21].

$$d_{max} = \frac{4r}{3V_f} \quad \dots(2.3)$$

where r is the radius of the precipitate and V_f is the volume fraction of particles.

Olivier [11] studied grain growth in type 441 ferritic stainless steel and observed grain growth at temperatures above 925°C (see Figure 2.16). Grain growth appears to be sluggish at 925°C, but the grain size rapidly increases above this temperature. At temperatures above 1100°C, excessive grain growth takes place.

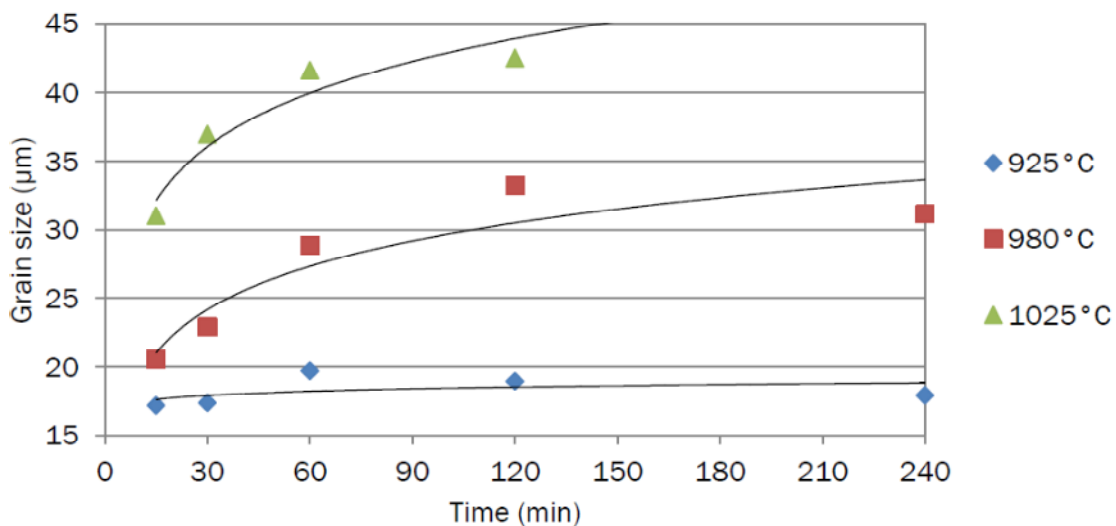


Figure 2.16: The effect of annealing temperature on the ferrite grain size of 441 type stainless steel [11].

During welding, the base material adjacent to the fusion line is heated to temperatures above which grain growth occurs. This effect is particularly pronounced in ferritic stainless steel, as there are no solid state phase transformations to inhibit grain growth on heating and cooling. Figure 2.17 shows the effect of weld heat input on the grain size in the heat-affected zone of EN 1.4512 ferritic stainless steel. It is evident that higher heat inputs (and therefore slower cooling rates) result in coarser grain sizes. During high heat input welding, the weld metal and heat-affected zone spend more time at temperatures (temperatures above 925°C) where unrestricted grain growth occurs. Low heat input welding (along with the use of low or no preheat, small diameter electrodes and low interpass temperatures) is normally

recommended for welding ferritic stainless steels to keep the weld thermal cycle as short as possible.

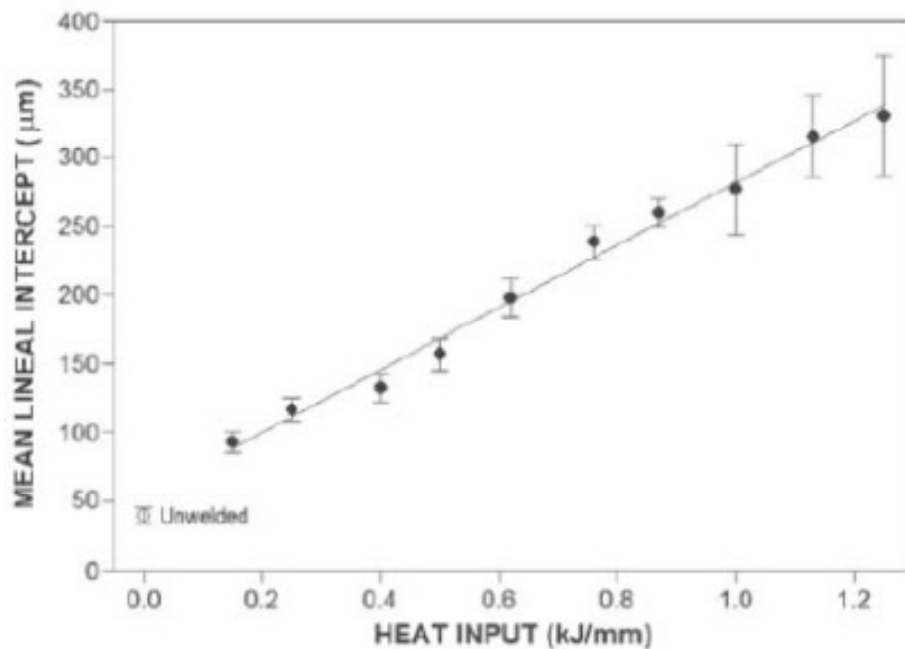


Figure 2.17: The average grain diameter in the heat-affected zone of EN 1.4512 ferritic stainless steel as a function of heat input during welding [22].

As noted above, the grain size of the base material adjacent to the fusion line coarsens during welding. Since the grain size influences the toughness and ductility of the steel, the properties of the material in this region are expected to be adversely affected. Figure 2.18 shows the effect of grain size on the impact toughness of a ferritic stainless steel containing 25 wt% chromium. It is evident that coarser grain sizes increase the DBTT and decrease the upper shelf energy [15].

The cooling rate determines the amount of time spent in the critical temperature range where grain growth occurs. Figure 2.19 shows the effect of linear cooling rate on the room temperature impact toughness of specimens cooled from 850°C and 950°C, respectively, in type 441 ferritic stainless steel. The specimen cooled from 850°C at a slow cooling rate displays poor impact toughness due to Laves phase formation. The sample cooled from 950°C also displays poor impact properties due to excessive grain growth. The influence of grain growth on impact toughness, however, appears to be more significant than that of Laves phase formation [9].

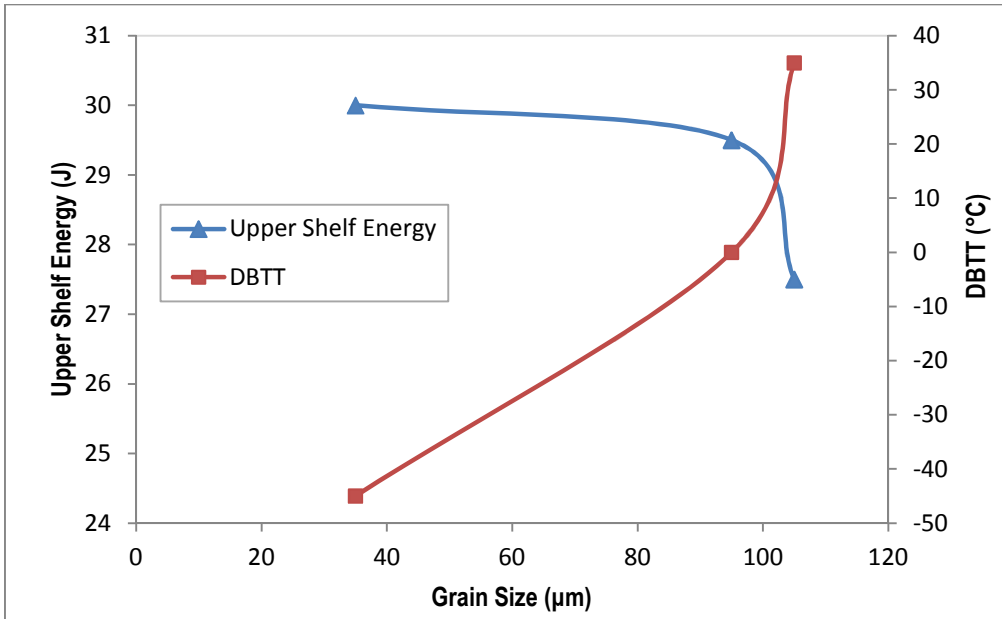


Figure 2.18: The effect of grain size on impact toughness of ferritic stainless steels [15].

The weld pool typically solidifies and cools rapidly. Depending on the heat input, fine grain sizes can be achieved in the weld metal if non-matching (austenitic) filler is used. Welding with a matching consumable or without filler metal (autogenous welding), however, results in coarse weld metal grain sizes due to epitaxial solidification at the fusion line.

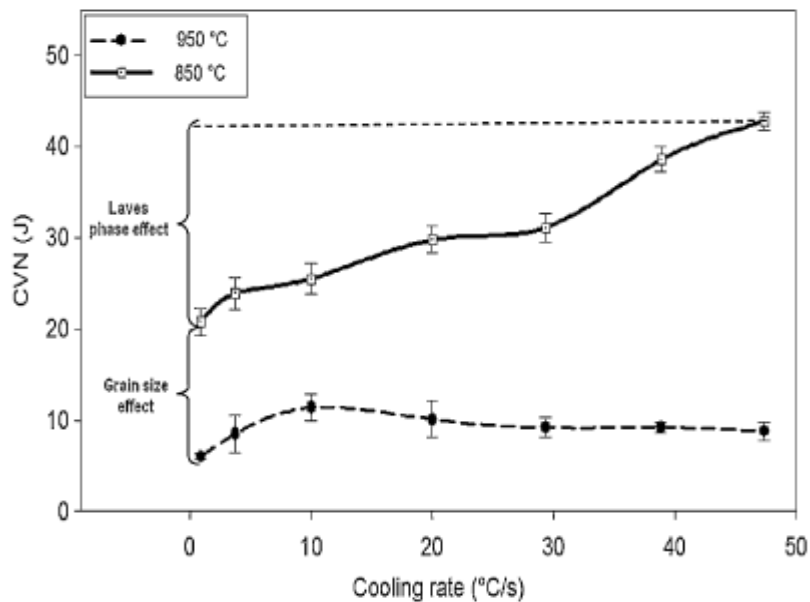


Figure 2.19: The effect of linear cooling rate in °C/s on the room temperature impact toughness of type 441 specimens cooled from 850 °C and 950 °C, respectively [9].

2.4.6 Sensitisation and intergranular corrosion in ferritic stainless steels

Ferritic stainless steels have a very low solubility for carbon at ambient temperature. The solubility of carbon in an 18% chromium ferritic stainless steel is approximately 0.05 wt% at 1000°C, but drops to almost 0% at ambient temperature. Excess carbon precipitates as chromium-rich carbides on cooling, mainly as $(\text{Cr,Fe})_{23}\text{C}_6$ or M_{23}C_6 , and in rare instances as M_7C_3 or M_6C . These carbides are highly enriched in chromium relative to the nominal composition of the stainless steel, with the chromium content of M_{23}C_6 and M_7C_3 carbides typically in the range of 42 to 65 wt%. Since the M_{23}C_6 carbide contains two to four times the amount of chromium in the base metal, the immediate surroundings of the precipitated carbides are depleted of chromium. The M_{23}C_6 carbides precipitate mainly at grain boundaries, resulting in chromium depleted zones adjacent to the grain boundary precipitates (as illustrated in Figure 2.20). If the chromium content of these depleted zones adjacent to the grain boundaries falls below approximately 12%, the corrosion resistance of these areas is significantly reduced, resulting in intergranular attack progressing along the chromium depleted grain boundaries. This results in destruction of the grain boundaries and may lead to grain dropping. Any excess nitrogen in the steel may precipitate as chromium-rich nitrides, mainly Cr_2N [1,2].

Trillo and Murr [35] studied M_{23}C_6 carbide precipitation behaviour on varying grain boundary misorientation in 304 stainless steels. It was found, in steels with low carbon, that precipitation M_{23}C_6 carbides nucleated on large grain boundary misorientation ($\Theta > 15^\circ$). It is evident from figure 2.21 that precipitation was not observed in the steel with misorientation $\Theta < 30^\circ$. It was also discovered that the density of precipitation also increased with the increase of grain boundary misorientation. Therefore M_{23}C_6 carbides will precipitate on high angle misorientation sites and will form dense series of heterogeneous nucleated individual nuclei of M_{23}C_6 carbides on these sites.

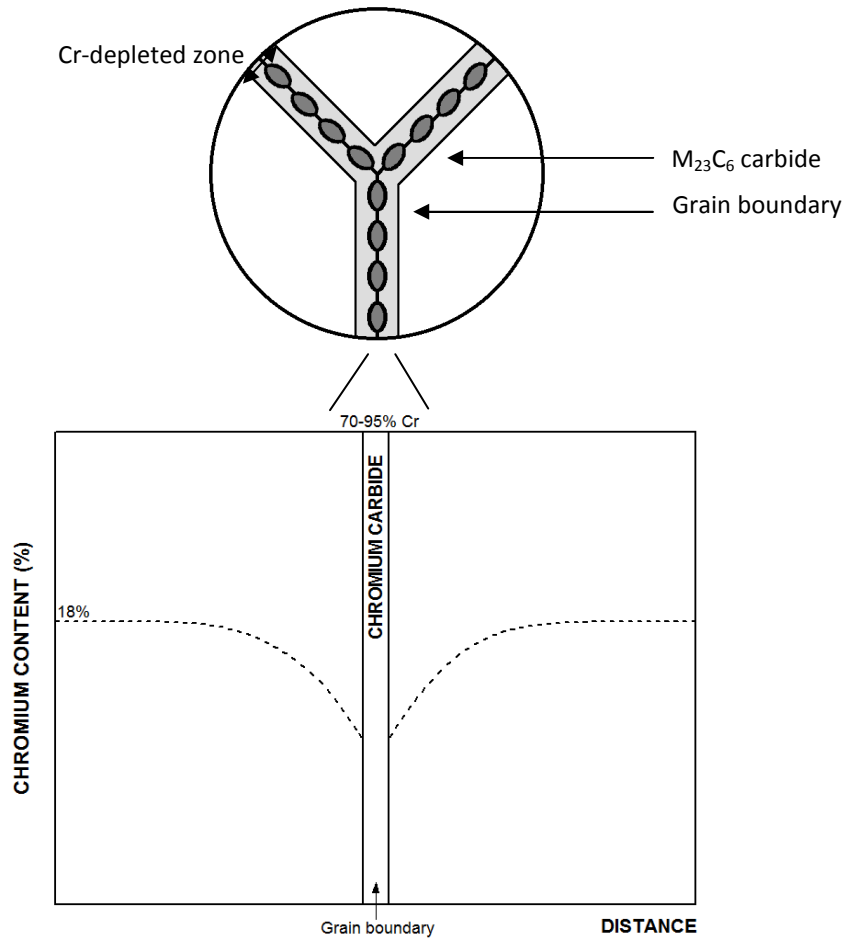


Figure 2.20: Schematic representation of carbide precipitation at a grain boundary and the chromium concentration profile at a ferrite grain boundary containing Cr-rich carbides [2].

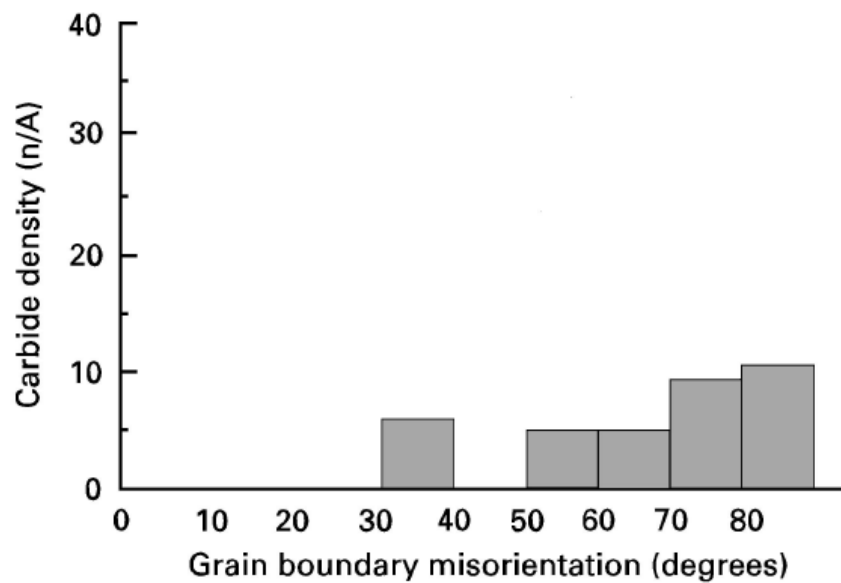


Figure 2.21: Carbide density measurements per unit length of the grain boundary at varying misorientation in a 304 stainless steel with 0.05 wt% C [35].

In ferritic stainless steels, sensitisation is usually induced by high temperature heat treatments and relieved by low temperature annealing treatments. The temperature range in which sensitisation takes place is the range in which there is a marked increase in the solubility of carbon and nitrogen in ferrite (usually higher than 925°C). On cooling, the ferrite becomes supersaturated in carbon and chromium-rich carbides or nitrides precipitate and leave a depleted matrix adjacent to the grain boundary, which now becomes susceptible to intergranular corrosion [1,2].

Due to the fast diffusion rates of chromium and carbon in ferrite, the sensitisation kinetics of ferritic stainless steels is so rapid that the material will only have chromium depleted grain boundaries when quenched from approximately 750°C or higher. If the sample is cooled slowly, it will become sensitised, but chromium will rapidly diffuse back during cooling to desensitise the grain boundaries (recovery). Annealing a sensitised ferritic stainless steel at temperatures of approximately 700°C to 800°C will also cause chromium to diffuse back to the depleted regions. Most ferritic stainless steels are supplied in the recovered condition. The steel can only resensitise if heated to a sufficiently high temperature (higher than about 925°C) for the carbides to redissolve, followed by rapid cooling [1,2].

If welds are heat treated in the same way as the base metal, i.e. solution annealed and quenched, they usually perform in the same manner as a steel grade of similar analysis with regard to carbide precipitation and sensitisation. In most cases, however, it is not possible to subject stainless steel welds to such annealing procedures and the weld is placed into service in the as-welded condition.

Sensitisation of ferritic stainless steels can be prevented by either reducing the carbon and nitrogen contents below certain levels, or by stabilising with titanium, niobium or tantalum. It has been reported that to avoid sensitisation, the combined carbon and nitrogen levels should not exceed 0.01% for a 17 wt% chromium ferritic stainless steel [23]. Excellent shielding during welding is required to avoid nitrogen contamination from the atmosphere. Since these very low levels of interstitial elements are difficult to attain, the low interstitial approach for avoiding sensitisation has been largely abandoned in favour of stabilisation.

2.4.6.1 Stabilisation in ferritic stainless steels

Stabilisation in stainless steel refers to the addition of an alloying element with a strong affinity for carbon and nitrogen that forms carbides and nitrides that are more stable than those formed by chromium. These alloy carbides form at higher temperatures than chromium carbides, and if enough carbon and nitrogen are tied up forming these precipitates, the formation of chromium-rich carbides and nitrides at lower temperatures, and therefore sensitisation, can be prevented [2].

Figure 2.22 shows the calculated solvus temperatures of various metal carbides and nitrides in iron. Although alloying with chromium tends to depress the solvus temperatures (as shown for TiN), it is evident that Ti, Nb, Zr, Ta and V form stable carbides and nitrides before chromium and are therefore potential stabilising elements. Tantalum is, however, rare and expensive, and not widely used. Zirconium is effective as a stabiliser, but is expensive and promotes the formation of brittle intermetallic compounds and needle-like carbonitrides, the presence of which negatively affects toughness. Vanadium forms carbides and nitrides at lower temperatures that are slightly more stable than those formed by chromium, but the diffusion of vanadium in iron is sluggish at precipitation temperatures and the reaction kinetics therefore not favourable for stabilisation [16].

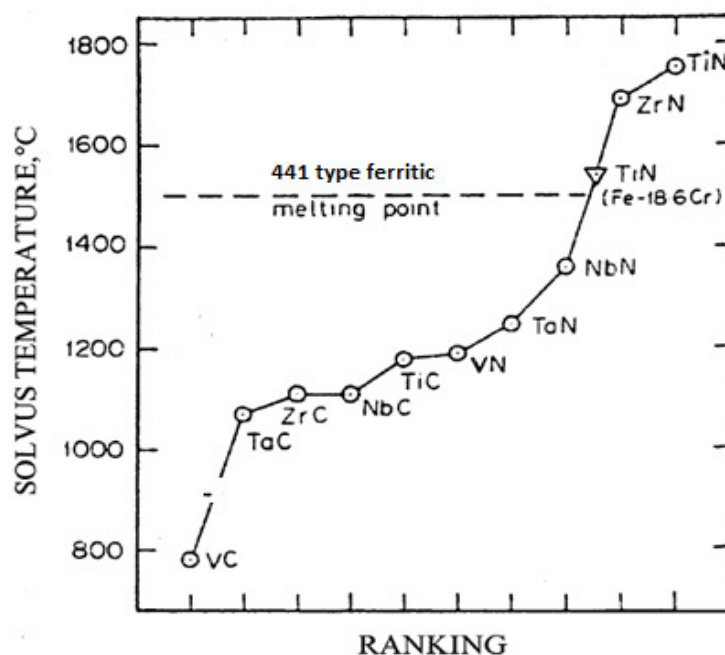


Figure 2.22: Calculated solvus temperatures in iron for MX (*M* is metal, *X* is C or N) stabiliser compounds [16].

2.4.6.2 Stabilisation with titanium

Titanium is the most widely used stabilising element in stainless steels. It can be added to the steel in the form of ferrotitanium, which is cheaper than any other stabilising addition. Titanium is highly reactive, forming at high temperatures stable titanium nitrides (TiN) in the presence of nitrogen, and titanium carbides (TiC) in the presence of carbon. In the presence of both carbon and nitrogen, titanium carbonitrides, Ti(C,N), form due to the mutual solubility of TiC and TiN. The titanium requirement for stabilisation depends on the carbon and nitrogen contents in the steel, with the stoichiometric requirement described by equation (2.4) [16].

$$\text{Ti} = 4\text{C} + 3.4\text{N} \quad \dots (2.4)$$

Higher concentrations of titanium are, however, required for full stabilisation. Some of the titanium reacts with sulphur in the steel, and titanium may also be present in solid solution in the matrix. In practice, the generally accepted titanium content required to fully stabilise a ferritic stainless steel is given by equations (2.5) or (2.6).

$$\text{Ti} = 0.2 + 4(\text{C} + \text{N}) \quad \text{or} \quad \dots (2.5)$$

$$\text{Ti} = 0.15 + 3.7(\text{C} + \text{N}) \quad \dots (2.6)$$

Titanium nitride and titanium carbide precipitates are extremely stable in iron and only dissolve at very high temperatures. As shown in Figure 2.22, titanium nitrides are stable at temperatures above the liquidus temperature of type 441 stainless steel (with the melting range of 441 superimposed on the solvus temperature diagram). Titanium nitrides therefore form in the melt and act as nucleation sites for heterogeneous solidification, promoting a fine grained equiaxed microstructure.

The addition of titanium to stainless steel, however, tends to result in the precipitation of coarse cuboidal carbonitrides, which may decrease the impact toughness of the steel by acting as preferential crack initiation sites. Over stabilisation with titanium can lead to solid solution strengthening, which reduces ductility and increases the ductile-to-brittle transition temperature. Titanium carbonitrides are readily attacked in highly oxidising media, which limits the use of these steels in highly oxidizing environments such as nitric acid solutions. Titanium additions promote poor surface finish in steel sheet [16]. It is also recognised that

sensitisation of titanium-stabilised stainless steels can occur on exposure to high temperatures, followed by rapid cooling (as described in §2.4.5.5).

2.4.6.3 Stabilisation with niobium

Niobium stabilisation offers a number of advantages over titanium stabilisation. Niobium is less reactive than titanium. Although it forms less stable carbides and nitrides, it still exhibits sufficient carbide and nitride stability in stainless steels to prevent sensitisation effects. The amount of niobium required for full stabilisation is given by equation (2.7).

$$\text{Nb} = 7.7\text{C} + 6.6\text{N} \quad \dots(2.7)$$

Although niobium is less likely to form oxides or sulphides than titanium and is unlikely to be taken into solid solution in significant amounts due to its low solubility in ferrite, it is widely agreed that the niobium content should be approximately ten times that of the combined interstitial content in the steel for optimal stabilisation [16].

Niobium forms small, spherical precipitates that do not decrease the impact toughness of stainless steel to the same extent as coarse cuboidal titanium carbide precipitates. A major advantage is that sensitisation in Nb-stabilised alloys does not occur as readily after rapid cooling from high temperatures than in Ti-stabilised alloys [16].

Niobium is, however, more expensive than titanium and has been shown to promote solidification cracking in stainless steels by forming low melting eutectic phases at the grain boundaries in the presence of sulphur and phosphorus during welding [24]. Niobium also promotes the formation of elongated columnar grains growing epitaxially from the weld centreline. This promotes solidification cracking and creates a plane of weakness. Alloys stabilised with titanium do not exhibit this solidification structure because the stable TiN precipitates provide nucleation sites in the melt that promote the formation of smaller equiaxed grains [16].

2.4.6.4 Dual-stabilisation with titanium and niobium

Dual-stabilisation, such as used in types 441 and 444 ferritic stainless steel, results in superior weld mechanical properties since the carbon and nitrogen are very effectively tied up (both titanium and niobium are efficient nitride and carbide

formers), while the negative effect of the individual stabilising additions are negated since each is present in smaller quantities [16].

The optimal dual-stabilisation content needed for full stabilisation is given by equations (2.8) and (2.9) [16].

$$\text{Ti+Nb} = 0.2 + 4(\text{C+N}) \quad (\text{minimum}) \quad \dots (2.8)$$

$$\text{Ti+Nb} = 0.8 \quad (\text{maximum}) \quad \dots (2.9)$$

Dual-stabilisation offers several advantages in ferritic stainless steel. Firstly, since the amount of titanium required to stabilise the steel is reduced, the risk of embrittlement caused by titanium is reduced. Secondly, the risk of solidification cracking is reduced. This is due to the fact that the amount of niobium required for full stabilisation is reduced. Lastly, in the case of dual-stabilisation with niobium and titanium, full stabilisation can be achieved with good mechanical properties [16].

2.4.6.5 Sensitisation in stabilised grades

Although more resistant to intergranular attack than unstabilised steels, sensitisation has been reported in stabilised ferritic grades [25-27]. As noted above, stabilised grades contain titanium and/or niobium that react with carbon and nitrogen to prevent sensitisation. During welding, high temperatures during the heating cycle may dissolve titanium and niobium precipitates. If the cooling rate is slow enough, the titanium and niobium carbonitrides reprecipitate on cooling. This removes carbon and nitrogen from solution and prevents the formation of chromium-rich carbides at lower temperatures. If cooling rates are rapid, however, enough time may not be available to allow reprecipitation of titanium and niobium carbonitrides at higher temperatures. At lower temperatures chromium carbides and nitrides form which sensitise the steel.

This sensitisation mechanism in stabilised stainless steels has been investigated for low heat input welding of various low chromium ferritic steels. Greeff and Du Toit [28] and Du Toit and Naudé [29] showed that titanium-stabilised EN 1.4003 ferritic stainless steel sensitises during the weld cooling cycle if welding is performed at heat inputs below approximately 0.5 kJ/mm. At heat inputs lower than 0.2 kJ/mm, sensitisation was reduced as the rapid heating and cooling rates did not allow

enough time for the titanium carbonitrides to dissolve. Van Niekerk and Du Toit [30] confirmed this mechanism for titanium-stabilised AISI 409 ferritic stainless steel.

Sensitisation of dual-stabilised ferritic stainless steels during low heat input welding has not been investigated to date.

2.5 REFERENCES

- [1] J. C. Lippold and D. J. Kotecki. "*Welding metallurgy and weldability of stainless steels*". Wiley-Interscience, Hoboken, NJ. 2005. pp. 87-137.
- [2] E. Folkhard. "*Welding metallurgy of stainless steels*". Springer Verlag, Vienna. 1988.
- [3] F.C. Hull. "*Effects of composition on embrittlement of austenitic stainless steels*". Welding Journal, vol. 52. 1973. pp. 104s-113s.
- [4] P.A. Blenkinsop and J. Nutting. "*Precipitation of the sigma phase in an austenitic steel*". Journal of the Iron and Steel Institute, vol. 205. 1967. pp. 953-958.
- [5] C.C. Hsieh and W.Wu. "*Overview of intermetallic sigma (σ) phase precipitation in stainless steels*". International Scholarly Research Network – Metallurgy, vol. 2012. 2012. Article ID: 732471.
- [6] ASTM A240/A240M-14. "*Standard Specification for Chromium and Chromium-Nickel Stainless Steel Plate, Sheet, and Strip for Pressure Vessels and for General Applications*". ASTM International, West Conshohocken, PA. 2014.
- [7] BS EN 10088-2:2005. "*Stainless steels. Technical delivery conditions for sheet/plate and strip of corrosion resisting steels for general purposes*". The British Standards Institution, London. 2005.
- [8] Columbus Stainless (Pty) Ltd company website at www.columbus.co.za.
- [9] M.P. Sello and W.E. Stumpf. "*Laves phase embrittlement of the ferritic stainless steel type AISI 441*". Materials Science and Engineering A, vol. 527, no. 20. 2010. pp. 5194-5202.
- [10] N. Fujita, K. Ohmura, M. Kikuchi, T. Suzuki, S. Funaki and I. Hiroshige. "*Effect of Nb on high-temperature properties for ferritic stainless steel*". Scripta Materialia, vol. 35, no. 6. 1996. pp. 705-710.

- [11] N. Olivier. “*Quantification of the grain growth anomaly found in AISI stainless steel 441 above 900 °C*”. Final-year project (unpublished research). Department of Materials Science and Metallurgical Engineering, University of Pretoria, South Africa. November 2011.
- [12] M.P. Sello. “*The Laves phase embrittlement of ferritic stainless steel type AISI 441*”. PhD Thesis. Department of Materials Science and Metallurgical Engineering, University of Pretoria, South Africa. 2009.
- [13] AWS A5.9/A5.9M:2006. “*Specification for bare stainless steel welding electrodes and rods*”. American Welding Society, Miami, FL. 2006.
- [14] AWS A5.4/A5.4M:2006. “*Specification for stainless steel electrodes for shielded metal arc welding*”. American Welding Society, Miami, FL. 2006.
- [15] A.C.T.M. van Zwieten and J. H. Bulloch. “*Some considerations on the toughness properties of ferritic stainless steels - A brief review*”. International Journal of Pressure Vessels and Piping, vol. 56, no. 1. 1993. pp. 1-31.
- [16] W. Gordon and A. van Bennekom. “*Review of stabilization of ferritic stainless steels*”. Materials Science and Technology, vol. 12. 1996. pp. 126-131.
- [17] G. M. Sim, J. C. Ahn, S. C. Hong, K. J. Lee and K. S. Lee. “*Effect of Nb precipitate coarsening on the high temperature strength in Nb containing ferritic stainless steels*”. Materials Science Engineering A, vol. 396, no. 1-2. 2005. pp. 159-165.
- [18] N. Fujita, K. Ohmura and A. Yamamoto. “*Changes of microstructures and high temperature properties during high temperature service of niobium added ferritic stainless steels*”. Materials Science and Engineering A, vol. 351, no. 1-2. 2003. pp. 272-281.
- [19] M. P. Sello and W. E. Stumpf. “*Laves phase precipitation and its transformation kinetics in the ferritic stainless steel type AISI 441*”. Materials Science and Engineering A, vol. 528, no. 3. 2011. pp. 1840-1847.
- [20] A. Bjärbo. “*Computer simulation of growth and coarsening of Laves phase in a modified 12 % chromium steel*”. Scandinavian Journal of Metallurgy, vol. 32, no. 2. 2003. pp. 94-99.
- [21] K. Easterling. “*Introduction to the physical metallurgy of welding*”. Butterworth-Heinemann. London. 1992.

- [22] C.J. van Niekerk, M. du Toit and M. W. Erwee. “*Sensitisation of AISI 409 ferritic stainless steel during low heat input arc welding*”. *Welding in the World*, vol. 56, no. 5. 2012. pp. 54-64.
- [23] N.J.E. Dowling, H. Kim, J-N. Kim, S-K. Ahn and Y-D. Lee. “*Corrosion and toughness of experimental and commercial super ferritic stainless steels*”. *Corrosion*, vol. 55, no. 8. 1999. pp. 743-755.
- [24] D.H. Kah and D.W. Dickenson. “*Weldability of ferritic stainless steels*”. *Welding Journal*, vol. 60 , no. 8. 1981. pp. 135s-142s.
- [25] J.K. Kim, Y.H. Kim, J.S. Lee and K.Y. Kim. “*Effect of chromium content on intergranular corrosion and precipitation of Ti-stabilized ferritic stainless steels*”. *Corrosion Science*, vol. 52, no. 5. 2010. pp. 1847-1852.
- [26] J.K. Kim, Y.H. Kim, S.H. Uhm, J.S. Lee and K.Y. Kim. “*Intergranular corrosion of Ti-stabilized 11wt% Cr ferritic stainless steel for automotive exhaust systems*”. *Corrosion Science*, vol. 51, no. 11. 2009. pp. 2716-2723.
- [27] M. du Toit, G.T. van Rooyen and D. Smith. “*Heat-affected zone sensitization and stress corrosion cracking in 12% chromium type 1.4003 ferritic stainless steels*”. *Corrosion*, vol. 63, no. 5.2007. pp. 395-404.
- [28] M.L. Greeff and M. du Toit. “*Looking at the sensitisation of 11-12 % chromium EN 1.4003 stainless steel*”. *Welding Journal*, vol. 85, no. 11. 2006. pp. 243-251.
- [29] M. du Toit and J. Naudé. “*The influence of stabilisation with titanium on the heat-affected zone sensitisation of 11 to 12% chromium ferritic stainless steels under low heat input welding conditions.*” *Welding in the World*, vol. 55, no. 3/4. 2011. pp. 38-47.
- [30] C.J. van Niekerk and M. du Toit. “*Sensitisation behaviour of 11-12% Cr AISI 409 stainless steel low heat input welding*”. *Journal of the Southern African Institute of Mining and Metallurgy*, vol. 111, no. 4. 2011. pp. 243-256.
- [31] K.H. Lo, C.H. Shek and J.K.L. Lai. “*Recent developments in stainless steels*”. *Material Science and Engineering R*, vol. 65. 2009. pp. 39-104.
- [32] A. Redjaimia, G. Metauer and M. Gantois. “*Decomposition of delta ferrite in a Fe-22Cr-8Ni-3Mo-0.03C duplex stainless steels. A morphological and structural study*”. *Duplex Stainless steels*, vol. 91. 1991. pp. 119-126

- [33] T.H. Chen and J.R. Yang. "Effect of solution treatment and continuous cooling on σ phase precipitation in a 2205 duplex stainless steel". *Material Science and Engineering A*, vol. 427. 2001. pp. 28-41.
- [34] D.N. Wasnik, G.K. Dey, V. Kain and I. Samaidar. "Precipitation stage in a 316L austenitic stainless steel". *Scripta Materialia*, vol. 49. 2003. pp. 135-141.
- [35] E.A. Trillo and L.E. Murr. "A TEM Investigation of $M_{23}C_6$ carbide precipitation behaviour on varying grain boundary misorientation in 304 stainless steels". *Journal of materials science*, vol. 33. 1999. pp. 1263-1271.

CHAPTER 3: PROCESSES FOR WELDING FERRITIC STAINLESS STEEL

Gas Tungsten Arc Welding (GTAW) and Laser Beam Welding (LBW) were selected to weld type 441 ferritic stainless steel during the course of this investigation. This chapter considers the reasons for choosing these processes in addition to discussing the advantages, operating principles and consumables used for each process.

3.1 GAS TUNGSTEN ARC WELDING (GTAW)

Gas tungsten arc welding (GTAW), illustrated schematically in Figure 3.1, is an arc welding process in which the heat for welding is supplied by an arc that forms between the workpiece and a non-consumable tungsten electrode. The electrode, weld pool, arc and adjacent base metal are protected from atmospheric contamination by an inert gas shield supplied through the torch. This process can be used in a manual, mechanised or fully automated configuration [1,2].

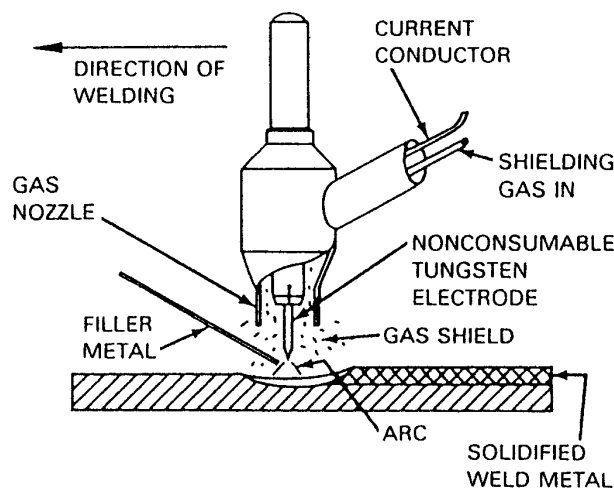


Figure 3.1: GTAW welding process [1].

An important advantage of this process is that autogenous welding (welding without filler) is possible since the electrode is not consumed during welding. In addition, the arc and weld pool are visible during welding, making it easier for the welder to control the welding process. If filler metal is used, it is fed directly into the weld pool and not transferred across the arc. All positional welding is possible and very thin sheet can be joined by using a pulsed power supply to reduce the average heat input [1,2].

One of the main differences between GTAW and other arc welding processes is that a non-consumable welding electrode is used. Tungsten is the electrode material of choice as it has the highest melting point (3410°C) of all metals and is an excellent emitter of electrons. Tungsten electrodes are readily available in different diameters and lengths and are classified in accordance with the requirements in AWS A5.12 [3]. Thoriated or ceriated tungsten electrodes are widely preferred for welding stainless steels. Thoriated electrodes are alloyed with 1 or 2 wt% ThO₂, improving electron emissivity while hot, increasing current carrying capacity, extending electrode life and ensuring greater resistance to contamination. Due to the health risks associated with low level radioactive emissions resulting from the ThO₂ additions, ceriated tungsten electrodes, alloyed with 2 wt% CeO₂, are now recommended in most applications involving stainless steel welding [1,2].

GTAW of ferritic stainless steel requires the use of an inert shielding gas to protect the weld pool, tungsten electrode and the heated end of the filler rod (if used) from atmospheric contamination. Argon, helium and argon-helium mixtures can be used for welding stainless steels, but pure argon is preferred in most manual and semi-automatic applications as it is less expensive than helium. Argon provides a soft, smooth and stable arc with excellent arc starting characteristics.

The GTAW process can be performed using direct current with electrode negative polarity (DCEN), direct current with electrode positive polarity (DCEP), pulsed direct current and alternating current (AC). DCEN is most widely used for welding stainless steel as most of the heat generated is used to melt the metal (less heat is lost through electrode heating). This results in warm arcs and deep penetration.

3.2 LASER BEAM WELDING (LBW)

Laser beam welding is a non-arc welding process that uses a high energy, coherent beam of light of a fixed wavelength to melt and fuse the metal. Such a high intensity beam is produced by stimulating radiation in a suitable gaseous or solid lasing medium. Welding is performed by focusing the radiation to a small spot size (usually less than 0.5 mm in diameter) on the workpiece. This high energy beam melts and vaporises the metal, enabling the metals to be joined [1,4].

Laser beam welding has a number of advantages over arc welding processes. Due to the high energy density in the beam, deep penetration is possible at low heat input levels. The welds and heat-affected zones tend to be narrow and distortion is minimised. High welding speeds are possible and filler metal is not required for most joints and edge preparations [4].

Laser welding requires a precisely focused, coherent laser beam. When focused to the appropriate spot size, the beam melts the metal, rapidly producing a narrow weld with high joint efficiency and minimal distortion. A laser typically consists of three fundamentally distinct parts: (1) a laser material or medium, (2) a method of excitation and (3) a resonant cavity. If white light is radiated into a gas enclosed in a vessel, many gas atoms may be raised, through resonance, from the ground state to excited states. As the electrons drop back, many of the atoms may be trapped in metastable energy levels. If the light intensity is high enough, a population inversion may be obtained, i.e. more atoms in the metastable state than in the ground state [5].

When an electron in one of these metastable states spontaneously jumps to the ground state, a photon of energy is emitted. As the photon passes another atom in the same metastable state, it can stimulate that atom to radiate a photon of the same frequency. The photon has exactly the same frequency, direction, phase, speed and polarisation as the primary photon. If the conditions in the gas are right, a chain reaction can be produced, resulting in high-intensity coherent radiation [1,5].

In order to produce a laser the stimulated radiation must be collimated by designing a resonant cavity in which the waves can be used repetitively. If two highly reflecting mirrors are placed at the ends of a cylindrical vessel and the atoms are excited to produce a population inversion, photons emitted parallel to the axis of the cylinder will be reflected back and forth. Photons moving at an appreciable angle to the walls of the vessel escape and are lost. If the mirrors are highly reflective and a high population density of metastable atoms exists in the vessel, the build up of photons surging back and forth through the cavity can be self-sustaining and the system oscillates, or lases, spontaneously [1,5]. The resulting laser is monochromatic (all of the output of the laser is concentrated in a single wavelength), highly directional and collimated (its angular spread is very small), and coherent (the amplitudes of the

waves are superimposed, resulting in constructive interference and a very intense beam) [5].

One of the most efficient lasers currently available for materials processing applications is the CO₂ laser, which can be utilised in both the high power continuous wave and pulsed operating modes. CO₂ lasers use an electric discharge as the source for exciting the lasing medium, which is CO₂ gas. The gas mixture for the laser is usually a combination of helium, nitrogen and CO₂ [5].

The simplest CO₂ laser has an axial flow system, i.e. the gas flows in the same direction as the laser beam and the electric field. The axial flow of gas is maintained to replenish molecules depleted by the effects of the discharge of electricity used for excitation. A mirror is located at each end of the discharge tube to complete the resonator cavity. Typically, one mirror is totally reflective and the other is partially transmissive and partially reflective [1,5].

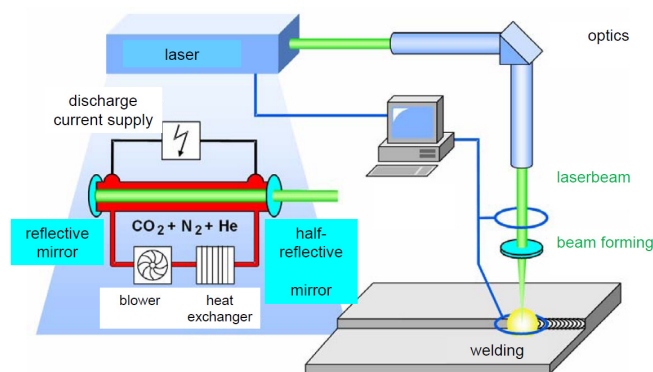


Figure 3.2: Schematic illustration of CO₂ laser welding [6].

Laser welds can be made at a variety of laser powers, depending upon whether a conduction-limited or deep-penetration weld is desired. A considerable amount of laser welding is performed in the conduction-limited mode on thin sheet. A conduction-limited weld is one where the laser melts the joint materials without significant vapourisation. The delivery of the laser power may be continuous or pulsed. Conduction-limited welds are usually limited to sheet thicknesses of less than 2 mm [1,5].

Laser beam welding with a high power continuous wave CO₂ laser is most effective in the deep-penetration or keyhole mode, in which the laser melts a small cylindrical

volume of metal through the thickness of the material. A column of vapour is produced in this hole, surrounded by a liquid pool. As the laser traverses the workpiece and the column is moved along the joint, the material on the advancing side of the hole is melted throughout its depth. The molten metal flows along the base of the hole and solidifies along the rear of the pool [5].

Because the laser beam vapourises and melts the material in the fusion zone, this area needs to be protected from the atmosphere. LBW normally uses an inert gas shield, typically argon or helium. Helium is inert and has a high ionisation potential, making it more resistant to plasma formation. For welding with a pulsed laser or moderate power continuous wave laser, the shielding gas feeds to the weld along the laser beam axis. Production welding with a high power CO₂ laser requires a shielding fixture that completely covers the weld. Single-pulse, solid-state laser welding is possible without shielding gas, because the weld pool is molten for only a very short time [5].

3.3 MOTIVATION FOR USING GTAW AND LBW

As described in Chapter 2, the reduction in toughness in the weld and heat-affected zone (HAZ) due to excessive ferrite grain growth remains the greatest concern during the welding of ferritic stainless steels. Ferritic stainless steels therefore have to be welded using processes capable of restricting grain growth in the HAZ and fusion zone by minimising heat input, but without adversely affecting fusion. Since filler metal is not transferred across the arc, GTAW has the advantage over other arc welding processes that low heat input welding is possible. If required, heat input can be further reduced by means of a pulsed power supply [7]. Since heat input can be controlled to within narrow tolerances and autogeneous welding is possible, GTAW remains a popular process for welding ferritic stainless steels in thin sections.

The low heat inputs and deep penetration that can be achieved with laser welding makes it an equally attractive process for joining ferritic stainless steels. The welds and heat-affected zones are narrow, and distortion is reduced. High welding speeds can be used and the process is well adapted to welding thin sections (using conduction-limited welding) and thick sections (using keyhole welding) [8].

3.4 REFERENCES

- [1] American Welding Society. *"AWS Welding Handbook -Volume 2: Welding Processes"*. American Welding Society, Miami, FL. 1991.
- [2] The Lincoln Electric Company. *"The Procedure Handbook of Arc Welding"*, 13th edition. The Lincoln Electric Company, Cleveland, OH. 1994.
- [3] AWS A5.12M/A5.12:2009. *"Specification for tungsten and oxide dispersed tungsten electrodes for arc welding and cutting"*. American Welding Society, Miami, FL. 2009.
- [4] J. Norrish. *"Advanced Welding Processes"*. Woodhead Publishing, Cambridge. 2006. pp. 95-129.
- [5] ASM International. *"ASM Handbook - Volume 6: Welding, Brazing and Soldering"*. ASM International, Materials Park, OH. 1993.
- [6] M. Rethmeier. *"Laserbeam welding"*. Unpublished presentation to the International Welding Engineer class, University of Pretoria. 2013.
- [7] J.A. Hamill, F.R. Manley and D.E Nelson. *"Fusion welding P/M components for automotive applications"*. Proceedings of the SAE International Congress and Exposition, held in Dearborn, MI, on 1-5 March 1993.
- [8] M. Tullmin, F.P.A. Robinson, C.A.O. Henning, A. Strauss and J. le Grange. *"Properties of laser-welded and electron-beam-welded ferritic stainless steel"*. Journal of the Southern African Institute of Mining and Metallurgy, vol. 89, no. 8. August 1989. pp. 243-249.

CHAPTER 4: EXPERIMENTAL PROCEDURE

This chapter provide detailed overview of the experimental procedure and workplan followed in order to characterise the microstructure and properties of autogenous type 441 welds during the course of this investigation.

4.1 ALLOY INVESTIGATED

The parent material used in this investigation was supplied by Columbus Stainless in the form of commercial type 441 stainless steel plate from a single production batch. The melt chemistry of the steel supplied is shown in Table 4.1 below, and conforms in specification to EN 1.4509 (in accordance with BS EN 10088-2:2005 [1]) and UNS S44100 (as specified in ASTM A240/A240M-14 [2]). The material was supplied in the fully annealed condition in the form of 5 mm thick plate.

Table 4.1. *Nominal chemical composition of the type 441 stainless plate material used in this investigation (weight percentage, balance Fe).*

C	Si	Mn	P	S	N	Cr	Nb	Ni	Ti	Co	V
0.015	0.50	0.51	0.040	0.015	0.0085	17.89	0.444	0.19	0.153	0.03	0.12

The steel chemistry in Table 3.1 confirms that the steel is overstabilised with respect to sensitisation, with a stabilisation ratio of 25 (calculated according to equation (4.1)).

$$\text{Stabilisation ratio} = \frac{(\text{Ti} + \text{Nb})}{(\text{C} + \text{N})} \quad \dots(4.1)$$

4.2 THERMODYNAMIC MODELLING

In order to understand the phase transformations and precipitation reactions that can occur in type 441 stainless steel with the composition shown in Table 4.1, Thermo-Calc™ was used to predict the equilibrium phase transformations that occur during cooling from the liquid state in this steel. This software package performs phase diagram calculations by minimising the total Gibbs free energy of the components specified and is designed to handle complex problems involving interactions between various elements and phases. Due to the non-equilibrium nature of the

heating and cooling cycles experienced during welding, these results cannot be used to explain microstructure evolution during welding. It gives an indication, however, of the phases that are stable at various temperatures, purely on the basis of thermodynamic considerations.

4.3 WELDING

4.3.1 Gas Tungsten Arc Welding (GTAW)

In order to study microstructure evolution during arc welding, bead-on-plate welds were deposited on cleaned and degreased 441 plate samples using autogenous gas tungsten arc welding (GTAW) at different heat inputs (yielding a range of cooling rates after welding). As a consequence, the penetration of the welds varied with increasing heat input. A non-consumable thoriated tungsten electrode (classified as EWTh-2 according to AWS A5.12 [3]) was used with pure welding-grade argon as shielding gas. DCEN (direct current electrode negative) polarity was used with a constant arc length of 2 mm for all welds. A uniform travel speed of 2 mm/s was maintained, controlled by keeping the arc and welding torch stationary and moving the workpiece at a constant rate using a custom built tractor and stepper motor. The experimental setup used for GTAW is shown in Figure 4.1. The heat input during welding was varied between 0.09 kJ/mm and 0.80 kJ/mm by controlling the welding current. The welding current was not pulsed. The heat input, HI , was calculated from the welding parameters using equation (4.2), where η represents the arc efficiency of the process, V the arc voltage, I the welding current and v the travel speed.

$$HI = \frac{\eta VI}{v} \quad \dots(4.2)$$

Previous research showed that the arc efficiency for the power source and experimental setup used during this investigation is approximately 49% [4], which is consistent with gas tungsten arc welding using electrode negative polarity.

The ASME Boiler and Pressure Vessel Code, Section IX: Welding and Brazing Qualification [5] lists the essential variables that need to be considered when qualifying a GTAW welding procedure. These are listed below in table 4.2.

Table 4.2: List of essential welding variables used in this study for GTAW welding as required by ASME IX [5].

ASME IX Paragraph		Process Variable	Value
QW-403 Base Material	.8	Base Metal thickness	5 mm Plate
	.11	P number	AISI 441 P No.7
QW-405 Positions	.2	Positions	Flat
QW-408 Gas	.2	Single, mixture, or %	Single, Argon Welding Grade
QW-409 Electrical Characteristics	.1	Heat Input	0.15-0.80 kJ/mm
	.4	Current or Polarity	40-202 A DCEN Polarity

Note: No Filler Material, Preheat, or Post Weld Heat Treatment used.

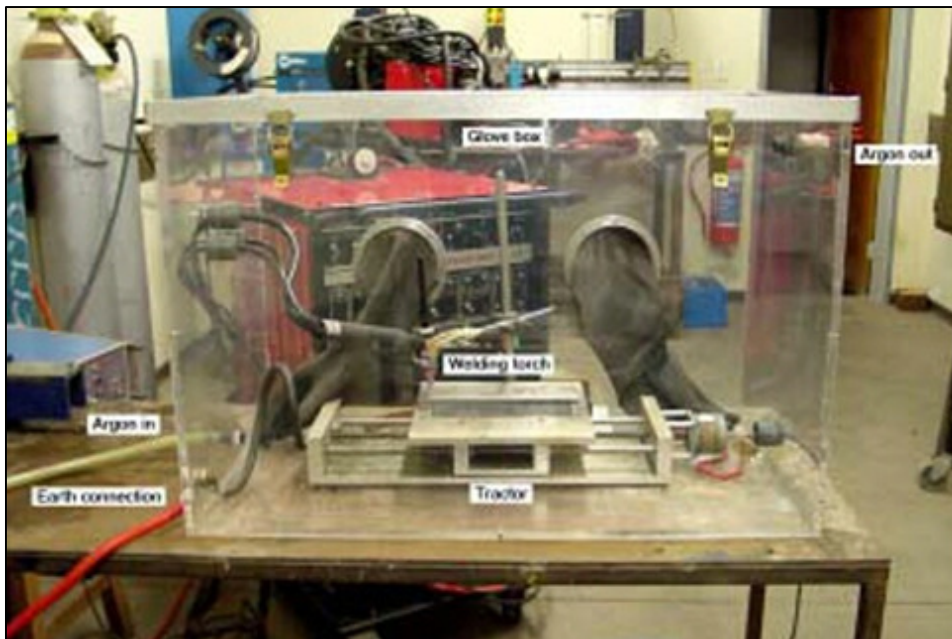


Figure 4.1. The GTAW experimental setup (photograph courtesy of Prof M. du Toit).

4.3.2 Laser Beam Welding (LBW)

Laser welding of type 441 samples was performed by BAM (Federal Institute for Materials Research and Testing) in Berlin, Germany, using a continuous-wave CO₂ laser with helium as shielding gas. The laser power was varied between 3.5 kW and 5.7 kW and the welding speed between 1.5 m/min and 2.0 m/min to produce heat

inputs of 0.11 kJ/mm and 0.23 kJ/mm. The list of essential variables that need to be considered when qualifying a laser welding procedure in accordance with ASME IX is shown in Table 4.3.

Table 4.3. List of essential welding variables used in this study for LBW welding as required by ASME IX [5].

ASME IX Paragraph		Process Variable	Value
QW-403 Base Material	.1	P number	AISI 441, P No.7
	.3	Penetration	Full penetration over 5 mm thickness plate
QW-408 Gas	.2	Single, mixture, or %	Helium Welding Grade
	.12	Gas Flow Rate	Not Recorded
QW-409 Electrical Characteristics	.19	Pulse	Not Applicable
	.20	Mode, energy	Continuous Mode
	.21	Power	3.5 kW and 5.7 kW
QW-410 Technique	.7	Oscillation	Not recorded
	.14	Angle of beam axis	Not recorded
	.20	Wash Pass	Not Used
	.21	1 vs 2 side welding	Single side welding
	.37	Single to multiple pass	Single pass welding
	.64	Use of thermal process	Not used
	.66	Travel, Beam factors	1.5-2 m/min
	.67	Optical Technique	Not recorded
	.68	Type of equipment	Continuous wave CO ₂ laser
	.77	Wavelength	Not Recorded
.80	Spot Size	Not Recorded	
Note: No Filler Material, Preheat, or Post Weld Heat Treatment used.			

4.4 METALLOGRAPHIC EXAMINATION

In order to examine the microstructures of the parent material, weld metal and heat-affected zones of the type 441 samples, a combination of optical microscopy, scanning electron microscopy (SEM) and transmission electron microscopy (TEM) techniques was used.

Representative samples were sectioned from the parent material and welded plates and mounted in resin before being ground and diamond polished to a 1 μ m finish. To reveal the general microstructure, the polished samples were etched electrolytically in a 55% nitric acid solution at a potential of 1.5 V DC for between 30 and 120 seconds.

The metallographic samples were examined using an Olympus PGM™ optical microscope, equipped with Olympus Stream™ image analysis software, a JEOL JSM-6300 scanning electron microscope (SEM) and a high resolution field emission JEOL JSM-6000F SEM. The grain size in the heat-affected zone was determined using the Heyn linear intercept method described in ASTM E112-13 [6]. Transmission electron microscopy was performed by Mr Stan Mandziej from Dynamic Systems Inc. in the Netherlands.

4.5 PHASE IDENTIFICATION

Two analytical techniques were used to identify the phases within the microstructures, namely energy dispersive X-ray spectrometry (EDS) and X-ray diffraction (XRD).

The EDS technique uses the characteristic X-ray spectrum emitted when a high-energy beam of electrons is focused on the solid sample to obtain a localised chemical analysis. Quantification involves comparing line intensities for each element observed with calibration standards of known composition. During the course of this project EDS analysis was used in conjunction with SEM investigation of the microstructure. Samples were gold coated for improved conductivity during high resolution SEM analysis.

XRD was used to identify second phase particles in the weld metal and HAZ. Due to the narrow width of the weld metal and HAZ relative to the parent material, an electrolytic extraction technique was used to dissolve the matrix while retaining the precipitates and second phase particles in the weld metal and HAZ. Samples were sectioned in such a way that the weld metal and the HAZ were retained, but the amount of surrounding parent material minimised. To obtain solid residue for analysis, an electrochemical cell was created in such a way that the weld sample was the anode. As shown in Figure 4.2, a stainless steel container was employed as

cathode and a 60% nitric acid solution as electrolyte. A voltage of 5 VDC (direct current) was applied to promote dissolution of the anode. The ferrite matrix dissolved, leaving the second phase particles in the matrix as a fine solid residue that was recovered through vacuum filtration using sub-micron filter paper ($<0.7\mu\text{m}$). The extracted residue was rinsed in ethanol and dried at 200°C . The dried residue was finally milled to a fine powder and subjected to XRD analysis.



Figure 4.2. Experimental setup for electrolytic extraction of second phase particles and precipitates for XRD analysis.

4.6 SENSITISATION TESTING

Sensitisation was evaluated using the 10% oxalic acid electrolytic etch described in Practice W of ASTM 763-93 [7]. In order to classify the resulting microstructures, polished and etched samples of each weld were examined using an optical microscope. The oxalic acid etch reveals the presence and location of any chromium-rich carbides in the microstructure, but normally only serves as a screening test for sensitisation as it cannot discern between sensitised and healed (or desensitised) structures. Although previous work [8-10] confirmed that the oxalic acid etch serves as a reliable test for determining the susceptibility of ferritic stainless steels to sensitisation after low heat input welding, the $\text{Cu-CuSO}_4\text{-H}_2\text{SO}_4$

test, described in Practice Z of ASTM 763-93, was used to confirm chromium depletion associated with the presence of grain boundary Cr-rich carbides. Since the narrow width of the high temperature heat-affected zone did not facilitate the use of bending to locate any chromium depleted zones after testing, the samples were analysed using a scanning electron microscope. Ditching of grain boundaries and grain dropping were seen to be indicative of sensitisation in samples tested according to Practice Z.

4.7 DILATOMETRY

A dilatometer measures the dimensional changes of a specimen with variation in temperature, and is commonly used for determining phase transformation temperatures and for constructing phase diagrams. During the course of this investigation, a Bähr-Thermanalyse DIL805 A/D deformation dilatometer was used to determine whether any phase transformations occurred in the 441 parent material during cooling. Small cylindrical test samples were heated from room temperature to 1300°C at a constant rate of 153°C/s, and cooled at the same rate to room temperature. The heating and cooling rates obtained during welding are higher than 153°C/s, but 153°C/s was the highest possible using the dilatometer. The change in length as a function of temperature was recorded continually during the heat treatment.

4.8 MECHANICAL TESTING

During the course of this investigation, a series of mechanical tests were performed to determine the hardness, transverse tensile strength and toughness of the base metal and welded samples.

4.8.1 Hardness measurements

Hardness measurements were performed across the welds to compare the hardness of the weld metal, HAZ and surrounding base metal. A calibrated micro-Vickers hardness tester with an applied load of 300g was used and testing was performed in accordance with the requirements of ASTM E384-11e1 [11]. At least three measurements were taken to obtain a statistically relevant average for each location.

4.8.2 Tensile tests

Transverse tensile tests were performed on gas tungsten arc welds for three different heat input levels, namely 0.20 kJ/mm, 0.45 kJ/mm and 0.80 kJ/mm, and on laser welds for heat input levels of 0.11 kJ/mm and 0.23 kJ/mm. The tensile tests were performed at a cross head speed of 5 mm/min at room temperature using sub-size specimens prepared in accordance with the recommendations of ASTM E8/E8M-11 [12]. The dimensions of the samples used are shown in Figure 3.3 and Table 3.2. At least three tests were performed for each heat input level.

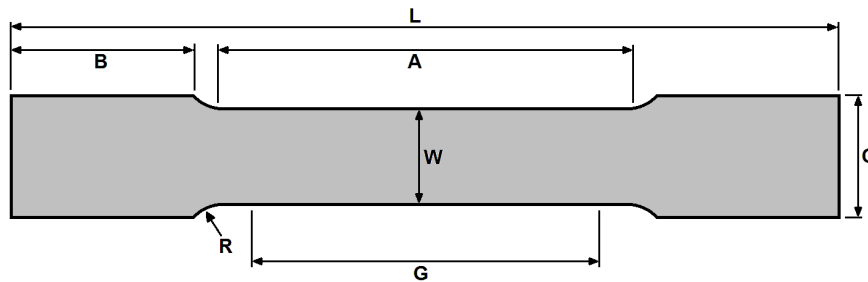


Figure 4.3. The dimensions of the transverse tensile samples used.

Table 4.4. The dimensions of sub-size transverse tensile specimens.

<i>Parameter</i>	<i>Dimension</i>
G – Gauge length	25.0 ± 0.1 mm
W – Sample width	6.0 ± 0.1 mm
T – Sample thickness	5 mm
R – Radius of fillet	6 mm
L – Overall length	100 mm
A – Length of reduced section	32 mm
B – Length of grip section	30 mm
C – Width of grip section	10 mm

4.8.3 Sub-size Charpy V-notch impact tests

In order to test the impact toughness of the welds, miniaturised Charpy V-notch impact samples were prepared as the plate thickness of the 441 base material did not allow the use of full-size specimens. Figure 4.4 below shows the dimensions of the miniaturised Charpy V- notch samples, as prescribed by ASTM E2248-13 [13].

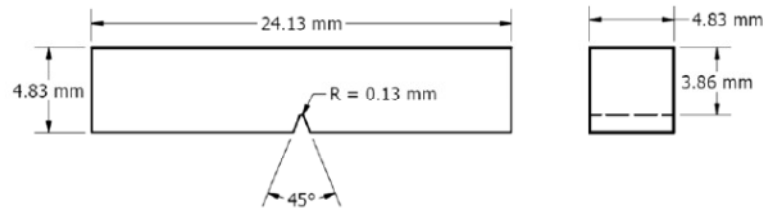


Figure 4.4. The dimensions of the miniaturised Charpy V-notch samples used in this investigation (in accordance with ASTM E2248-13).

Impact tests were carried out on the gas tungsten arc welds for three different heat input levels, namely 0.20 kJ/mm, 0.45 kJ/mm and 0.80 kJ/mm, and on laser welds at heat inputs of 0.11 kJ/mm and 0.23 kJ/mm. The notch was located in the weld metal or HAZ and the tests were repeated a minimum of three times for each heat input and notch placement area.

The results of these experiments are discussed in more detail in Chapter 5.

4.9 REFERENCES

- [1] ASTM A240/A240M-14. "Standard Specification for Chromium and Chromium-Nickel Stainless Steel Plate, Sheet, and Strip for Pressure Vessels and for General Applications". ASTM International, West Conshohocken, PA. 2014.
- [2] BS EN 10088-2:2005. "Stainless steels. Technical delivery conditions for sheet/plate and strip of corrosion resisting steels for general purposes". The British Standards Institution, London. 2005.
- [3] AWS A5.12M/A5.12:2009. "Specification for tungsten and oxide dispersed tungsten electrodes for arc welding and cutting". American Welding Society, Miami, FL. 2009.
- [4] M. du Toit and P.C. Pistorius. "Nitrogen control during the autogenous arc welding of stainless steel - Part 1: Experimental observations". Welding Journal, vol. 82, no. 8. August 2003. pp. 219s-224s.
- [5] ASME IX Boiler and Pressure Vessel Code. "Welding and brazing qualifications". ASME International, New York, NY. 2015.
- [6] ASTM E112-13. "Standard test methods for determining average grain size". ASTM International, West Conshohocken, PA. 2013.
- [7] ASTM A763-93. "Standard practices for detecting susceptibility to intergranular

- attack in ferritic stainless steels*". ASTM International, West Conshohocken, PA. 2009.
- [8] M.L. Greeff and M. du Toit. "*Sensitisation of two 11-12% chromium type EN 1.4003 ferritic stainless steels during continuous cooling after welding*". *Welding in the World*, vol. 50, no. 7/8. 2006. pp. 18-27.
- [9] M. du Toit and J. Naudé. "*The influence of stabilisation with titanium on the heat-affected zone sensitisation of 11 to 12% chromium ferritic stainless steels under low heat input welding conditions*". *Welding in the World*, vol. 55, no. 3/4. 2011. pp. 38-47.
- [10] C.J. van Niekerk and M. du Toit. "*Sensitisation behaviour of 11-12% Cr AISI 409 stainless steel low heat input welding*". *Journal of the Southern African Institute of Mining and Metallurgy*, vol. 111, no. 4. April 2011. pp. 243-256.
- [11] ASTM E384-11e1. "*Standard test method for Knoop and Vickers hardness of materials*". ASTM International, West Conshohocken, PA. 2011.
- [12] ASTM E8/E8M-11. "*Standard test methods for tension testing of metallic materials*". ASTM International, West Conshohocken, PA. 2011.
- [13] ASTM E2248-13. "*Standard test method for impact testing of miniaturized Charpy V-notch specimens*". ASTM International, West Conshohocken, PA. 2013.

CHAPTER 5: RESULTS AND DISCUSSION

In this chapter, the results obtained from the experimental work, described in Chapter 4, are considered. The microstructures observed in the weld metal, heat-affected zone and base material of autogenous type 441 gas tungsten arc welds and laser welds are interpreted, and an attempt made to relate the observed microstructures to the measured mechanical properties of the welded joints.

5.1 MICROSTRUCTURE PREDICTIONS FOR TYPE 441 STAINLESS STEEL

In order to understand the phase transformations and precipitation reactions that can occur in type 441 stainless steel with composition shown in Table 4.1, ThermoCalc™ was used to predict the equilibrium phase transformations that occur during cooling from the liquid state in this steel. Due to the non-equilibrium nature of the heating and cooling cycles experienced during welding, these predictions cannot be used to explain microstructure evolution during welding, but can give an indication of the phases that are thermodynamically stable in the alloy on cooling.

Figure 5.1(a) shows the predicted amounts of liquid, body centred cubic (BCC) ferrite and sigma (σ) phase in type 441 as a function of temperature, while Figure 5.1(b) shows the predicted carbonitride and Laves phase fractions on an enlarged scale. The thermodynamic predictions shown in Figure 5.1(a) confirm that the alloy under investigation solidifies as primary ferrite, with the BCC ferrite phase remaining stable down to room temperature. During cooling, small amounts of a number of other phases are also predicted to form. As shown in Figure 5.1(b), titanium-rich carbonitrides are very stable under equilibrium conditions over the entire temperature range after solidification. In addition to titanium, these carbonitrides are predicted to contain niobium in solid solution. A small amount of Laves phase is predicted to form at temperatures below approximately 950°C, with significant amounts of sigma phase precipitating at temperatures below about 650°C under equilibrium conditions. In accordance with these predictions, the base material in the as-supplied condition (fully annealed) should consist of a single-phase ferrite matrix and titanium-rich carbonitride precipitates (with some niobium in solution).

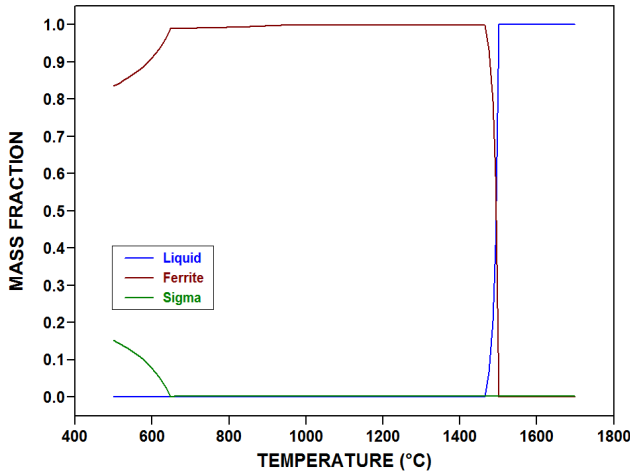


Figure 5.1(a): Predicted by Thermo-Calc™ mass fractions of the liquid, ferrite and sigma phases in type 441 stainless steel as a function of temperature.

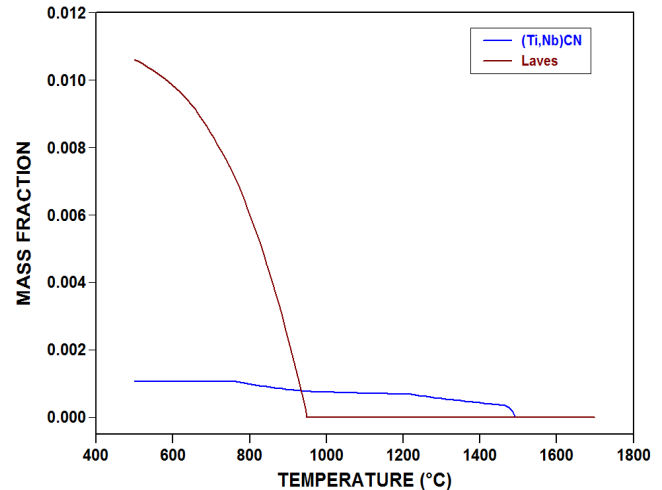


Figure 5.1(b): Predicted by Thermo-Calc™ mass fractions of (Ti,Nb)CN and Laves phases in type 441 stainless steel as a function of temperature.

It is important to note that Thermo-Calc™ does not predict the presence of the chromium-rich $M_{23}C_6$ carbide that is generally assumed to be responsible for the majority of sensitisation and intergranular corrosion observed in stainless steels. This can be attributed to the fact that Thermo-Calc™ assumes that under equilibrium slow cooling conditions, all carbon and nitrogen are combined with niobium and titanium in the form of carbides and carbonitrides. The earlier observation that the steel is overstabilised (with a stabilisation ratio of 25) suggests that there is sufficient titanium and niobium to remove all carbon and nitrogen from solid solution during cooling prior to the onset of $M_{23}C_6$ precipitation at lower temperatures.

The Balmforth diagram [1] can be used to predict the weld metal microstructures of ferritic and ferritic-martensitic stainless steels as a function of chemical composition. As shown in Figure 5.2, autogenous welds in type 441 ferritic stainless steel with the chemical composition shown in Table 4.1 are predicted to be fully ferritic, with no austenite or martensite present at room temperature. This diagram, however, does not consider the precipitation of carbides, carbonitrides or intermetallic phases on cooling.

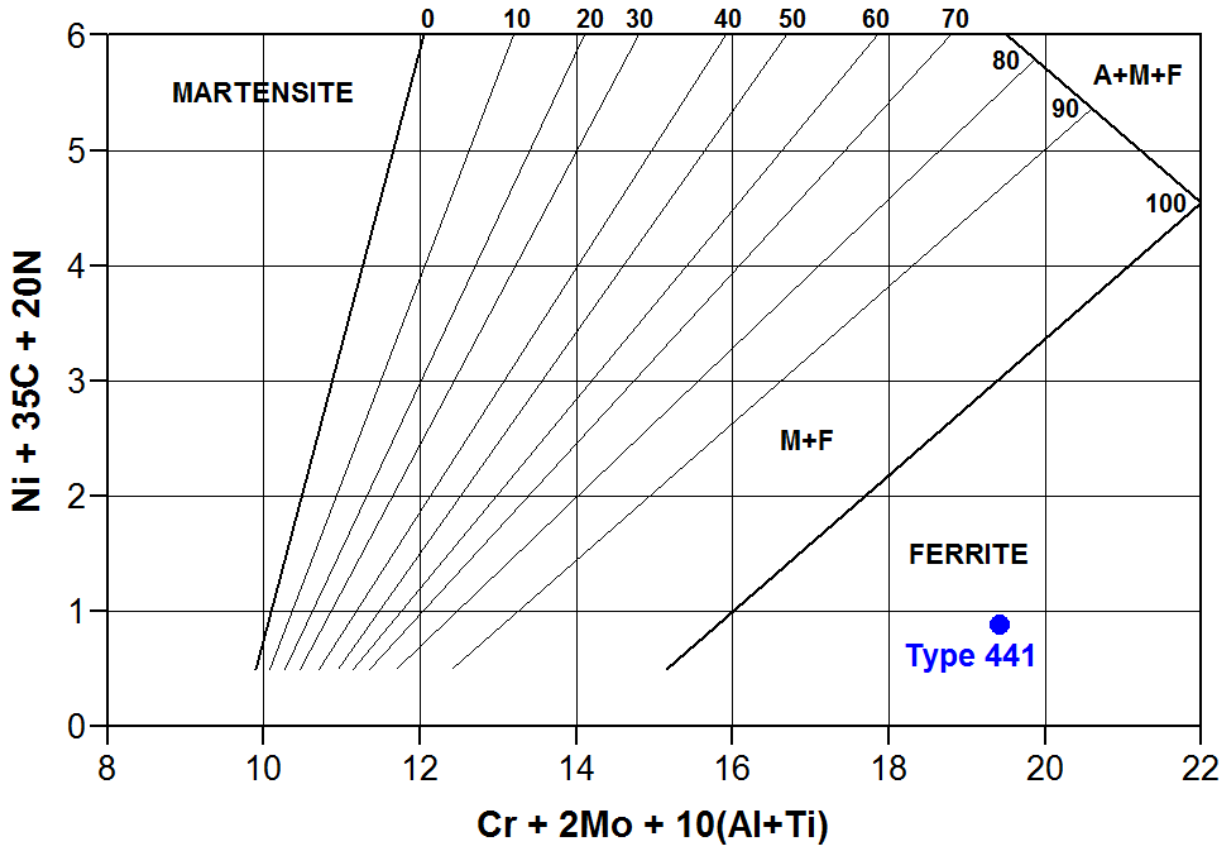


Figure 5.2: Balmforth diagram for predicting the microstructure of martensitic and martensitic-ferritic stainless steel welds [1]. The composition of the type 441 used in this investigation is shown on the diagram.

5.2 MICROSTRUCTURES OF THE GAS TUNGSTEN ARC WELDS

Figure 5.3 displays representative optical photomicrographs of the weld metal, surrounding heat-affected zone and base metal of welds performed at a very low heat input (0.09 kJ/mm), an intermediate heat input (0.3 kJ/mm) and a high heat input (0.7 kJ/mm) in the range studied. The microstructure of the weld performed at 0.09 kJ/mm, shown in Figure 5.3(a), confirms that the HAZ is predominantly ferritic. The high temperature heat-affected zone (HTHAZ) adjacent to the fusion line is characterised by a ferrite grain size that is marginally coarser than that of the base metal (average HTHAZ grain diameter of $35 \pm 5 \mu\text{m}$, compared to an average base metal grain size of $32 \pm 3 \mu\text{m}$). This region of the heat-affected zone experienced the highest temperatures during the weld thermal cycle, but the cooling time at this low heat input was too fast to allow extensive grain growth. The low temperature heat-affected zone (LTHAZ) appears to have a finer grain size than that of the base metal.

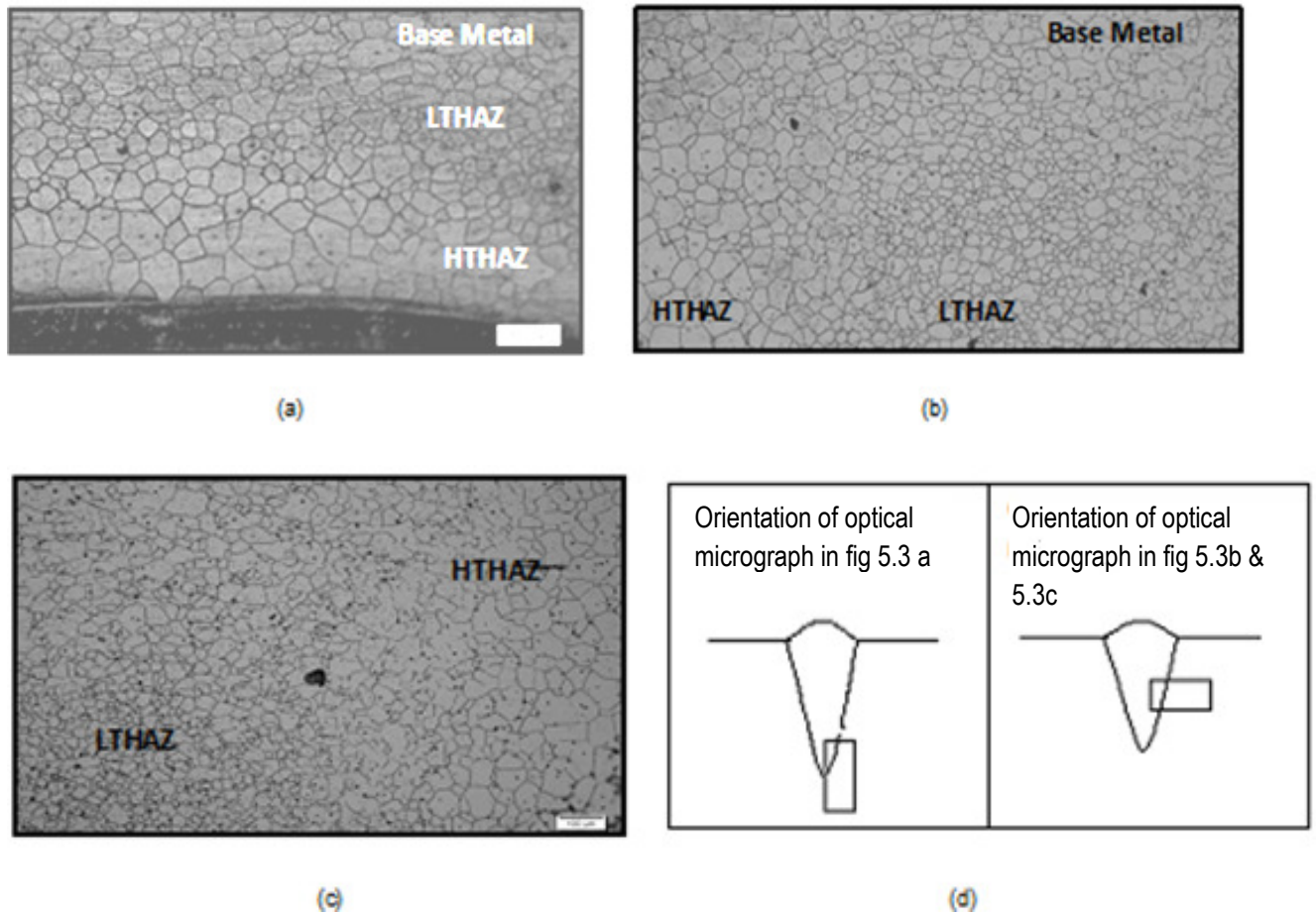


Figure 5.3: Microstructure of the heat-affected zone of gas tungsten arc welds in type 441 ferritic stainless steel at effective heat input levels of: (a) 0.09 kJ/mm; (b) 0.3 kJ/mm; (c) 0.7 kJ/mm (electrolytic HNO_3 etch); and (d) orientations of micrographs in a-c.

The same trend is evident in micrographs of welds performed at 0.3 and 0.7 kJ/mm, as shown in Figures 5.3(b) and (c), respectively. The coarse grained HTHAZ adjacent to the fusion line displays the largest grain size (with an average grain diameter of $76 \pm 7 \mu\text{m}$ after welding at 0.3 kJ/mm and $131 \pm 8 \mu\text{m}$ after welding at 0.7 kJ/mm). An increase in heat input results in a slower cooling rate after welding, with a correspondingly longer residence time above the grain coarsening temperature. The LTHAZ further removed from the weld fusion line displays evidence of considerable grain refining (with average grain sizes between 18 and 22 μm).

The same trend is evident in micrographs of welds performed at 0.3 and 0.7 kJ/mm, as shown in Figures 5.3(b) and (c), respectively. The coarse grained HTHAZ adjacent to the fusion line displays the largest grain size (with an average grain diameter of $76 \pm 7 \mu\text{m}$ after welding at 0.3 kJ/mm and $131 \pm 25 \mu\text{m}$ after welding at 0.7

kJ/mm). An increase in heat input results in a slower cooling rate after welding, with a correspondingly longer residence time above the grain coarsening temperature. The LTHAZ further removed from the weld fusion line displays evidence of considerable grain refining (with average grain sizes between 18 and 22 μm).

The average grain size in the HTHAZ, determined using the line intercept method, is shown in Figure 5.4 as a function of the heat input. As expected, the grain size of the HTHAZ adjacent to the fusion line increases with an increase in heat input. Higher heat input levels result in slower cooling rates, allowing more time for grain growth to take place during the weld thermal cycle.

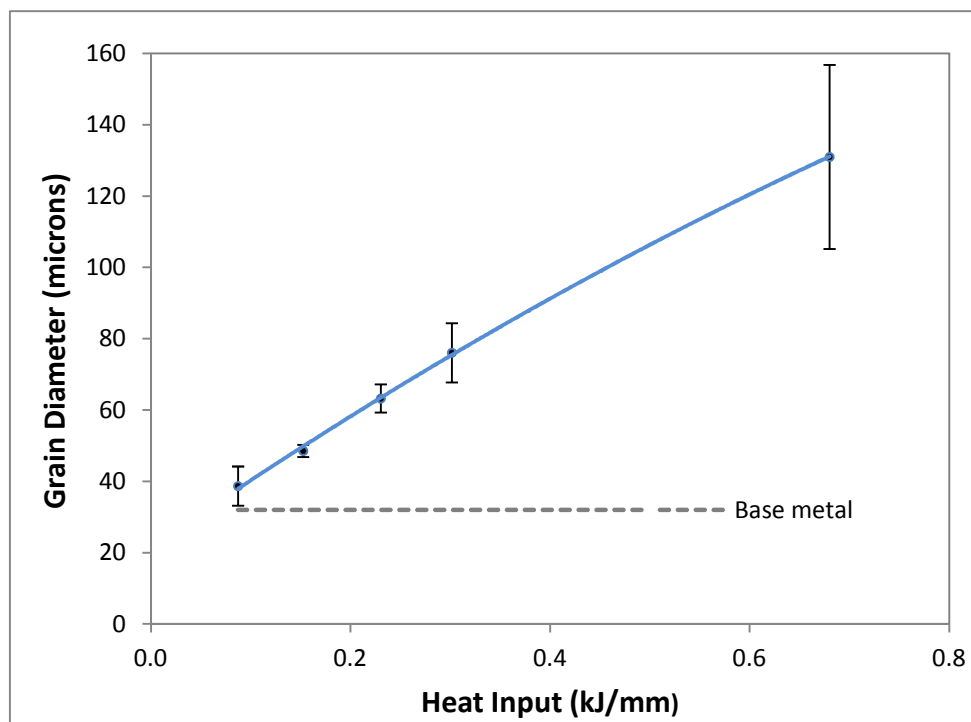


Figure 5.4: The average HTHAZ grain size as a function of weld heat input during GTAW. (See Table A1 in Appendix for experimental data).

Representative optical micrographs of the weld metal and heat-affected zones of welds performed at heat inputs between 0.09 and 0.45 kJ/mm after oxalic acid etching are shown in Figures 5.5(a) to (d). Oxalic acid etching removes chromium-rich carbides and reveals the location of grain boundary carbide precipitation as ditches in the microstructure. After welding at a very low heat input of 0.09 kJ/mm, there is little evidence of carbide precipitation in the weld metal and HAZ (Figure 5.5(a)). An increase in heat input to 0.15 kJ/mm resulted in grain boundary carbide precipitation in a narrow band of the high temperature heat-affected zone adjacent to the fusion line (Figure 5.5(b)). After welding at 0.3 and 0.45 kJ/mm (Figures 5.5(c)

and (d)), carbides are evident in the weld metal and in a narrow band of the HTHAZ, with evidence of strong epitaxial solidification at the fusion line. There is also some evidence of fine precipitation in the HTHAZ adjacent to the fusion line, which was investigated in more detail using a high resolution scanning electron microscope (SEM).

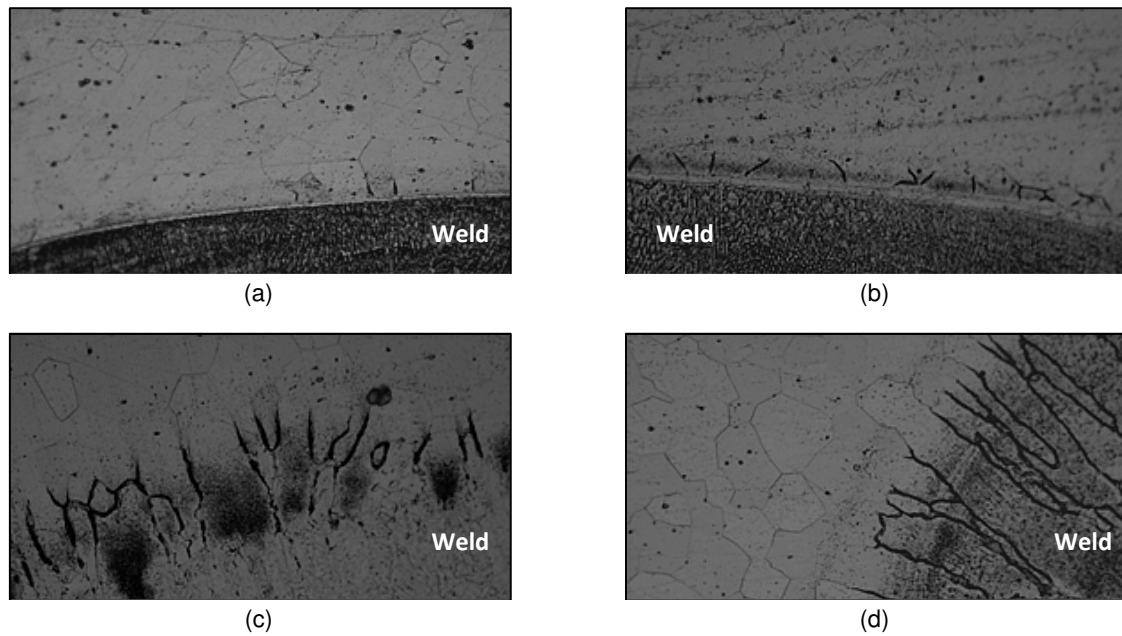


Figure 5.5: Optical photomicrographs of GTAW welds in type 441 ferritic stainless steel at heat input levels of: (a) 0.09 kJ/mm; (b) 0.15 kJ/mm; (c) 0.3 kJ/mm; and (d) 0.45 kJ/mm (electrolytic oxalic acid etch). (100x magnification). (See Table A4 in Appendix for orientation of micrographs).

Representative scanning electron micrographs of the weld metal of the autogenous type 441 welds are shown in Figures 5.6(a) and (b). The weld metal displays a characteristic columnar dendritic solidification structure. Higher magnification reveals the presence of a well-defined grain boundary dense precipitation, coarse intragranular particles similar in appearance to the grain boundary phase, and a homogeneous dispersion of fine intragranular needle-like precipitates with a well-defined orientation relationship with the underlying matrix. As shown in Figure 5.7, SEM-EDS (energy-dispersive X-ray spectroscopy) analysis confirmed the presence of high levels of niobium in the grain boundary phase, suggesting that the grain boundary precipitate, as well as the coarser particles within the grains, consist of intermetallic Laves phase (Fe_2Nb).

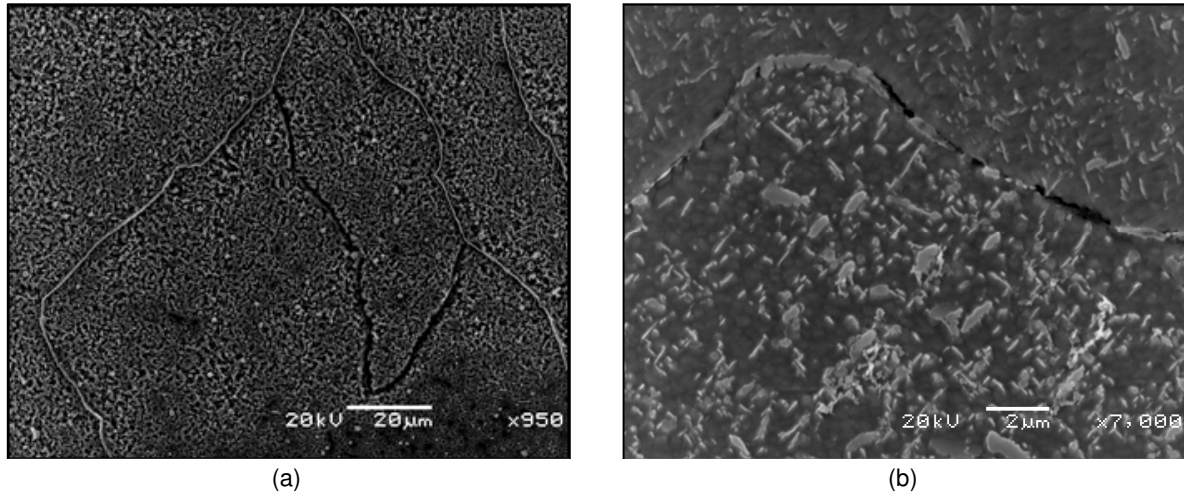


Figure 5.6: Representative scanning electron micrographs of the weld metal of autogenous 441 GTAW welds at two magnifications. (See Table A4 in Appendix for orientation of micrographs).

The time-temperature-transformation (TTT) diagram for Laves phase precipitation in type 441 (shown in Figure 2.10) indicates that transformation only starts after more than 600 seconds (for isothermal transformation). This suggests that the weld cooling rates, especially after welding at low heat inputs, would be too fast for Laves phase precipitation. During welding, however, the (Ti,Nb)C precipitates in the weld metal completely dissolve and at low heat inputs, there may not be enough time for these carbides to reprecipitate. The weld metal therefore has higher levels of niobium in solid solution, shifting the TTT diagram to shorter times. This may enable Laves phase precipitation during the weld thermal cycle.

The presence of Laves phase in the type 441 welds was confirmed by means of X-ray diffraction (XRD) analysis of the residue recovered after dissolving the matrix using hydrochloric acid (shown in Figure 5.8). XRD revealed the presence of the ferrite matrix, TiC precipitates, niobium-containing titanium-rich carbides and intermetallic Laves phase in the welded samples. In addition to Laves phase, preliminary investigation using transmission electron microscopy (TEM) revealed the presence of coarse precipitates in the weld metal, identified as FeCr sigma phase using selected-area electron diffraction (Figure 5.9).

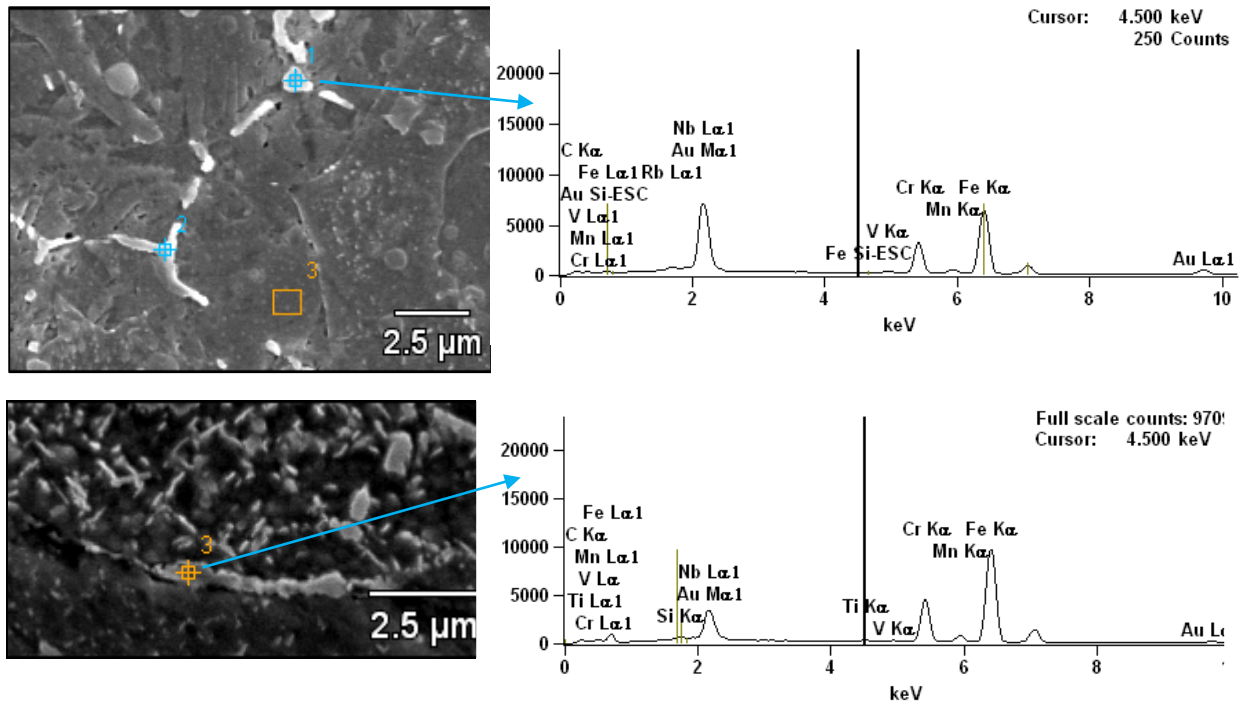


Figure 5.7: SEM-EDS analysis of the grain boundary phase observed in the weld metal of the GTAW autogenous welds.

Figures 5.10 (a) and (b) contain representative scanning electron micrographs of the heat-affected zone of welds performed at a low heat input level of 0.15 kJ/mm after electrolytic etching in nitric acid, Figure 5.10(a), and in oxalic acid, Figure 5.10(b). Rosenthal's heat flow equations [2] are the most widely used to estimate the temperature profile in the heat affected zone for a moving heat source. Thick plate solution is given below in equation (5.1). T is the temperature at a distance r from the heat source, T_o is the original temperature of the plate before welding, δ is thermal conductivity, q is the heat transferred to the plate, v is the welding speed, a is the thermal diffusivity, and r is the radial distance from the heat source.

$$T - T_o = \left(\frac{q/v}{2\pi\delta t} \right) \exp\left(-\frac{r^2}{4at} \right) \quad \dots (5.1)$$

The approximate temperature profile in the HTHAZ was calculated using Rosenthal's conduction-driven heat flow model [2] and is shown in Figure 5.11.

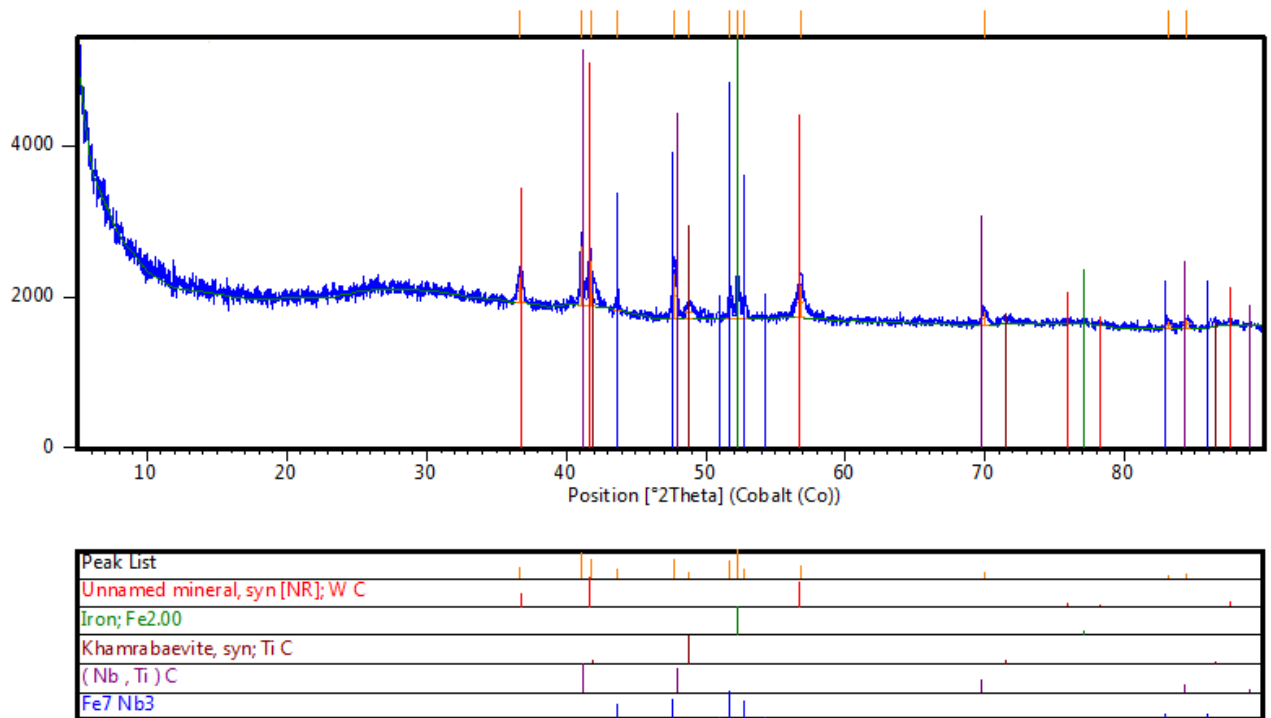


Figure 5.8: XRD analysis of the residue recovered after the matrix of a welded sample was dissolved in hydrochloric acid.

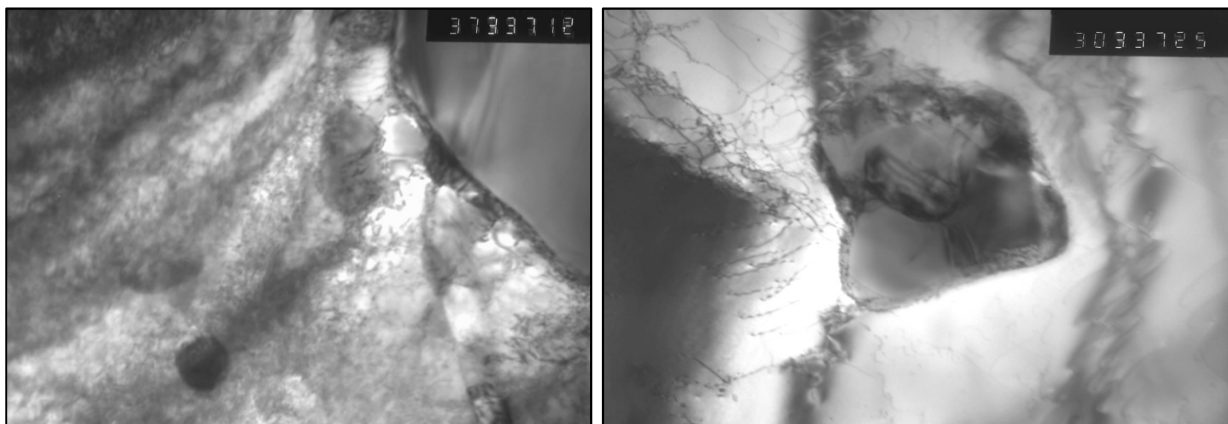


Figure 5.9: Thin foil TEM micrographs of GTAW weld done at a heat input of 0.77 kJ/mm containing coarse precipitates identified as intermetallic sigma phase using selected-area electron diffraction. (Photographs by Mr Stan Manziej).

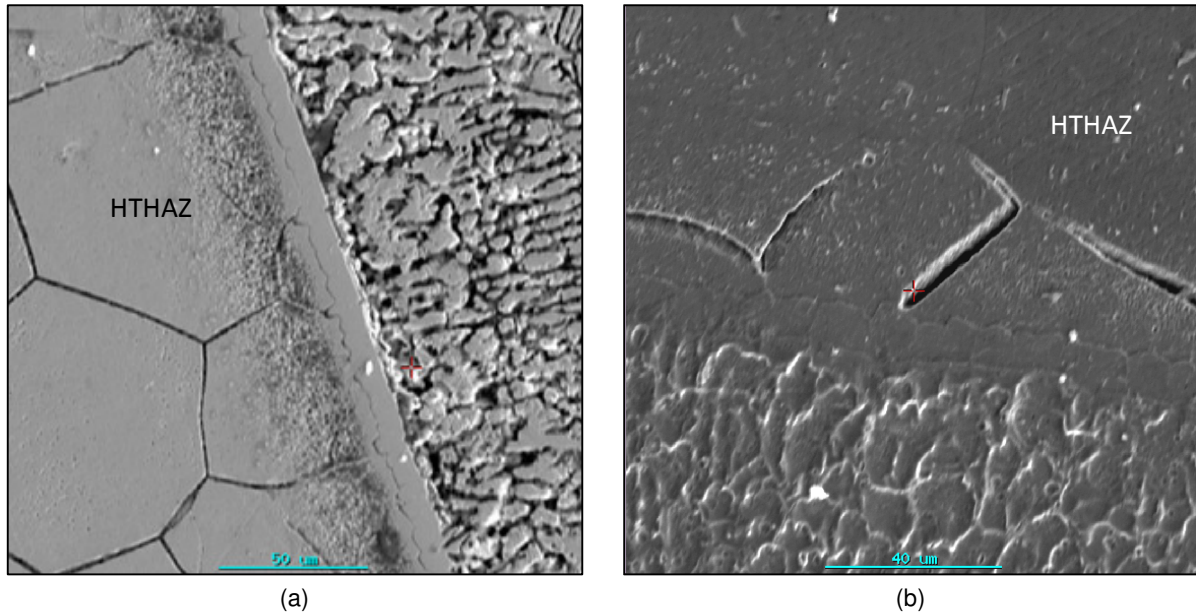


Figure 5.10: Scanning electron micrographs of a GTAW weld performed at a heat input level of 0.15 kJ/mm after electrolytic etching in: (a) nitric acid; and (b) oxalic acid. (See Table A4 in Appendix for orientation of micrographs).

Adjacent to the fine dendritic weld metal, a smooth, featureless band of material dissects Figure 5.10(a) at the fusion line. It is postulated that this zone represents metal that melted during the weld thermal cycle, but resolidified rapidly due to effective heat conduction into the base metal and the fast cooling rates associated with low heat input levels. This band of material appears to be mostly free of precipitates and second phase particles, suggesting that the high cooling rate after welding suppressed the precipitation of carbides, carbonitrides and intermetallic phases during cooling. The smooth featureless appearance of this zone suggests a planar solidification mechanism during the initial stages of the weld solidification process [3]. A steep temperature gradient into the liquid at the fusion line suppressed constitutional supercooling and allowed planar growth of the solidification front over a short distance during the initial stages of solidification. Shortly after the start of solidification, however, a decrease in temperature gradient and increased solute rejection at the solidification front promoted constitutional supercooling and the solidification front rapidly become unstable. Instability of the solidification front resulted in the formation of dendrites in the weld metal.

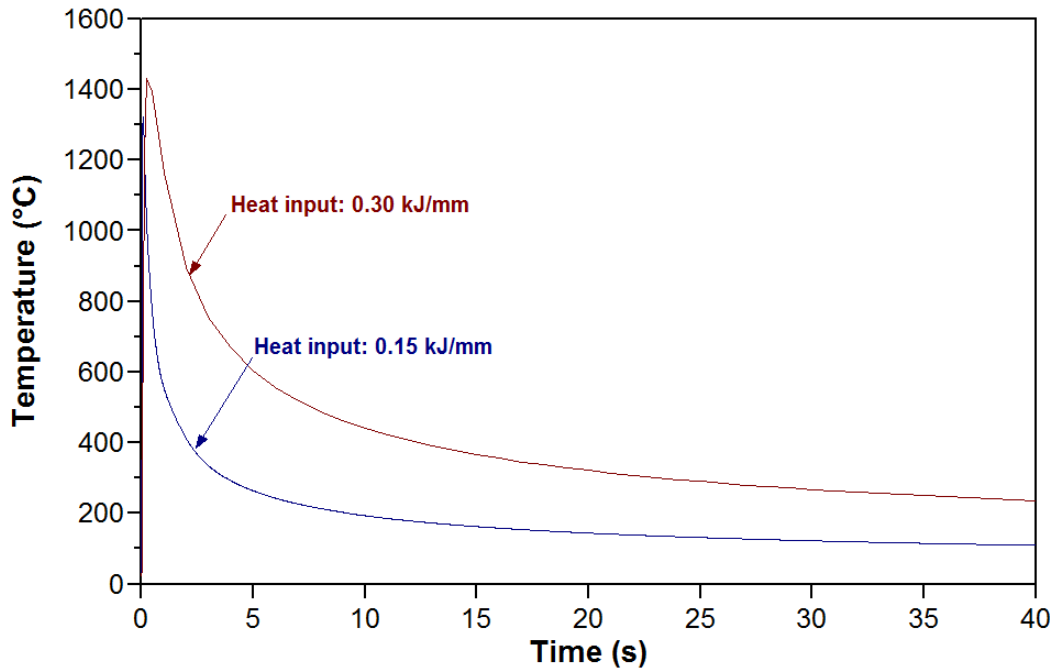


Figure 5.11: Calculated temperature cycles experienced by the high temperature heat-affected zone for heat inputs of 0.15 kJ/mm and 0.3 kJ/mm. The distance from the fusion line is 10 μm . (See Table A5 in the Appendix for the parameters used to estimate weld temperature cycles using Rosenthal's equation).

A band of material between the featureless zone and the bulk of the HTHAZ was observed to contain a high concentration of fine intragranular precipitates (Figure 5.10(a)). A higher magnification scanning electron micrograph, Figure 5.12, revealed a band of material containing fine needle-like precipitates near the fusion zone. These needle-like precipitates are similar in appearance to those observed in the weld metal (Figure 5.6(b)) and display a well-defined orientation relationship with the ferrite matrix. Although SEM-EDS analysis of these precipitates was inconclusive due to the small size of the particles, the particles were shown to contain niobium, titanium and carbon (Figure 5.13). The presence of similar needle-like precipitates in ferritic stainless steels has been confirmed by various authors. Silva *et al* [4] and Padilha and Machado [5] studied precipitation phenomena in dual-stabilised ferritic stainless steels and reported the presence of needle-like particles containing niobium and titanium. These authors concluded that the particles are most likely intermetallic Laves phase precipitates. Schmidova *et al* [6], however, reported the presence of these needle-like precipitates in titanium-stabilised type 1.4510 (or AISI 439) ferritic stainless steel, and similar precipitates have been observed in the high

temperature heat-affected zone of titanium-stabilised type 409 ferritic stainless steel welds [7]. Since types 439 and 409 ferritic stainless steel do not contain deliberate additions of niobium, the needle-like precipitates are unlikely to be Laves phase. Schmidova *et al* [6] reported high concentrations of titanium in these particles and provisionally identified the precipitates as titanium carbides. The TEM investigation performed during the course of this project confirmed that the thin plate-like particles are carbides. It is postulated that these titanium carbide particles nucleate on dislocations and incoherent twin boundaries, rather than on TiN precipitates, which may account for the departure in shape from the more widely observed cuboidal TiC form.

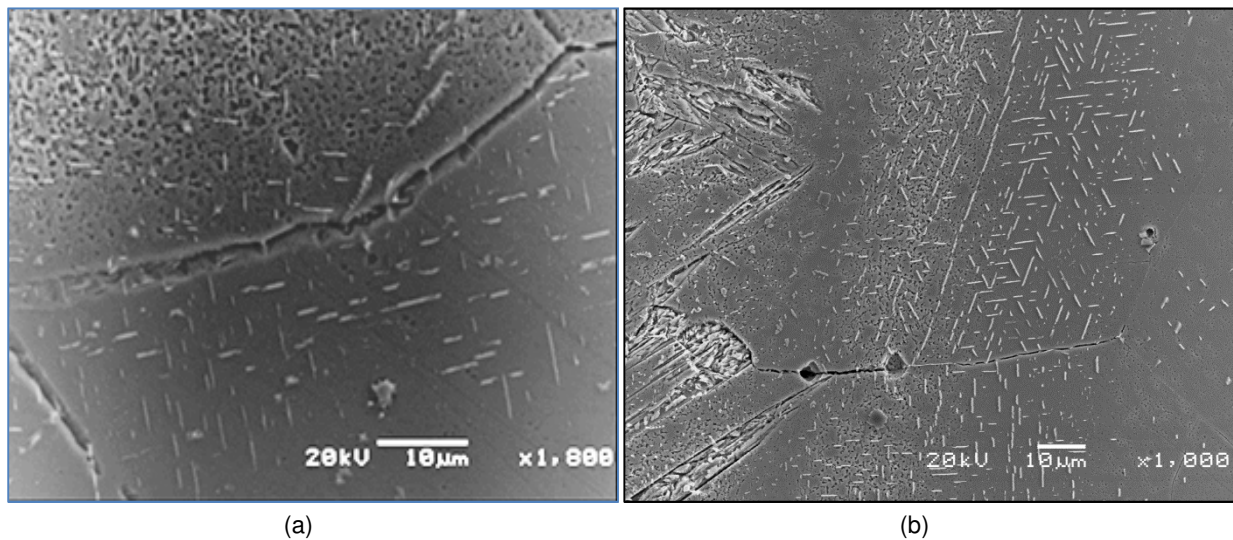


Figure 5.12: Higher magnification scanning electron micrographs of the HTHAZ of GTAW welds performed at: (a) 0.23 kJ/mm; and (b) 0.77 kJ/mm (electrolytic HNO₃ etch). (See Table A4 in Appendix for orientation of micrographs).

Figure 5.10(b) also shows evidence of a band of material in the HTHAZ (coinciding with the zone of material containing needle-like TiC precipitates) that displays severely ditched grain boundaries after oxalic acid etching. Grain boundary attack is also evident in Figure 5.12 after electrolytic nitric acid etching. Ditching of stainless steel during oxalic acid etching suggests that grain boundary Cr-rich M₂₃C₆ carbides formed on cooling following the partial dissolution of Nb and Ti-containing carbonitrides at higher temperatures. On cooling some of the titanium and niobium are retained in solid solution, and Cr-rich carbides are able to form on the ferrite grain boundaries when the temperature reaches the M₂₃C₆ precipitation range. The

Cu-CuSO₄-H₂SO₄ boiling acid test (described in Practice Z or ASTM 763-93) confirmed that the grain boundaries in the HTHAZ are sensitised.

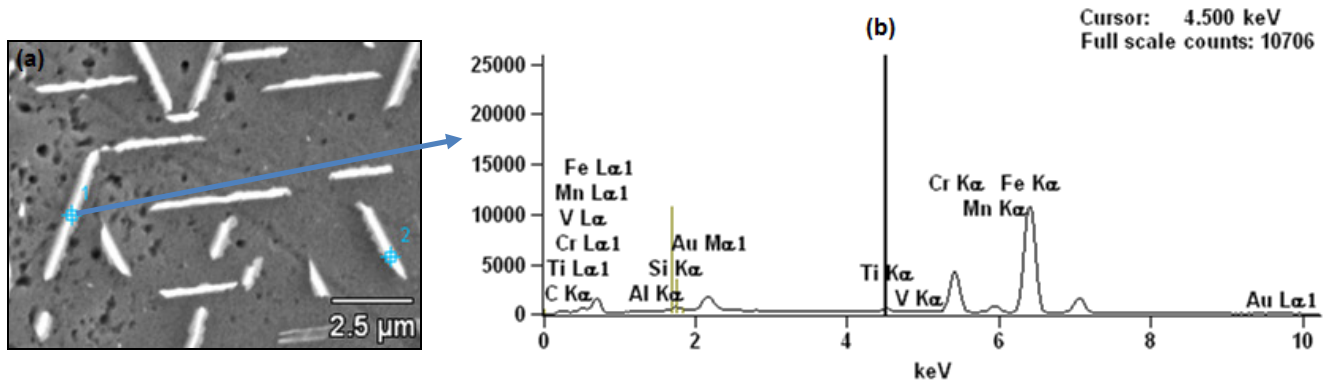


Figure 5.13: SEM-EDS analysis of the needle-like phase observed in the weld metal and HTHAZ of the autogenous GTAW welds.

Figures 5.14(a) and (b) contain representative scanning electron micrographs of welds performed at a heat input level of 0.45 kJ/mm after electrolytic etching in nitric acid, Figure 5.14(a), and in oxalic acid, Figure 5.14(b). At higher heat input levels, a smoother transition is evident between the weld metal and the heat-affected zone, and the featureless zone is absent or less well defined. This can be attributed to the slower cooling rates associated with higher heat input welding (as shown in Figure 5.11), which allowed the weld metal and the HTHAZ to sensitise during the weld thermal cycle. Ditching, indicative of the presence of Cr-rich M₂₃C₆ carbides, is evident along the columnar grain boundaries in the HTHAZ (Figure 5.14(b)), extending into the weld metal through a mechanism of epitaxial solidification. In the weld metal and HTHAZ close to the fusion line, the peak temperatures during welding were high enough to cause full or partial dissolution of Ti- and Nb-rich carbonitrides during welding. As shown in Figure 5.11, the cooling rate through the precipitation range of the alloy carbonitrides at higher temperatures after welding is significantly faster than the cooling rate at lower temperatures through the M₂₃C₆ precipitation range (below approximately 870°C). At heat inputs of 0.3 and 0.45 kJ/mm, the cooling rate in the weld metal and HTHAZ after solidification was therefore fast enough through the precipitation range of the alloy carbonitrides to prevent extensive reprecipitation of Ti- and Nb-rich carbonitrides and carbon was retained in solid solution. The slower cooling rate through the M₂₃C₆ precipitation range at lower temperatures allowed the formation of Cr-rich carbides at the grain boundaries, resulting in chromium depletion and sensitisation.

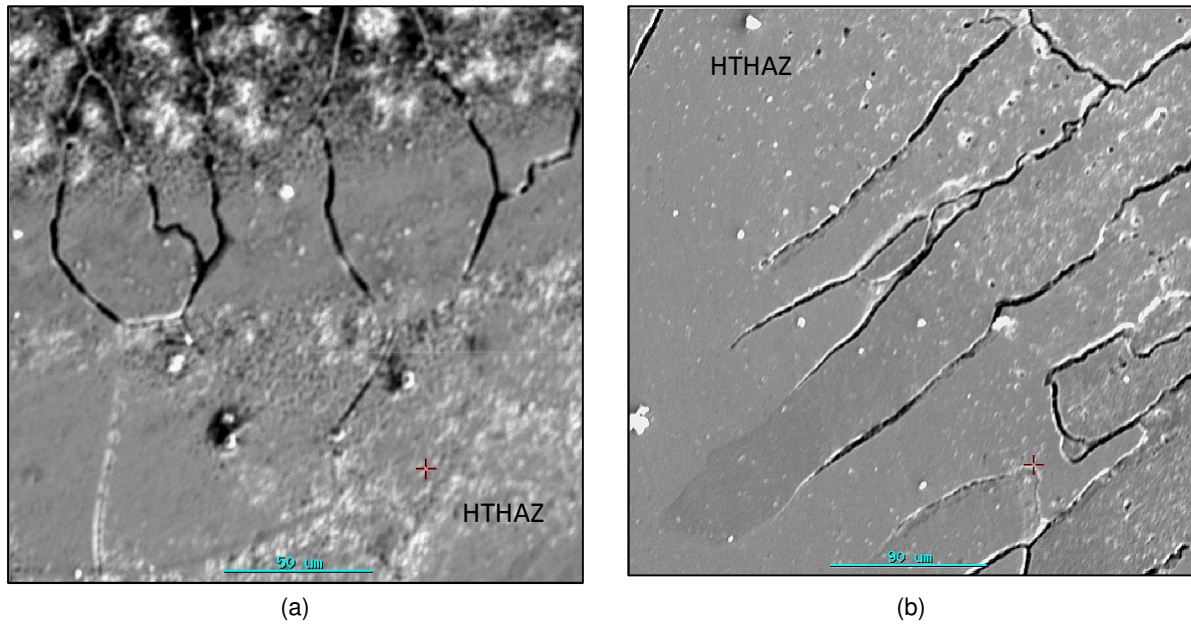


Figure 5.14: Scanning electron micrographs of a GTAW weld performed at a heat input level of 0.45 kJ/mm after electrolytic etching in: (a) nitric acid; and (b) oxalic acid. (See Table A4 in Appendix for orientation of micrographs).

As shown in Figure 5.15, the Cu-CuSO₄-H₂SO₄ boiling acid test (described in Practice Z or ASTM 763-93) confirmed that the grain boundaries in the weld metal and high temperature HAZ are sensitised. Beyond the sensitised region (characterized by grain boundary ditching), the Ti- and Nb-rich carbonitrides in the base metal did not fully go into solution during the weld thermal cycle (lower peak temperatures) and some overageing and coarsening of the precipitates occurred (as illustrated by the high precipitate density in the lower half of Figure 5.14(a)). M₂₃C₆ precipitation did not occur at lower temperatures as very little carbon was retained in solid solution to react with chromium. Sensitisation was largely suppressed in samples welded at heat inputs of 0.7 kJ/mm or higher.

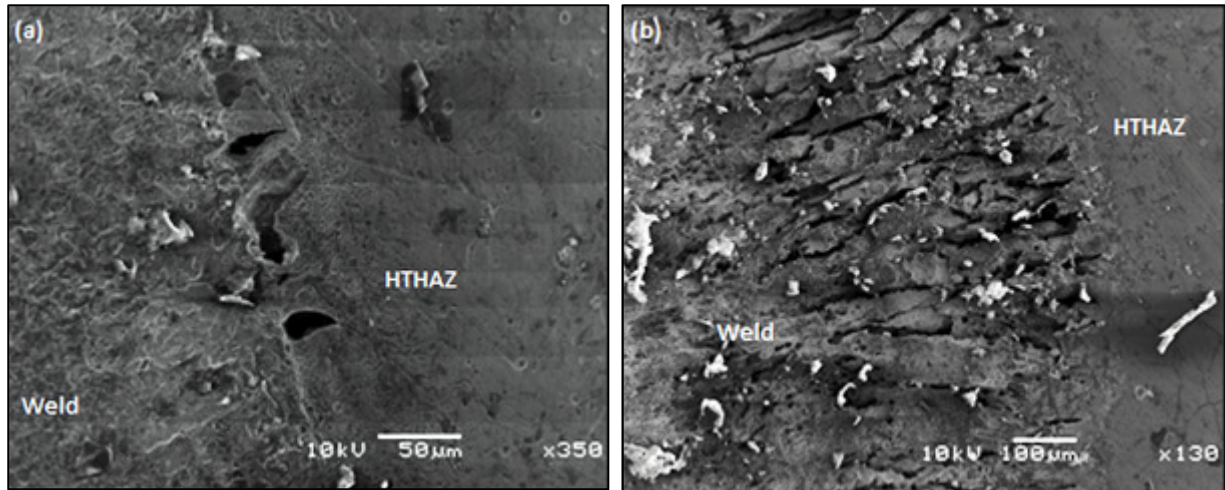


Figure 5.15: SEM micrographs of ditched grain boundaries in the weld metal and HTHAZ after exposure to the $\text{Cu-CuSO}_4\text{-H}_2\text{SO}_4$ boiling acid test (described in Practice Z of ASTM 763-93) for GTAW welds performed at heat inputs of: (a) 0.23 kJ/mm; and (b) 0.45 kJ/mm. (See Table A4 in Appendix for orientation of micrographs).

5.3 MICROSTRUCTURES OF LASER BEAM WELDS

Figure 5.16 shows optical photomicrographs of the weld metal, heat-affected zone and surrounding base metal of autogenous laser welds performed at heat inputs of 0.11 kJ/mm and 0.23 kJ/mm. The microstructures of all three zones are fully ferritic. The weld metal microstructure consists of columnar ferrite grains bending in towards the weld centreline. Although epitaxial solidification took place at the fusion line, the low heat inputs resulted in weld metal with a finer grain size than that of the gas tungsten arc welds. The grain size of the HAZ appears to be marginally coarser than that of the base material. The localised grain refinement observed in the LTHAZ of the gas tungsten arc welds is not as evident in the laser welds.

Scanning electron micrographs of the weld metal and heat-affected zone of an autogenous laser weld performed at a heat input of 0.11 kJ/mm are shown in Figures 5.17(a) and (b), respectively. The weld microstructure, Figure 5.17(a), appears to be fully ferritic and does not contain any visible second phase particles. This can be attributed to complete dissolution of intermetallic phases and (Ti,Nb)C during heating and melting of the weld metal. As a result of the rapid cooling rates associated with low heat input laser welding, reprecipitation was suppressed during cooling and the

weld metal is supersaturated in niobium, titanium and carbon. The heat-affected zone microstructure, shown in Figure 5.17(b), is largely ferritic, but some cuboidal (Ti,Nb)C precipitates are visible. This suggests that the lower peak temperatures in the heat-affected zone resulted in incomplete dissolution of (Ti,Nb)C during heating. Although there is evidence of heterogeneous nucleation on the (Ti,Nb)C particles, extensive reprecipitation did not occur on cooling.

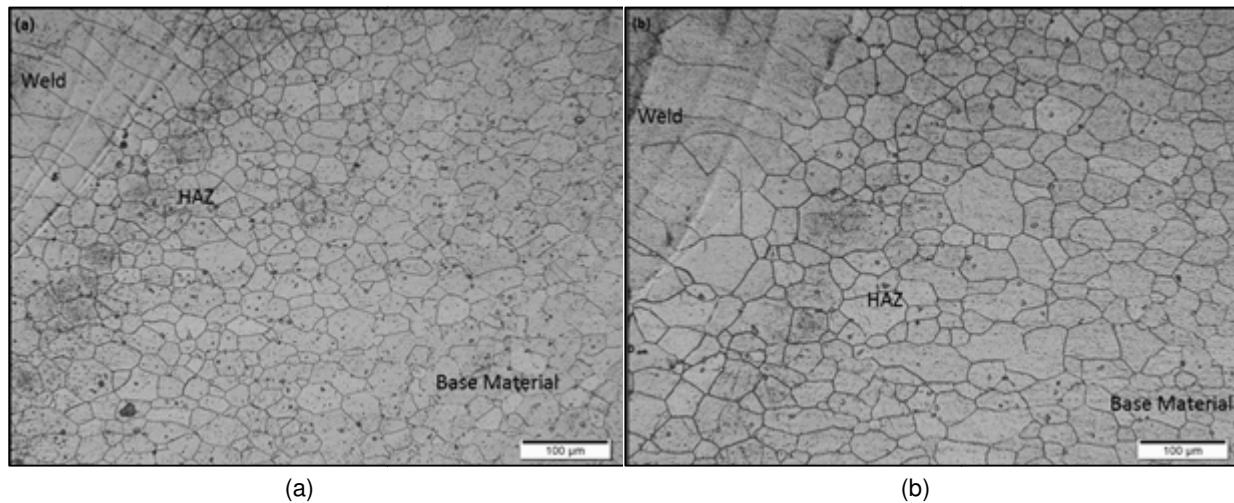


Figure 5.16: Microstructure of the heat-affected zone of LBW welds performed at effective heat input levels of: (a) 0.11 kJ/mm; and (b) 0.23 kJ/mm. (Electrolytic HNO₃ etch). (See Table A4 in Appendix for orientation of micrographs).

Figures 5.18(a) and (b) contain scanning electron micrographs of the weld and heat-affected zone, respectively, of a weld performed at a heat input of 0.23 kJ/mm. The microstructures are very similar to those observed in Figure 5.17. The microstructure of the weld metal is ferritic and does not contain any visible second phase particles. Isolated gas porosity is, however, evident. As a result of the higher heat input and correspondingly slower cooling rate, the HAZ grain size is coarser than that shown in Figure 5.17(b). The HAZ contains a number of coarse (Ti,Nb)C precipitates. The darker centre of the coarse carbide particle in Figure 5.18(b) suggests that TiN precipitated first from the melt, followed by (Ti,Nb)C nucleation on the TiN particles. There appears to be some evidence of nucleation on the (Ti,Nb)C particle in Figure 5.18(b), suggesting limited reprecipitation on cooling after welding.

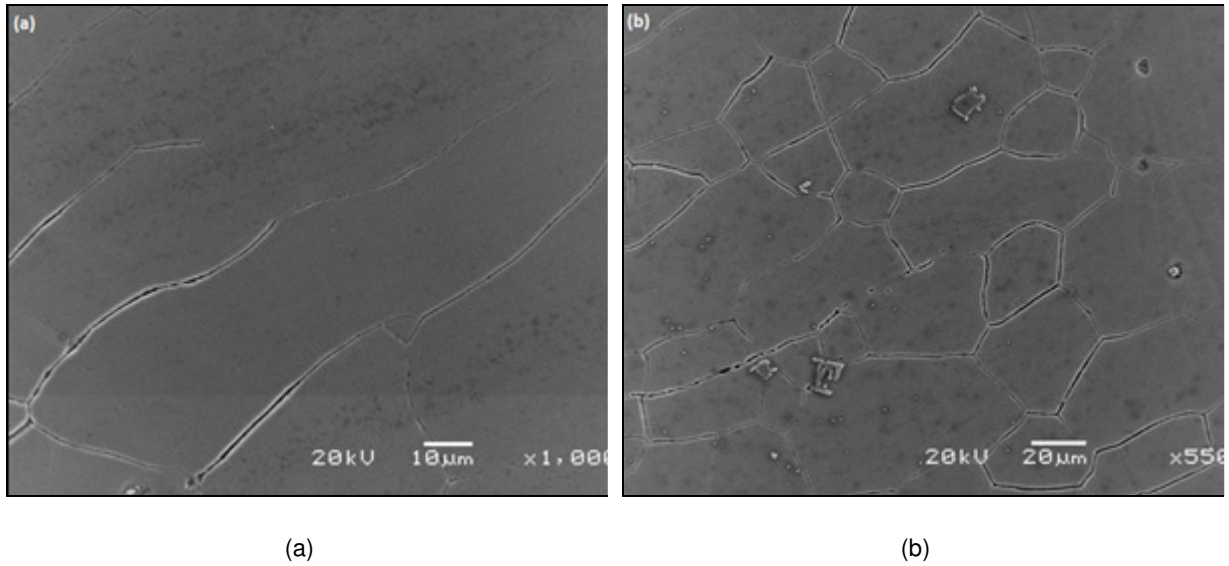


Figure 5.17: SEM micrographs of the: (a) weld metal; and (b) heat-affected zone, of a LBW weld performed at heat input of 0.11 kJ/mm. (See Table A4 in Appendix for orientation of micrographs)

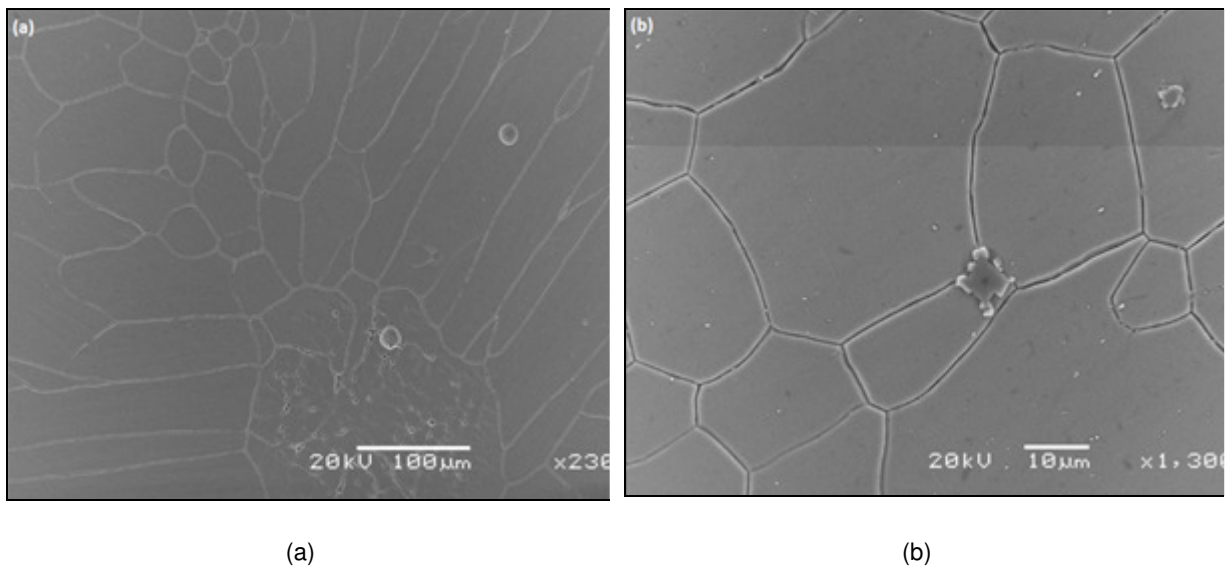


Figure 5.18: SEM micrographs of the: (a) weld metal; and (b) heat-affected zone, of a LBW weld performed at heat input of 0.23 kJ/mm. (See Table A4 in Appendix for orientation of micrographs)

Figure 5.19 compares the measured grain size in the HTHAZ for GTAW and LBW welds as a function of heat input. It is evident that the HAZ grain size increases with an increase in heat input. The heat input affects the heating and cooling rates, and therefore the time spent above the grain growth temperature range during the weld thermal cycle. For type 441 steel, grain growth occurs at temperatures above approximately 925°C. It is evident that laser welds are considerably finer than GTAW

welds produced at the same heat input. This can be attributed to the difference in grain structure formed on cooling. Laser welding produces deep, narrow welds, whereas GTAW produces welds with significantly lower depth-to-width ratios. LBW also produces steeper thermal gradients which reduces grain growth [8]. It is also important to note that the grain size in the HAZ of the laser weld produced at 0.11 kJ/mm seems to be finer than that the base material. This can be attributed to the very fast cooling rate of the weld.

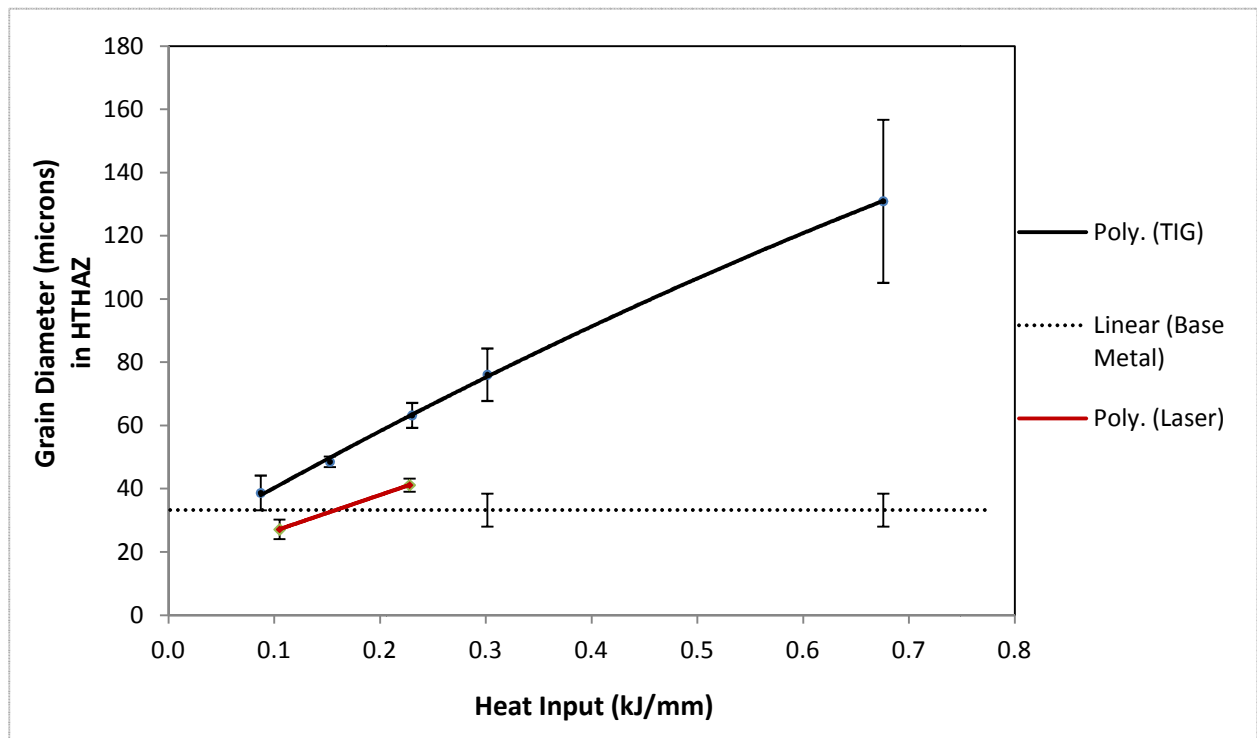


Figure 5.19: Grain size as the function of heat input for GTAW and LBW welds (with 95% confidence interval). (Data used to plot this graph is given in Table A1 and A2 in the Appendix).

Optical photomicrographs of the weld metal and heat-affected zone of laser welds performed at heat inputs of 0.11 and 0.23 kJ/mm after oxalic acid etching are shown in Figures 5.20(a) and (b), respectively. The presence of ditched grain boundaries after oxalic acid etching is generally indicative of the presence of $M_{23}C_6$ carbides at the grain boundaries. Grain boundary carbide precipitation is evident in the weld metal and high temperature heat-affected zone of welds performed at a heat input of 0.11kJ/mm, suggesting that the welds are sensitised to intergranular corrosion. The (Ti,Nb)C particles partially dissolve during the heating cycle, but do not reprecipitate on cooling due to the fast cooling rates in the elevated temperature part of the weld

thermal cycle. At lower temperatures in the $M_{23}C_6$ precipitation range, the cooling rate is slower, allowing extensive chromium-rich carbide precipitation at grain boundaries. After welding at 0.23 kJ/mm, extensive grain boundary carbide precipitation is evident in the weld and the HTHAZ, with the grain boundary carbide precipitation extending one to two grain diameters into the HTHAZ (see Figure 5.20(b)). The cooling rate of the 0.23 kJ/mm weld is still fast enough to suppress reprecipitation of stabilising carbides at higher temperatures, but slow enough at lower temperatures to allow extensive $M_{23}C_6$ precipitation on cooling.

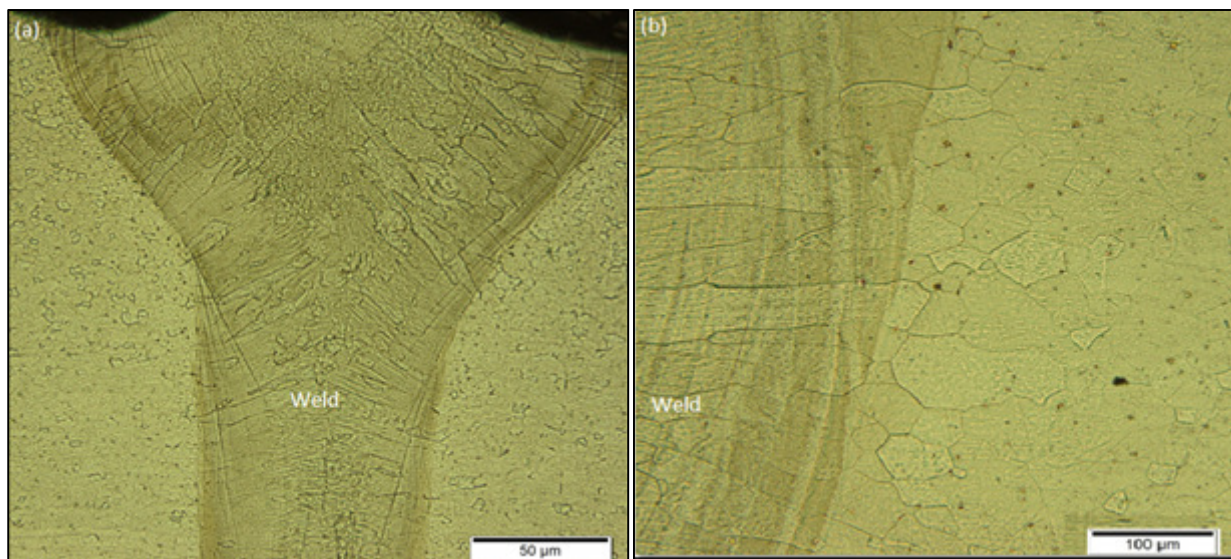


Figure 5.20: Optical micrographs of LBW welds at effective heat input levels of: (a) 0.11 kJ/mm; and (b) 0.23 kJ/mm. (Oxalic acid etch). (See Table A4 in Appendix for orientation of micrographs)

Sensitisation was confirmed by means of the Cu-CuSO₄-H₂SO₄ test described in Practice Z of ASTM A763-93. Figure 5.21 below shows scanning electron micrographs of welds performed at 0.11 and 0.23 kJ/mm after hot acid etching. It is evident that after welding at a heat input of 0.11 kJ/mm, there is extensive ditching at the grain boundaries of the columnar grains in the weld metal. These ditched grain boundaries extend approximately 20 µm into the HTHAZ (see Figure 5.21(a)). After welding at 0.23 kJ/mm, the weld metal and the HTHAZ are sensitised. The laser welds appear to be more resistant to sensitisation than the GTAW welds. This can be attributed to the fast cooling rates associated with laser welding that suppress $M_{23}C_6$ carbide precipitation.

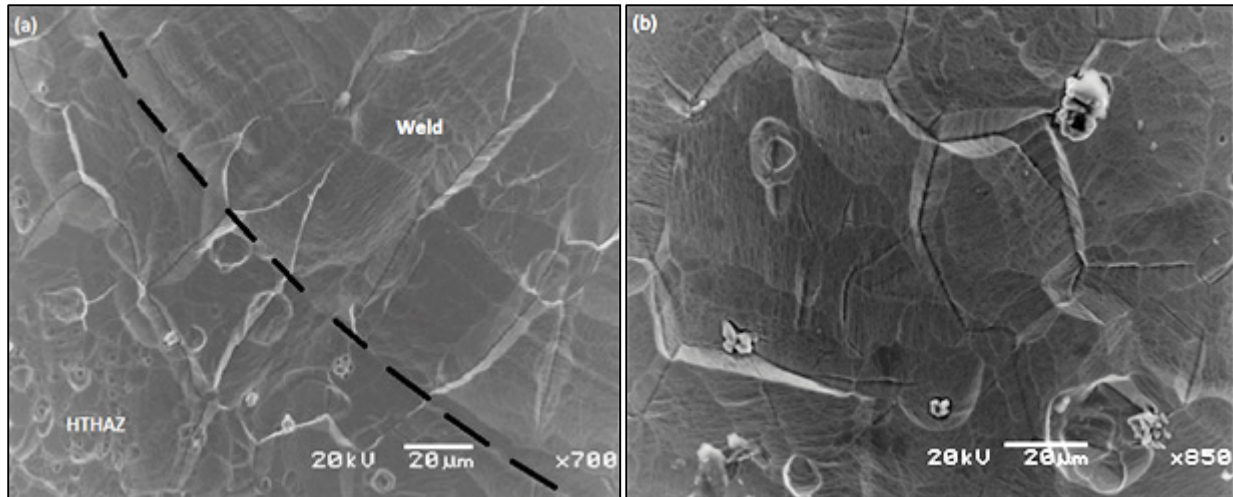


Figure 5.21: SEM micrographs of LBW welds performed at: (a) 0.11 kJ/mm; and (b) 0.23 kJ/mm, after the boiling hot acid test (Practice Z of ASTM A763-93). (See Table A4 in Appendix for orientation of micrographs).

5.4 GRAIN REFINEMENT EFFECT IN THE LTHAZ OF GAS TUNGSTEN ARC WELDS

Figure 5.22 shows an optical photomicrograph of the HAZ and base material of a GTAW weld performed at a heat input of 0.3 kJ/mm. Three distinct zones are visible, namely the HTHAZ, LTHAZ and the base material. The average grain sizes in the base material, HTHAZ and LTHAZ are superimposed on Figure 5.22. The coarse grain size in the HTHAZ can be attributed to the high peak temperatures experienced adjacent to the fusion line during welding. The LTHAZ, however, has an average grain size of 18 μm , which is finer than the average grain size in the base material (32 μm). It is apparent that grain refinement occurred in this region during the weld thermal cycle.

Figure 5.23 shows the measured hardness profile in the HAZ of the weld shown in Figure 5.22. The weld metal has a high hardness of 270 $\text{HV}_{0.3}$ (hardness on the Vickers scale) due to Laves and sigma phase precipitation. The hardness decreases beyond the fusion line in the HTHAZ, but an increase in the hardness to 200 $\text{HV}_{0.3}$ is evident at a distance of approximately 0.1 mm from the fusion line. This can be attributed to the presence of needle-shaped titanium-rich carbides in a band parallel to the fusion line in the HTHAZ (see Figure 5.12). Beyond this point the hardness decreases to a constant value of approximately 160 $\text{HV}_{0.3}$. At approximately 0.8 mm

away from the fusion line, there is another increase in hardness to 170 HV_{0.3} in the LTHAZ. This distance corresponds to the grain refined region observed in the LTHAZ, suggesting that the grain refinement effect in the LTHAZ is not an artefact, but a real phenomenon. The mechanism of grain refinement in the LTHAZ is, however, not clear.

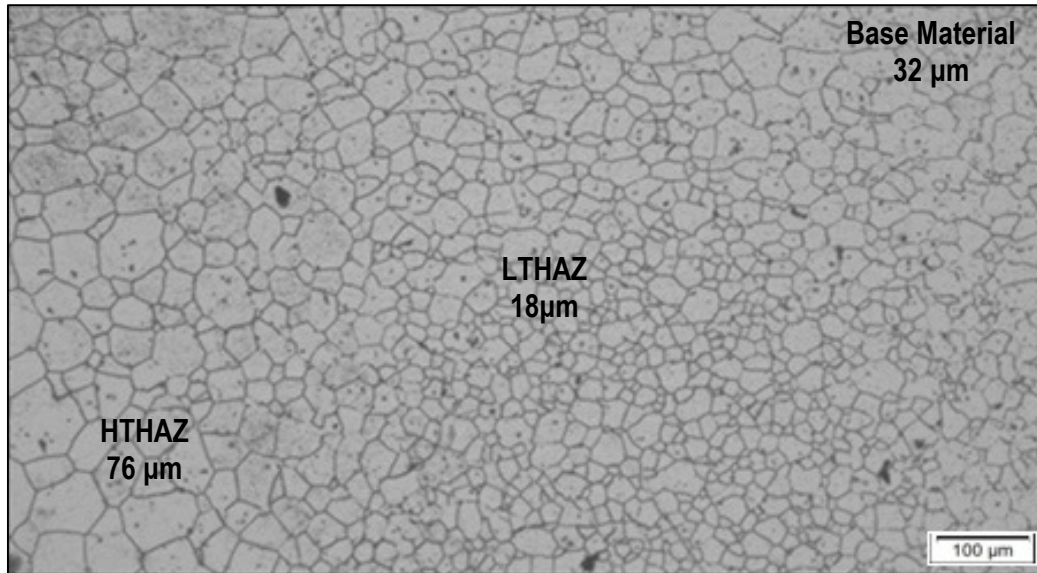


Figure 5.22: Optical photomicrograph of the HAZ of a GTAW weld performed at 0.3 kJ/mm (electrolytic HNO₃ etch). (See Table A4 in Appendix for orientation of micrographs).

In order to study the grain refinement effect, the thermal cycles in the heat-affected zone at a position corresponding to the LTHAZ hardness peak were calculated. Figure 5.24 shows the temperature profiles in the LTHAZ for the band of material that showed grain refinement. It is evident that the peak temperatures in the grain refined region range between approximately 800°C to 1000°C.

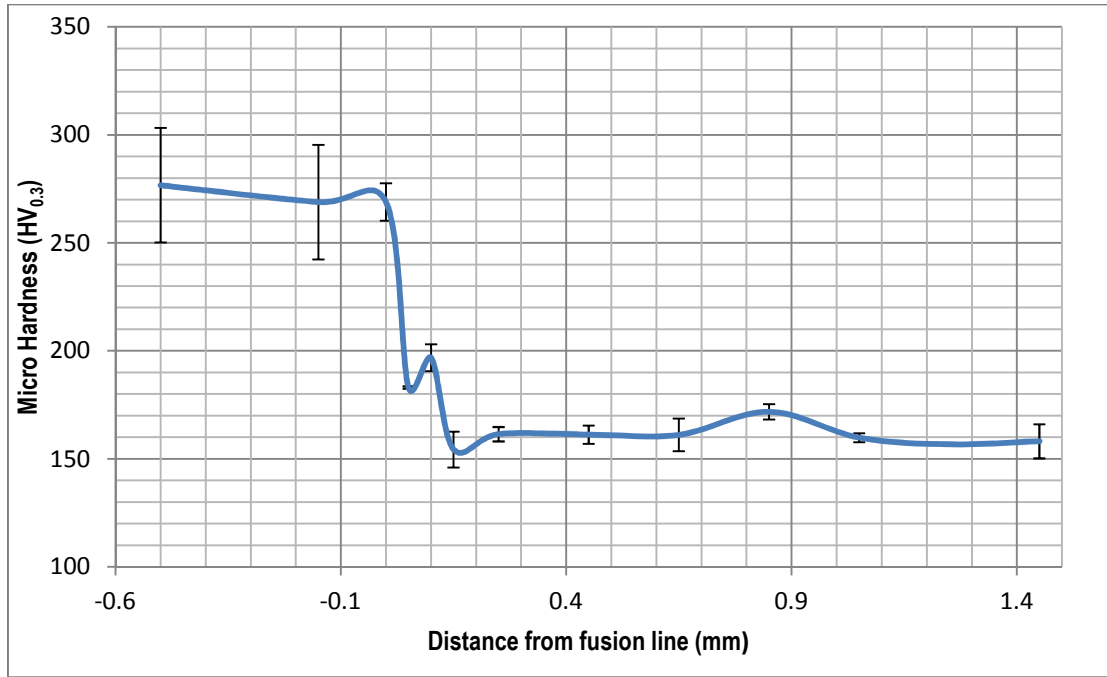


Figure 5.23: Microhardness profile across the HAZ of a weld performed at 0.3 kJ/mm (with 95% confidence interval). (Every data point represents the average of three hardness values. Data used to plot this graph is given in Table A3 in the Appendix.)

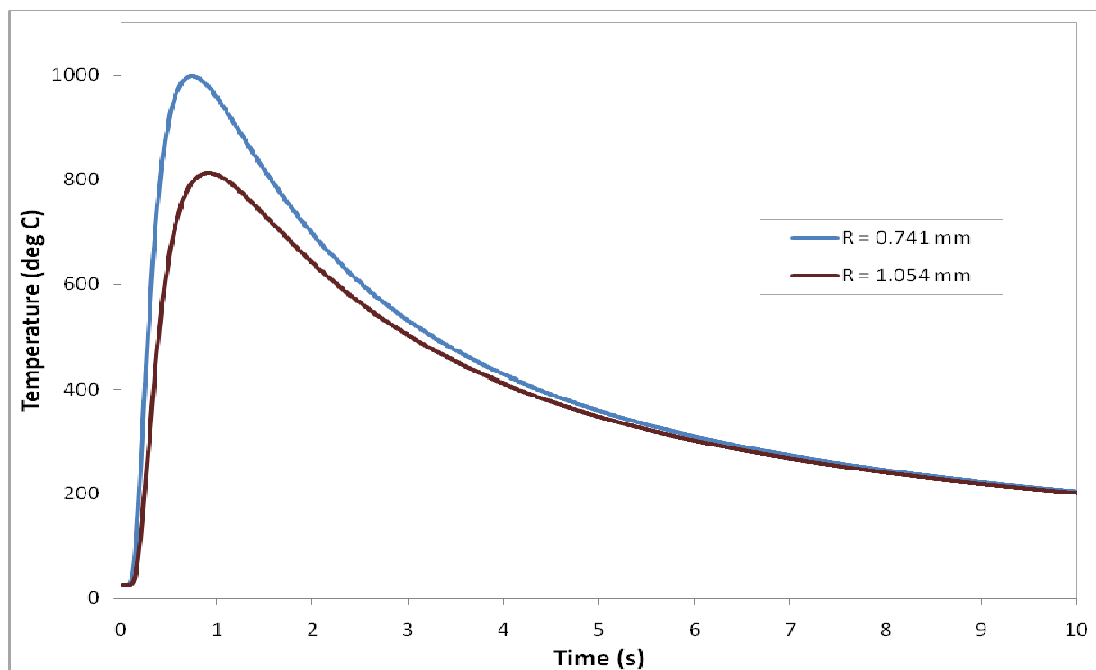


Figure 5.24: Temperature profiles in the LTHAZ of a weld performed at 0.3 kJ/mm (corresponding to a band of material displaying grain refinement). R is the distance from the fusion line. (The parameters used to plot this graph are given in Table A5 in the Appendix).

Since a solid state phase transformation appears to be the only possible explanation for this phenomenon, a dilatometer was used to determine if a phase transformation occurs in type 441 during the heating and cooling thermal cycle. Figure 5.25 shows the dilatometer results as the change in length of a specimen with a change in temperature. A phase transformation is marked by a sudden kink (expansion or contraction) on the curve. It is clear from Figure 5.25 that there is an inflection point in the curve between 640°C and 680°C during heating, and just below 680°C on cooling, which may be due to sigma phase dissolution and reprecipitation. There is no evidence of a phase transformation at temperatures above 700°C. This is in agreement with the Thermo-Calc™ results shown in Figure 5.1, which showed that ferrite is stable at all temperatures in the solid state.

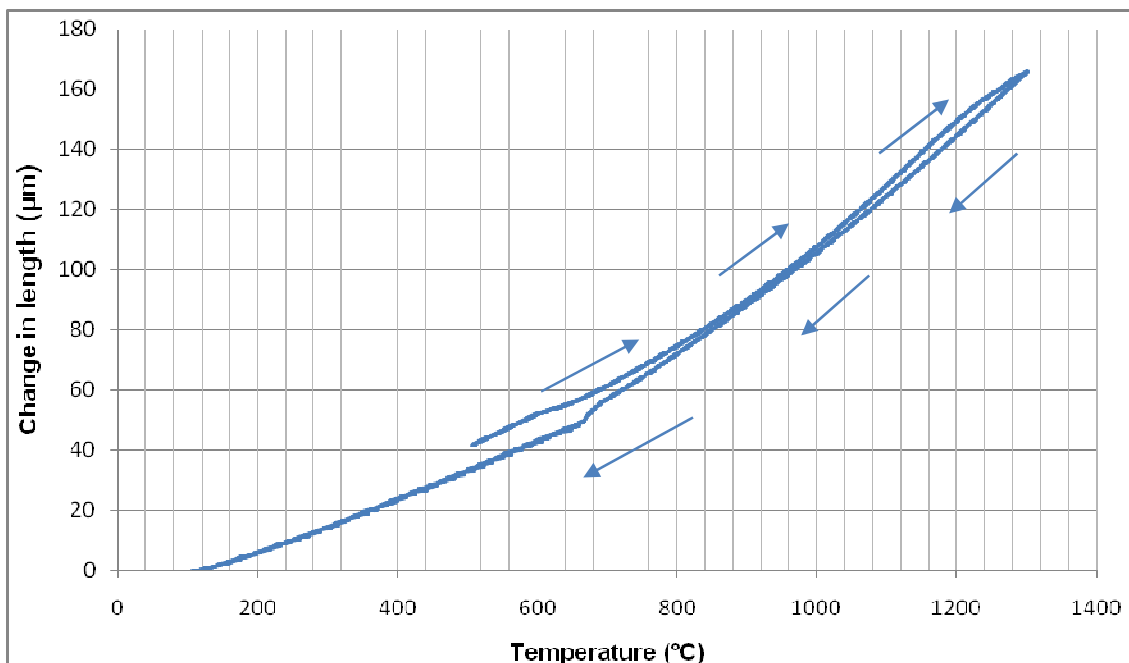


Figure 5.25: Dilatometer curves showing the change in length as a function of temperature during heating and cooling. Heating and cooling are done at 153 °C/s. The heating cycle is shown by the arrows pointing right-up and cooling cycle shown by arrows pointing left-down.

Figure 5.26(a) below shows a gas tungsten arc weld performed at a heat input of 0.3 kJ/mm without prior heat treatment, whereas Figure 5.26(b) shows a gas tungsten arc weld that was heat treated at 600°C for 1.5 hours and water quenched before welding at the same heat input level. Grain refinement in the LTHAZ is evident in Figure 5.26(a), suggesting that the effect is repeatable. However, in the weld heat treated at 600°C and water quenched prior to welding, the LTHAZ is not as clearly defined (see Figure 5.26(b)) and the grain refinement effect not as evident.

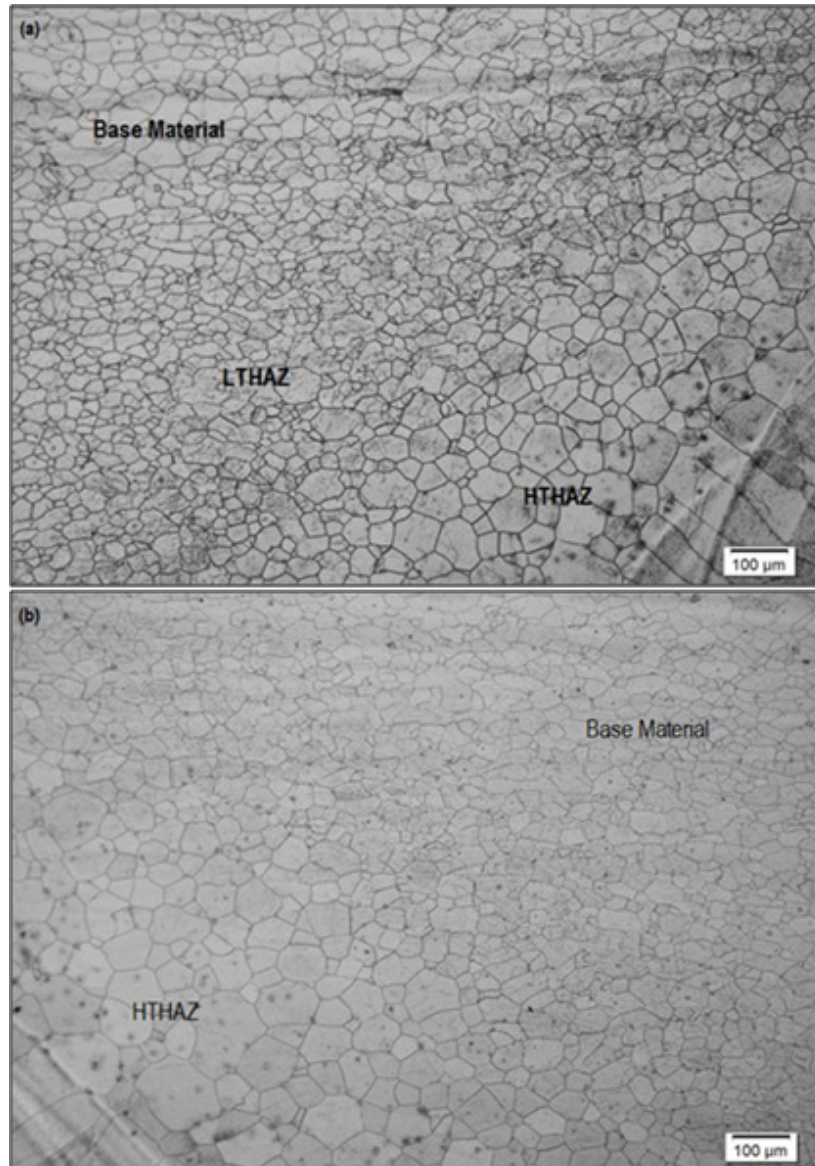


Figure 5.26: GTAW welds performed at heat inputs of 0.3 kJ/mm (etched electrolytically in 55% nitric acid): (a) welded without prior heat treatment; and (b) heat treated at 600 °C for 1.5 h prior to welding. (See Table A4 in Appendix for orientation of micrographs).

The mechanism responsible for grain refinement in the LTHAZ is still not understood, but it is clear from the dilatometry results (see figure 5.25) that no high temperature phase transformation occurs in this steel. Grain refinement due to a phase transformation can therefore not be used to explain grain refinement in the low temperature heat affected zone. Another possibility for the refinement in the LTHAZ is that recrystallisation occurred in LTHAZ. Plastic straining invariably occurs in a fusion welded joint. At the peak temperatures encountered in the LTHAZ (peak temperature between 1000 and 800 °C (see figure 5.24) recrystallisation is possible.

It is not clear, however, why, in a single pass welded joint, such recrystallisation occurs only in the low temperature heat affected zone. The hypothesis, that grain refinement in the LTHAZ is the result of plastic strain followed by recrystallisation, remains speculative.

5.5 MECHANICAL PROPERTIES

Figure 5.27 shows weld penetration achieved in GTAW and LBW welds as a function of heat input. It is evident that LBW welds achieved good penetrations compared to GTAW welds. It is also evident that penetration increased as the heat input increased for both GTAW and LBW, but it was observed that GTAW welds became wider than deeper as the heat input increased. Full penetration was not achieved in GTAW welds (the depth of weld pool was less than 40% of sheet thickness for all GTAW welds). As a consequence, the tensile and impact toughness of GTAW welds represent the properties of weld metal, heat affected zone and base metal, with relative contribution of the various parts of the welded joint dependent on the penetration. The mechanical properties of GTAW joints were not considered and presented during the current study. The tensile and Charpy test results for LBW welds will be considered because good penetration has achieved in these welds.

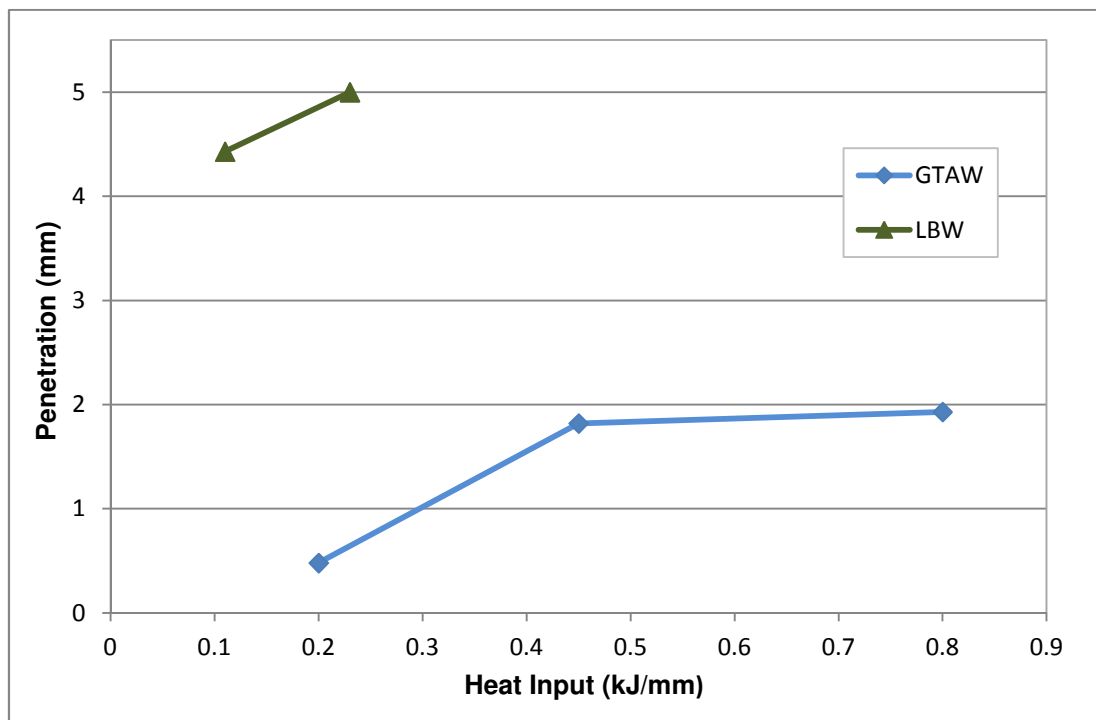


Figure 2.27: The effect of heat input on weld penetration of GTAW and LBW welds. Plate thickness was 5 mm in all welds.

Figure 5.28 compares the tensile properties of the base material and the laser welds, whereas Figure 5.29 shows stress-strain curves for the transverse tensile tests. The specimen welded at 0.11 kJ/mm fractured in the weld metal (fusion zone), whilst the specimen welded at 0.23 kJ/mm fractured in the HAZ near the fusion line. Table 5.1 summarises the tensile test results, weld penetration depths and fracture positions of LBW welds at different heat inputs.

Table 5.1: Tensile properties (UTS and Elongation), and the penetration of LBW welds as a function of heat input.

Heat Input (kJ/mm)	UTS (MPa)	Elongation (%)	Weld Penetration Depth (mm)	Fracture Position
Base Metal	490	24	-	-
0.11	520	24	4.43	Weld
0.23	465	16	5 (full penetration)	HAZ

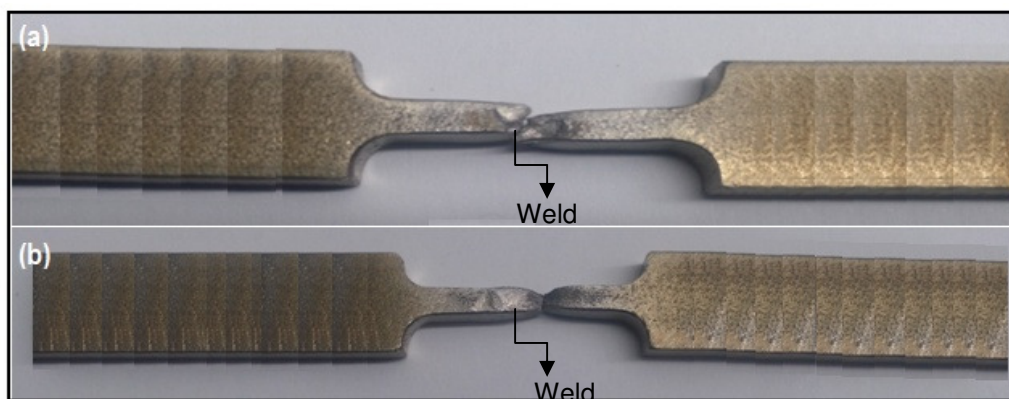


Figure 5.28: Photographs of transverse tensile samples containing laser welds performed at: (a) 0.11 kJ/mm; and (b) 0.23 kJ/mm.

Good weld penetration depths were achieved after LBW welding. The strength of the weld metal (UTS of approximately 520 MPa) at a heat input of 0.11 kJ/mm is higher than that of the base material. Due to the fast cooling rates associated with laser welding, the weld metal microstructure consists of fine ferrite grains, supersaturated in niobium and titanium. Solid solution strengthening and grain refinement increases the weld strength. The weld metal ductility (elongation of approximately 24%) is similar to that of the base material.

Laser welding at a heat input of 0.23 kJ/mm resulted in fracture in the HTHAZ close to the fusion line. The strength (UTS of approximately 465 MPa) and ductility (about 16%) values measured in this region are lower than those of the base material. Due

to the presence of overaged (Ti,Nb)C and grain growth in HAZ at this heat input, strength and ductility are reduced (see figure 5.18(b) and 5.19). The advantage of laser welding over GTAW is that good strength and ductility can be achieved with deep penetration after welding.

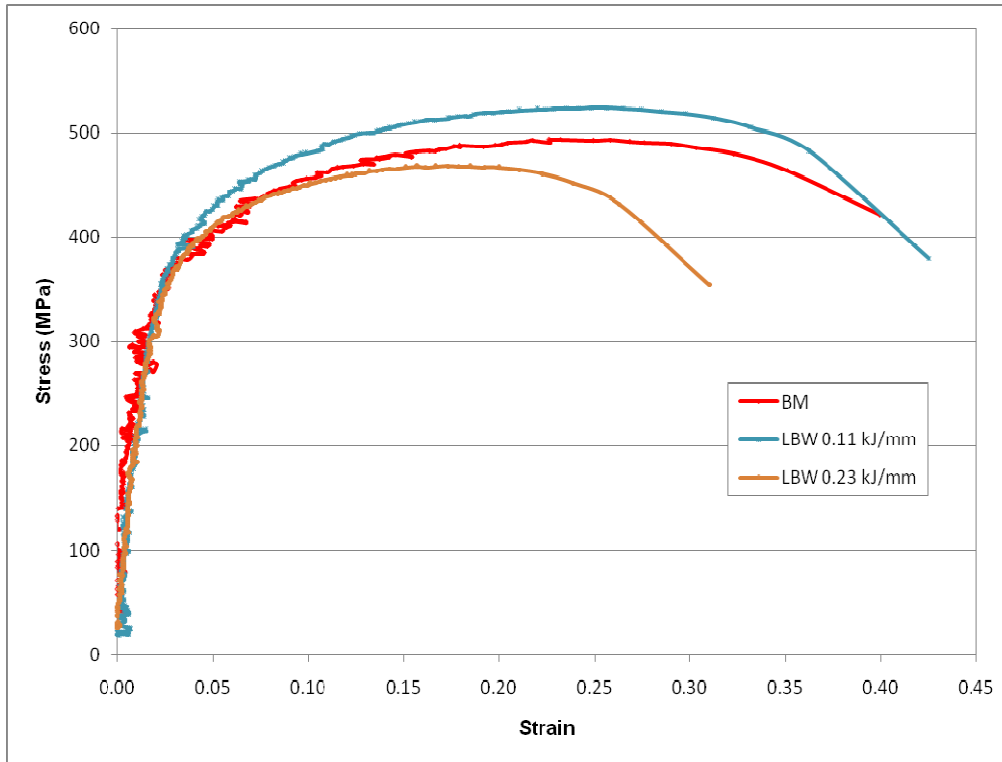


Figure 5.29: Stress-strain curves of the base material (BM) and laser welds performed at various heat inputs. Tests were done at 20 °C.

5.6 IMPACT TOUGHNESS

Figure 5.30 shows the impact toughness of Charpy sub-size specimens of LBW welds as a function of heat input. The impact toughness of both the heat-affected zone and weld metal of the laser welds is lower than that of base metal. Due to the presence of overaged (Ti,Nb)C and grain growth in HAZ at this heat input, impact toughness is reduced. It is also interesting to note that impact toughness of the weld metal at 0.11 and 0.22 kJ/mm is the same. This is due to fact that laser welds tend to have high depth-to-width ratios, consisting of elongated columnar grains growing epitaxially from the fusion line to the centreline of the weld. This grain structure promotes centreline segregation and creates a plane of weakness which decreases the impact toughness of the weld metal [9].

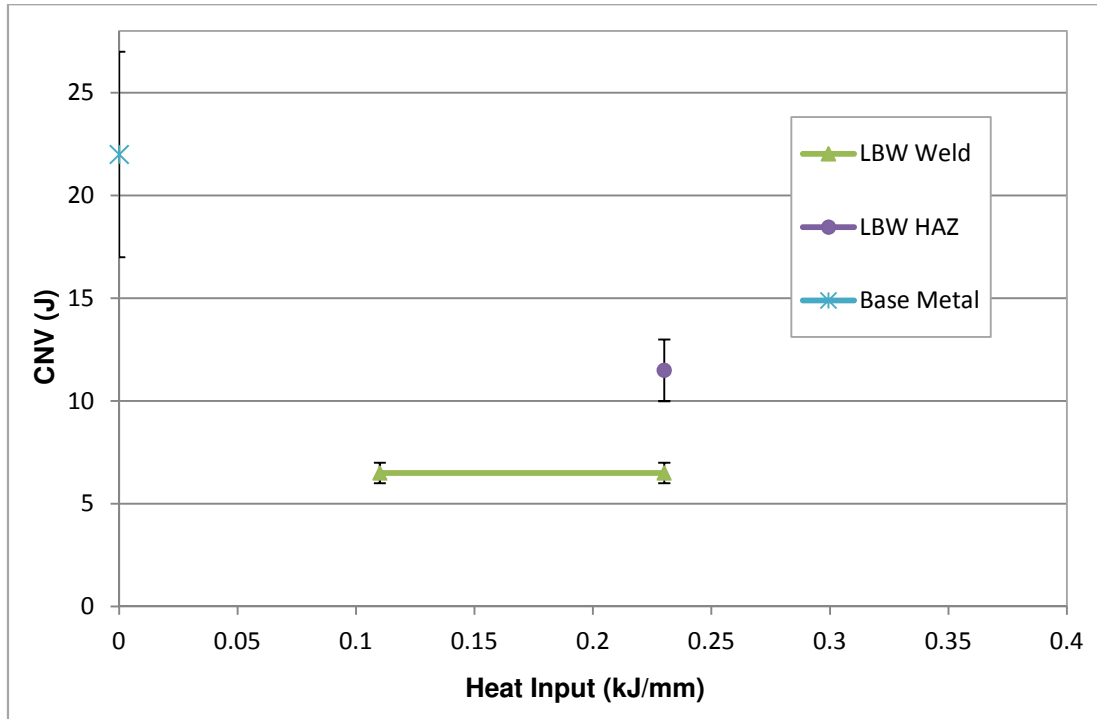


Figure 5.30: Impact energy curves of the weld metal and HAZ for LBW welds performed at various heat inputs (with 95% confidence interval). Tests were done at 20 °C. (Every data point represents the average of three impact tests).

5.7 FRACTURE SURFACES

Analyzing the fracture surfaces from Charpy impact tests can give more insight on the nature of the fracture. This examination of the fracture surfaces determines whether fracture was ductile, brittle, or a mixture of both. On a macroscale, ductile fracture is fibrous (shear fracture), while brittle fracture is granular (cleavage fracture). The flat facets of cleavage of fracture provides a high reflectivity and bright appearance, while dimpled surfaces of a ductile fibrous fracture provides a light-absorptive surface and dull appearance [10]. Although tensile and Charpy impact toughness test results of GTAW were not considered thus far because of low penetration achieved, but fracture surfaces will be considered here because the fracture surfaces can shed some light on the mode of fracture in these welds.

SEM microphotographs can also be used to establish the mode of fracture. Figure 5.33(a) shows SEM microphotographs of the fractured surface of the base material in low and high magnification. The low magnification microphotograph shows the base metal has a mixture of ductile and brittle fracture. The evidence of dimples in

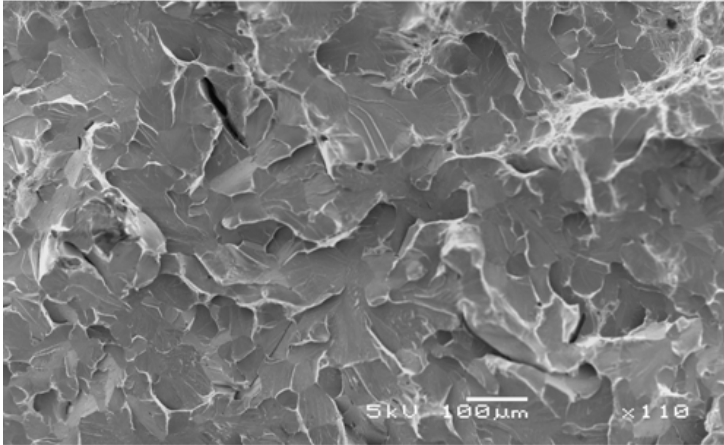
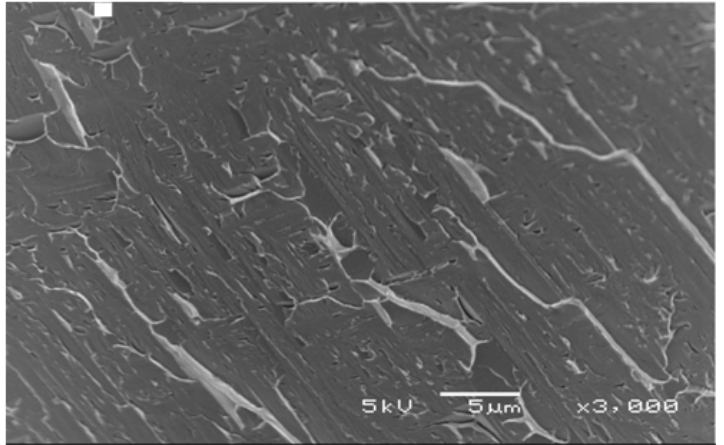
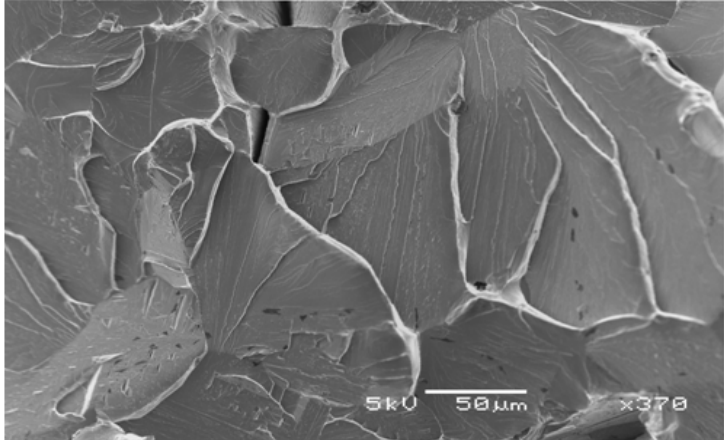
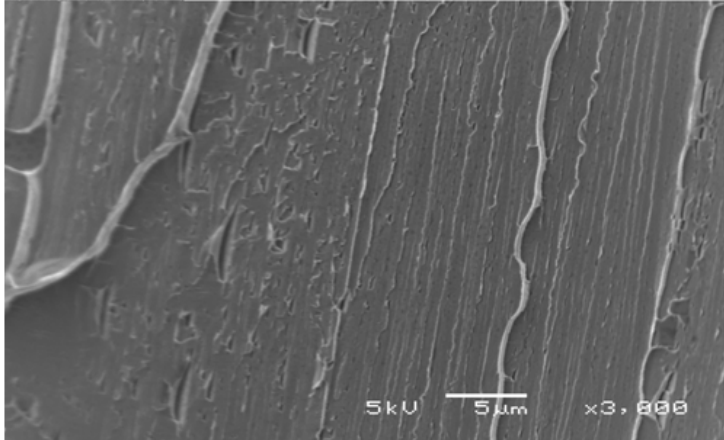
the base material fracture surface suggests ductile fracture, but the fracture seems to be largely brittle cleavage fracture. The high magnification microphotograph shows the river line pattern in the fractured grain. This is common with brittle cleavage fracture. An impact toughness of $22 \pm 8\text{J}$ shows the low toughness generally observed in ferritic stainless steels [9,12].

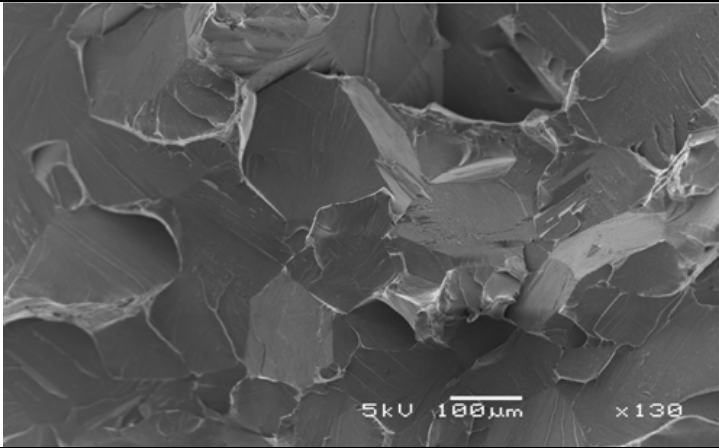
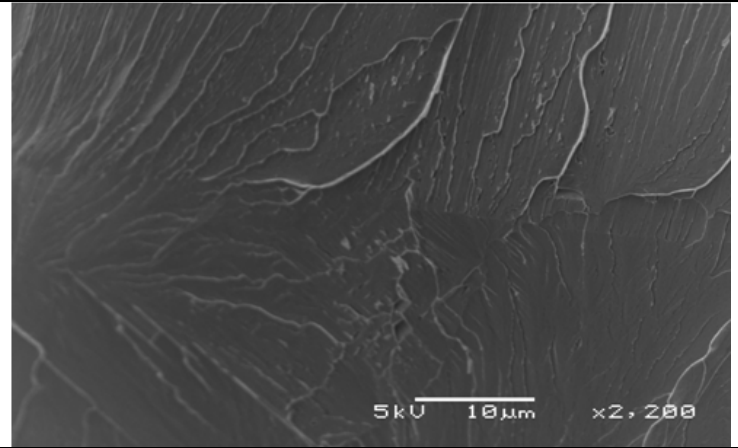
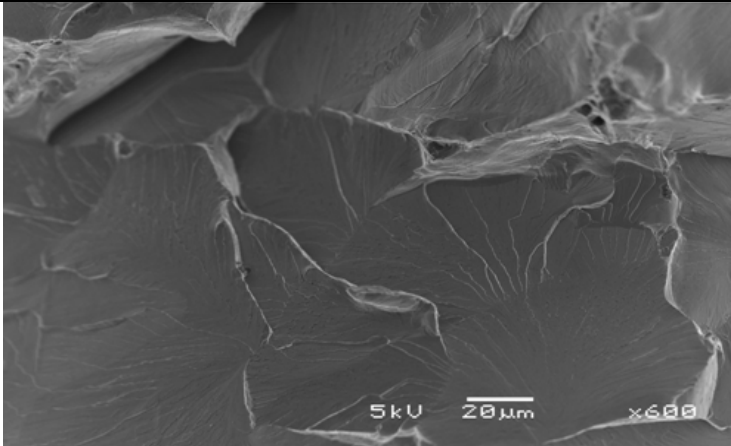
Figure 5.33(b) shows the SEM microphotographs of the fractured surface of the weld metal of a GTAW weld in low and high magnification done at a heat input of 0.45 kJ/mm. The low magnification microphotograph shows the fracture was brittle cleavage fracture. The coarse columnar grain structure is also evident from this microphotograph and it is consistent with earlier findings of this work (see Figure 5.5(d)). The high magnification microphotograph shows the river line pattern in the fractured grain.

Figure 5.33(c) shows the SEM microphotographs of the fractured surface in the HTHAZ of a GTAW weld in low and high magnification done at a heat input of 0.8 kJ/mm. The low magnification microphotograph shows evidence of transgranular cleavage fracture. Y Li et al [11] studied the fracture morphology in the coarse grained heat affected zone (CGHAZ) of a Cr18Mo2 ferritic stainless steel and transgranular cleavage fracture was also observed in the CGHAZ. The high magnification microphotograph shows the river line pattern in the fractured grain, common to cleavage fracture.

Figure 5.33(d) shows the low SEM microphotograph of the fractured surface in the weld metal of the LBW weld in low magnification done at a heat input of 0.23 kJ/mm . There is strong evidence of brittle cleavage fracture with river line pattern.

Low and high magnification SEM photomicrographs of the HAZ of a laser weld performed at a heat input of 0.23 kJ/mm are shown in Figure 5.32(e). The low magnification photomicrograph shows predominantly brittle cleavage fracture. The fine grain structure is evident in the HAZ, as expected for low heat input laser welding. The high magnification photomicrograph shows brittle cleavage fracture and a river line pattern showing the direction of crack propagation.

	Heat input (kJ/mm)	SEM Low magnification (100-600x)	SEM High magnification (2000-3000x)
(a) Base Metal	-		
(b) GTAW Weld Metal	0.45		

<p>(c) GTAW HAZ</p>	<p>0.80</p>		
<p>(d) LBW Weld Metal</p>	<p>0.23</p>		<p>Not examined</p>

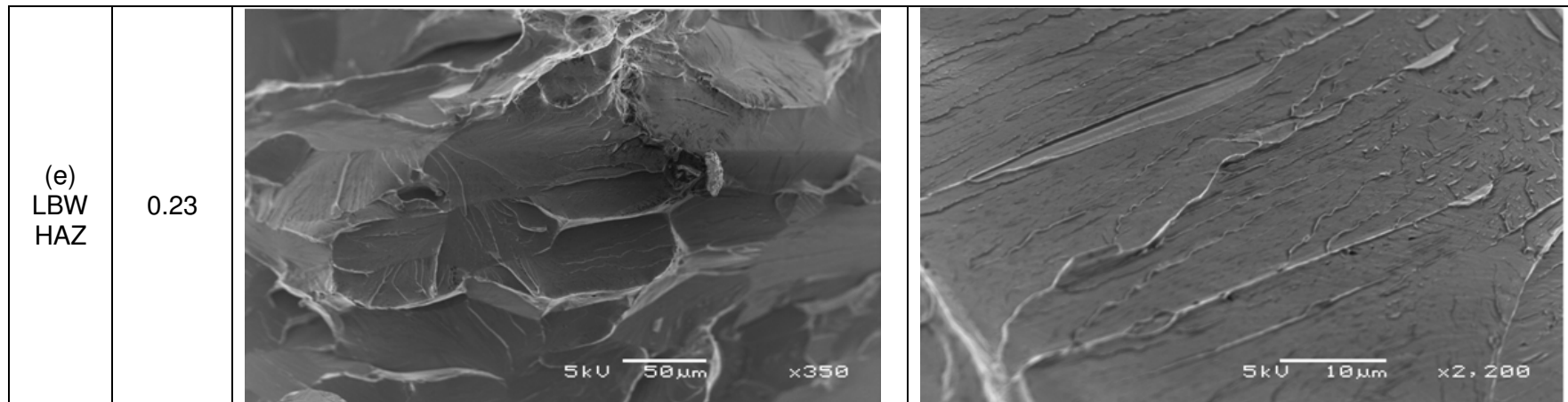


Figure 5.32: SEM microphotographs of fractured Charpy impact specimens tested at room temperature (20°C). The photomicrographs represent: (a) the base metal; (b) GTAW weld metal for a heat input of 0.45 kJ/mm; (c) GTAW HAZ for a heat input of 0.8 kJ/mm; (d) LBW weld metal for a heat input of 0.23 kJ/mm; and (e) LBW HAZ for a heat input of 0.23 kJ/mm. Low (left) and high (right) magnification SEM microphotographs and the measured Charpy impact toughness are shown.

5.8 REFERENCES

- [1] M.C. Balmforth and J.C. Lippold. "A new ferritic-martensitic stainless steel constitution diagram". *Welding Journal*, vol. 79, no. 12. 2000. pp. 339-345.
- [2] D. Rosenthal. "The theory of moving sources of heat and its application to metal treatments". *Transactions of the ASME*, vol.68. 1946. pp. 849-866.
- [3] K. Easterling. "Introduction to the physical metallurgy of welding". Butterworth-Heinemann. London. 1992.
- [4] C.C. Silva, J.P. Farias, H.C. Miranda, J.W.A. Menezes and M.A.M. Neto. "Microstructural characterization of the HAZ in AISI 444 ferritic stainless steel welds". *Materials Characterization*, vol. 59, no. 5. 2008. pp. 528-533.
- [5] A.F. Padilha, I.F. Machado and R.L. Plaut. "Microstructures and mechanical properties of Fe-15%Cr-15%Ni austenitic stainless steels containing different levels of niobium additions submitted to various processing stages". *Journal of Materials Processing Technology*, vol. 170, no. 1-2. 2005. pp. 89-96.
- [6] E. Schmidova, P. Svanda, D. Vesely and A. Kalendova. "Mechanism of degradation of stabilized corrosion-resistant steel during the welding cycle". *Anti-Corrosion Methods and Materials*, vol. 56, no. 4. 2009. pp. 206-217.
- [7] M. du Toit and C.J. van Niekerk. *Unpublished research*. University of Pretoria, South Africa. 2011.
- [8] M. Tullmin, F.P.A. Robinson, C.A.O. Henning, A. Strauss and J. le Grange. "Properties of laser-welded and electron-beam-welded ferritic stainless steel". *Journal of the Southern African Institute of Mining and Metallurgy*, vol. 89, no. 8. August 1989. pp. 243-249
- [9] D.H. Kah and D.W. Dickenson. "Weldability of ferritic stainless steels". *Welding Journal*, vol. 60 , no. 8. 1981. pp. 135s-142s.
- [10] G. E. Dieter, "Mechanical Metallurgy," McGraw-Hill Book, 1989, pp. 472–475.
- [11] Y. Li, Z. Zou and M. Thompson. "Microstructure and fracture morphology in the welding zone of Cr18Mo2 ferritic stainless steels". *Journal of Material Science Technology*, vol. 12, 1996. pp. 452-465.
- [12] ASM international. "Failure analysis and prevention". *ASM handbook*, vol. 11, 2002. pp. 516-526

CHAPTER 6: CONCLUSIONS AND RECOMMENDATIONS

6.1 CONCLUSIONS

Type 441 stainless steel (EN 1.4509 or UNS S43940) is a low carbon dual-stabilised ferritic grade with a nominal chromium content of 18%. This steel displays good corrosion and oxidation resistance, excellent high temperature strength and thermal fatigue resistance, and good formability, and is used primarily in high temperature applications and in automotive exhaust systems. The ferritic grades of stainless steel are difficult to weld successfully, especially in thicker sections, and for applications involving welding, the recommended plate thickness is limited to 2.5 mm for type 441. This investigation examined the weldability of type 441 stainless steel in thicker sections, with specific emphasis on the microstructure and mechanical properties of the weld metal and heat-affected zone after gas tungsten arc welding and laser welding at various heat input levels. The precipitation of intermetallic compounds (such as Laves and sigma phase) during the weld thermal cycle, carbide precipitation and grain growth were considered.

Type 441 ferritic stainless steel welded using gas tungsten arc welding (GTAW) undergoes significant grain growth in the high temperature heat-affected zone (HTHAZ) adjacent to the fusion line, with the grain size increasing with an increase in heat input. This can be attributed to the longer residence times above the grain coarsening temperature as a result of the slower cooling rates experienced by higher heat input welds. An unexplained grain refinement effect was observed in the low temperature heat-affected zone (LTHAZ) of the gas tungsten arc welds. Laser welds are less susceptible to grain growth in the heat-affected zone as a result of the low heat inputs associated with the process and the deep, narrow weld geometries.

Autogenous gas tungsten arc welds were shown to consist of intermetallic Laves phase in the form of discreet intragranular particles and continuous dense grain boundary precipitation, coarse sigma phase precipitates, fine needle-like titanium-rich carbides (with some niobium in solid solution) and chromium-rich $M_{23}C_6$ carbides in the ferrite matrix. The presence of intermetallic compounds and carbide particles raised the hardness of the weld metal to approximately 270 HV_{0.3} (hardness on the Vickers scale) from the as-supplied base metal hardness of about 160 HV_{0.3}. The

HAZ microstructures of the gas tungsten arc welds contained needle-like titanium-rich precipitates and $M_{23}C_6$ carbides.

In contrast, the fusion zones of the laser welds were mostly free of second phase particles, whereas the HAZ contained partially dissolved cuboidal titanium-rich carbides and some $M_{23}C_6$ carbides (in the higher heat input weld). The laser welds displayed significantly higher strength and ductility, which can be attributed to the lower heat inputs utilised and the finer grain sizes. The weld toughness was, however, very low. This is due to the columnar grain structure of the weld metal which creates a plane of weakness at the weld centreline.

Although type 441 is dual-stabilized with titanium and niobium, welding at low heat input levels resulted in chromium-rich $M_{23}C_6$ precipitation in the high temperature heat-affected zone during cooling, effectively sensitising the welds to intergranular corrosion. Sensitisation in gas tungsten arc welds was limited to a narrow region of the HTHAZ adjacent to the fusion line in low heat input welds, but extended well into the HTHAZ and weld metal at heat inputs of 0.3 kJ/mm and 0.45 kJ/mm. Sensitisation was largely suppressed in samples welded at a heat input of 0.7 kJ/mm. Sensitisation was observed in the weld metal of laser welds performed at 0.11 kJ/mm, and in the weld and HTHAZ after welding at 0.23 kJ/mm.

In order to successfully weld type 441 ferritic stainless steel, low heat inputs are recommended to restrict grain growth and suppress the precipitation of harmful intermetallic compounds in the weld and heat-affected zone. Low heat inputs, however, promote sensitisation and may render the welds susceptible to intergranular attack.

6.2 RECOMMENDATIONS FOR FUTURE WORK

The mechanism responsible for the grain refinement effect observed in the LTHAZ of the gas tungsten arc welds is still not understood. Further LTHAZ simulations using the Gleeble™ thermomechanical simulator, in combination with quenching experiments from temperatures within the LTHAZ, are proposed. The reasons for the unusual needle-shaped morphology of the titanium carbides observed in the gas tungsten arc welds also need to be investigated.

APPENDIX

Table A1: Grain size measurements in the high temperature HAZ of GTAW welds as a function of heat input.

Heat input	Grain size measurements, μm										
	1	2	3	4	5	6	7	8	Average	Standard deviation	Error
0.09	49.5	31.3	35.4						38.7	9.5	5.5
0.15	45.1	49.5	44.0	56.2	55.6	45.4	46.4	46.4	48.6	4.8	1.7
0.23	72.1	55.6	55.7	49.3	84.2	67.2	64.2	57.9	63.3	11.2	4.0
0.30	78.7	70.2	97.6	58.1					76.1	16.6	8.3
0.68	207.9	109.5	96.5	110.2					131.0	51.6	25.8

Table A2: Grain size measurements in the HAZ of laser welds as a function of heat input.

Heat input	Grain size measurements, μm						
	1	2	3	4	Average	Standard deviation	Error
0.11	18.8	20.9	26.8	27.6	27.2	4.4	3.1
0.23	39.4	46.0	36.5	43.0	41.2	4.1	2.1

Table A3: Micro-Vickers hardness measurements across GTAW welds as a function of distance from the fusion line at a heat input of 0.3 kJ/mm.

Distance from fusion line, mm	-0.5	-0.15	0	0.05	0.1	0.15	0.25	0.45	0.65	0.85	1.05	1.25	1.45	1.65
Hardness, HV	277	303	303	174	197	156	146	160	169	175	153	161	160	166
Hardness, HV	318	217	217	192	196	142	174	156	160	183	163	156	157	182
Hardness, HV	235	288	288	-	-	163	165	167	155	158	164	154	158	154
Average	277	269	269	183	197	154	161	161	161	172	160	157	159	167
Standard deviation	41	46	46	12	1	11	14	6	7	13	6	4	1	14
Error	24	27	27	9	1	6	8	3	4	8	4	2	1	8

Table A4: Orientation of micrographs for various figures in Chapter 5. The rectangular box represents the orientation of the micrograph in respect to the fusion zone.

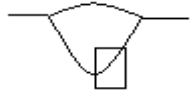
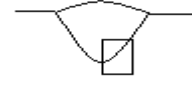
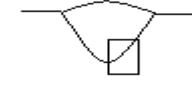
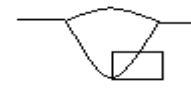
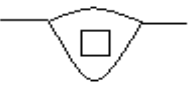
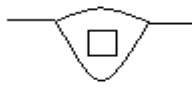
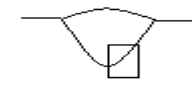
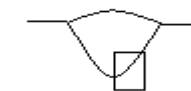












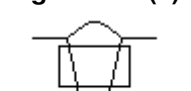






Figure 5.5(a) 	Figure 5.5(b) 	Figure 5.5(c) 	Figure 5.5(d) 
Figure 5.6(a) 	Figure 5.6(b) 	Figure 5.10(a) 	Figure 5.10(b) 
Figure 5.12(a) 	Figure 5.12(b) 	Figure 5.14(a) 	Figure 5.14(b) 
Figure 5.15(a) 	Figure 5.15(b) 	Figure 5.16(a) 	Figure 5.16(b) 
Figure 5.17(a) 	Figure 5.17(b) 	Figure 5.18(a) 	Figure 5.18(b) 
Figure 5.20(a) 	Figure 5.20(b) 	Figure 5.21(a) 	Figure 5.21(b) 
Figure 5.22 	Figure 5.26(a) 	Figure 26(b) 	

Table A5: Parameters used in the Rosenthal heat flow equation to compute the thermal profile at a distance R from the fusion line [1].

Heat input	0.3kJ/mm
T_o	298 K
Q_c	4700000Jm ⁻³ K ⁻¹
d'	49.1 mm
d (measured)	5.0 mm
δ (conductivity)	24.9Wm ⁻¹ K ⁻¹
a (diffusivity)	0.0000053m ² s ⁻¹

REFERENCES

- [1] D. Rosenthal. “*The theory of moving sources of heat and its application to metal treatments*”. Transactions of the ASME, vol.68. 1946. pp. 849-866.